

AD-A196 023

DTIC FILE COPY

1

Doppler Radar Analysis of Coastal Marine
Atmospheric Boundary Layer Structure
During a Cold Air Outbreak

by
Michael N. Jones

DTIC
ELECTE
AUG 03 1988
S D

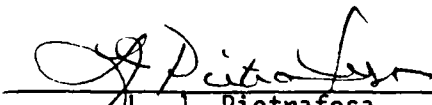
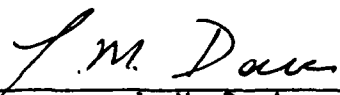
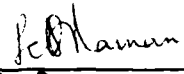
A thesis submitted to the Graduate Faculty of
North Carolina State University
in partial fulfillment of the
requirements for the Degree of
Master of Science

Department of
Marine, Earth and Atmospheric Sciences

Raleigh
1988

DISTRIBUTION STATEMENT A
Approved for public release
Distribution Unlimited

Approved By:


L. J. Pietrafesa

J. M. Davis
Co-chairman of Advisory Committee

S. Raman
Co-chairman of Advisory Committee

88 8 02 122

REPORT DOCUMENTATION PAGE		READ INSTRUCTIONS BEFORE COMPLETING FORM
1. REPORT NUMBER AFIT/CI/NR 88- 1	2. GOVT ACCESSION NO.	3. RECIPIENT'S CATALOG NUMBER
4. TITLE (and Subtitle) DOPPLER RADAR ANALYSIS OF COASTAL MARINE ATMOSPHERIC BOUNDARY LAYER STRUCTURE DURING A COLD AIR OUTBREAK		5. TYPE OF REPORT & PERIOD COVERED MS THESIS
7. AUTHOR(s) MICHAEL N. JONES		6. PERFORMING ORG. REPORT NUMBER
9. PERFORMING ORGANIZATION NAME AND ADDRESS AFIT STUDENT AT: NORTH CAROLINA STATE UNIVERSITY		8. CONTRACT OR GRANT NUMBER(s)
11. CONTROLLING OFFICE NAME AND ADDRESS		10. PROGRAM ELEMENT, PROJECT, TASK AREA & WORK UNIT NUMBERS
14. MONITORING AGENCY NAME & ADDRESS (if different from Controlling Office) AFIT/NR Wright-Patterson AFB OH 45433-6583		12. REPORT DATE 1988
		13. NUMBER OF PAGES 112
		15. SECURITY CLASS. (of this report) UNCLASSIFIED
		15a. DECLASSIFICATION/DOWNGRADING SCHEDULE
16. DISTRIBUTION STATEMENT (of this Report) DISTRIBUTED UNLIMITED: APPROVED FOR PUBLIC RELEASE		
17. DISTRIBUTION STATEMENT (of the abstract entered in Block 20, if different from Report) SAME AS REPORT		
18. SUPPLEMENTARY NOTES Approved for Public Release: IAW AFR 190-1 LYNN E. WOLAVER <i>Lynn Wolaver</i> 12 Feb 88 Dean for Research and Professional Development Air Force Institute of Technology Wright-Patterson AFB OH 45433-6583		
19. KEY WORDS (Continue on reverse side if necessary and identify by block number)		
20. ABSTRACT (Continue on reverse side if necessary and identify by block number) ATTACHED		

ABSTRACT

JONES, MICHAEL N. Doppler Radar Analysis of Coastal Marine Atmospheric Boundary Layer Structure During a Cold Air Outbreak (Under the direction of Sethu Raman and Jerry Davis).

This study documents and interprets the spatial and temporal variation of Marine Atmospheric Boundary Layer (MABL) structure during the latter stages of a Cold Air Outbreak (CAO) along the Outer Banks of North Carolina, 8 March 1986, Genesis of Atlantic Lows Experiment (GALE). Two C-band pulsed Doppler radars, one at Ocracoke and the other at Cape Hatteras, were used to collect reflectivity and radial velocity data in the chaff-filled MABL. The single Doppler analysis technique known as Velocity Azimuth Display, henceforth VAD (Browning and Wexler, 1968), was used to attain numerical values for a variety of kinematic properties. Time-height plots of horizontal wind speed, vertical velocity, horizontal divergence and deformation were constructed to depict the temporal variation of the MABL. Horizontal wind speed and direction versus altitude were plotted for each VAD analysis in order that anomalies in the MABL wind profiles may be identified and explained. The VAD analysis radius was varied between 5 and 15 kilometers so that the spatial distribution of the wind field could also be observed.

Chaff was dispersed by aircraft at a distance equivalent to 40 minutes travel distance upwind from the radar network. Dispersal began at 1746 Greenwich Mean Time (GMT) amidst a mean boundary layer wind from the north at roughly 7 meters per second. The MABL was thermally

unstable, well mixed and was capped by a strong subsidence inversion. As the study progressed, a synoptic high rapidly built in from the northwest. Winds gradually diminished and became northeasterly. Rawinsonde data from Buxton, North Carolina (Cape Hatteras), indicated increasing stability within the boundary layer such that by the end of the study period, 2200 GMT, the MABL had transitioned from turbulent to essentially stable conditions.

Time-height plots of horizontal windspeed, viertical velocity, horizontal divergence and deformation well depict the turbulence transition. Evidence of a meso- γ scale MABL perturbation, most likely the result of migrating cellular structures, was observed in both the 5 and 10 kilometer radii time-height plots of vertical velocity and horizontal divergence between 1930 and 2030 GMT. The 2103 GMT vertical slice (VSLICE) of radial velocity over Pamlico Sound depicted a strong vertical wind shear at an altitude of approximately 250 meters and at a range and azimuth of 24 kilometers and 335 degrees, respectively. This phenomenon represents a surface layer circulation pattern in opposition to the meso- α gradient flow, likely the result of anticyclonic shear arising from the land/water surface roughness discontinuity induced wind differential, and a veering caused by the Coriolis force. This flow pattern was also evident in the wind direction data from the Portable Automated Mesonet (PAM) station #46 beginning at 2030 GMT and by the 15 and 10 kilometer VAD wind speed and direction versus altitude plots at 2131 and 2201 GMT, respectively.

The results of this study well illustrate the ability of a single Doppler analysis to discern spatial and temporal variations of

kinematic properties in the boundary layer where remote sensing represents a viable means of attaining such information.

ABSTRACT

JONES, MICHAEL N. Doppler Radar Analysis of Coastal Marine Atmospheric Boundary Layer Structure During a Cold Air Outbreak (Under the direction of Sethu Raman and Jerry Davis).

This study documents and interprets the spatial and temporal variation of Marine Atmospheric Boundary Layer (MABL) structure during the latter stages of a Cold Air Outbreak (CAO) along the Outer Banks of North Carolina, 8 March 1986, Genesis of Atlantic Lows Experiment (GALE). Two C-band pulsed Doppler radars, one at Ocracoke and the other at Cape Hatteras, were used to collect reflectivity and radial velocity data in the chaff-filled MABL. The single Doppler analysis technique known as Velocity Azimuth Display, henceforth VAD (Browning and Wexler, 1968), was used to attain numerical values for a variety of kinematic properties. Time-height plots of horizontal wind speed, vertical velocity, horizontal divergence and deformation were constructed to depict the temporal variation of the MABL. Horizontal wind speed and direction versus altitude were plotted for each VAD analysis in order that anomalies in the MABL wind profiles may be identified and explained. The VAD analysis radius was varied between 5 and 15 kilometers so that the spatial distribution of the wind field could also be observed.

Chaff was dispersed by aircraft at a distance equivalent to 40 minutes travel distance upwind from the radar network. Dispersal began at 1746 Greenwich Mean Time (GMT) amidst a mean boundary layer wind from the north at roughly 7 meters per second. The MABL was thermally

unstable, well mixed and was capped by a strong subsidence inversion. As the study progressed, a synoptic high rapidly built in from the northwest. Winds gradually diminished and became northeasterly. Rawinsonde data from Buxton, North Carolina (Cape Hatteras), indicated increasing stability within the boundary layer such that by the end of the study period, 2200 GMT, the MABL had transitioned from turbulent to essentially stable conditions.

Time-height plots of horizontal windspeed, vertical velocity, horizontal divergence and deformation well depict the turbulence transition. Evidence of a meso- γ scale MABL perturbation, most likely the result of migrating cellular structures, was observed in both the 5 and 10 kilometer radii time-height plots of vertical velocity and horizontal divergence between 1930 and 2030 GMT. The 2103 GMT vertical slice (VSLICE) of radial velocity over Pamlico Sound depicted a strong vertical wind shear at an altitude of approximately 250 meters and at a range and azimuth of 24 kilometers and 335 degrees, respectively. This phenomenon represents a surface layer circulation pattern in opposition to the meso- α gradient flow, likely the result of anticyclonic shear arising from the land/water surface roughness discontinuity induced wind differential, and a veering caused by the Coriolis force. This flow pattern was also evident in the wind direction data from the Portable Automated Mesonet (PAM) station #46 beginning at 2030 GMT and by the 15 and 10 kilometer VAD wind speed and direction versus altitude plots at 2131 and 2201 GMT, respectively.

The results of this study well illustrate the ability of a single Doppler analysis to discern spatial and temporal variations of

kinematic properties in the boundary layer where remote sensing represents a viable means of attaining such information.



Accession For	
NTIS CR420	<input checked="checked" type="checkbox"/>
DTIC TAB	<input type="checkbox"/>
Unannounced	<input type="checkbox"/>
Justification	
By	
Distribution	
Availability Codes	
Dist	Avail and for Special
A-1	

BIOGRAPHY

Michael N. Jones is the son of Robert P. Jones and Ida M.

[REDACTED]

[REDACTED] He was raised in Owego, New York, and graduated from the Owego Free Academy in 1976.

He received a Bachelor of Science degree in Geology, with an emphasis in Environmental Studies, in January of 1981 from the State University of New York at Cortland.

In September of 1982 the author entered the United States Air Force Officer training School and was commissioned a second lieutenant in December of that same year.

In August of 1985 he entered the Graduate School at North Carolina State University to pursue a Master of Science degree in Meteorology.

The author has one child, a son, [REDACTED]

ACKNOWLEDGEMENTS

The author wishes to extend his appreciation to the United States Air Force, particularly the Air Force Institute of Technology and the Air Weather Service, for providing the opportunity to advance his formal education. He also extends his appreciation to Dr. Sethu Raman and Dr. Jerry Davis, Co-chairmen of his Advisory Committee, for their guidance and advice in the preparation of this thesis.

The staff at the National Center for Atmospheric Research, Field Observation Facility, were invaluable during the collection, processing and analysis of this data. Particular thanks are extended to Dr. Paul Herzegh, Cindy Mueller, Chris Burghart and Jonathan Corbett.

Special thanks are extended to Rob Marshall, a visiting professor in the Department of Electrical Engineering, for his extensive and vital assistance during all phases of this study. Several fellow graduate students, particularly Jim Kroll and Brian Templeman, were very cooperative in sharing their knowledge and expertise in computer generated data plots.

Finally, the author wishes to thank his family and friends, particularly his parents and son, for their encouragement and moral support throughout these trying times.

Part of this work was supported by the National Science Foundation under Grant ATM-83-11812 and Office of Naval Research under Contract N00014-84-K-0620.

TABLE OF CONTENTS

	Page
LIST OF TABLES	vi
LIST OF FIGURES.	vii
LIST OF SYMBOLES.	xii
1. INTRODUCTION	1
1.1 General Comments.	1
1.2 Literature Review	3
1.2.1 Doppler Radar Analysis Techniques.	3
1.2.2 Characteristics of the Coastal Marine Atmospheric Boundary Layer (MABL).	6
1.2.3 Doppler Radar Studies of the Planetary Boundary Layer (PBL)	8
1.3 Objectives of This Study.	14
2. EXPERIMENTAL DESIGN.	15
2.1 Radar Characteristics	15
2.2 Selection of Values for Radar Variables	16
2.3 Chaff Dispersal	19
3. DATA ACQUISITION	22
3.1 Rawinsonde.	22
3.2 Portable Automated Mesonet (PAM).	22
3.3 Doppler Radar	24
3.3.1 Description of the Velocity Azimuth Display (VAD) Technique.	24
3.3.1.1 Inherent errors	29
3.3.1.2 Data Editing	33
3.3.2 Description of the Vertical Slice (VSLICE) Technique	34

TABLE OF CONTENTS (continued)

	Page
4. SYNOPTIC AND MESOSCALE OVERVIEW.	39
4.1 Synoptic Setting.	39
4.2 Meso- α Setting.	43
4.3 Meso- β Surface Temperature and Wind Field Analysis. . .	47
4.3.1 Surface Temperature Distribution	47
4.3.2 Wind Field Analysis	47
5. DISCUSSION OF RESULTS.	66
5.1 Temporal Variations of MABL Structure	66
5.1.1 Rawinsonde Derived Lapse Rates	66
5.1.2 VAD-Derived Time-height Plots of Kinematic Properties.	67
5.2 Low-level Wind Shear.	86
5.2.1 VSLICE Profile	86
5.2.2 VAD Derived Wind Profiles.	89
6. CONCLUSIONS.	107
7. LIS. OF REFERENCES	109

LIST OF TABLES

	Page
2.1 Principle Characteristics of the Doppler Radars Used in the 8 March 1986 MABL Study	15
5.1 Boundary Layer Lapse Rates Derived From NWS Rawinsonde Data, Cape Hatteras, North Carolina, 8 March 1986	66
5.2 Descriptive Listing of the VAD Volumes Processed for the 8 March 1986 MABL Study	69
5.3 Altitude Locations, in 50 Meter Increments, of Data Points Within the 8 March Time-height Plots, by Analysis Radius	69

LIST OF FIGURES

	Page
1.1 Location of the Doppler radars CP-3 and CP-4 along the Outer Banks of North Carolina during GALE.	2
2.1 Location of the chaff dispersal flight track for the 8 March 1986 MABL study.	20
3.1 Location of PAM stations 40 and 45 through 49, the micrometeorological tower at Duck and the Diamond Shoals NOAA C-MAN platform.	23
3.2a Plot of radial velocity versus azimuth from the 4.8 degree scan, VAD radius of 5 kilometers taken by the CP-4 radar at 1835 GMT, 8 March 1986. Seventy-seven percent of the possible data points remained after editing; this scan was unconditionally accepted.	35
3.2b Plot of radial velocity versus azimuth from the 2.4 degree scan, VAD radius of 15 kilometers taken by the CP-3 radar at 2106 GMT, 8 March 1986. Thirty-three percent of the possible data points remained after editing; this scan was conditionally accepted.	36
3.2c Plot of radial velocity versus azimuth from the 3.2 degree scan, VAD radius of 15 kilometers taken by the CP-3 radar at 2108 GMT, 8 March 1986. Eight percent of the possible data points remained after editing; this scan was rejected.	37
4.1a Synoptic map of the United States on 7 March 1986 at 1200 GMT.	40
4.1b Synoptic map of the United States on 8 March 1986 at 1200 GMT.	41
4.1c Synoptic map of the United States on 9 March 1986 at 1200 GMT.	42
4.2a Meso- α map of the eastern United States on 8 March 1986 at 1200 GMT.	44
4.2b Meso- α map of the eastern United States on 8 March 1986 at 1800 GMT.	45
4.2c Meso- α map of the eastern United States on 9 March 1986 at 0000 GMT.	46
4.3a Distribution of SST across the Outer Banks coastal waters on 7 March 1986	48

LIST OF FIGURES (continued)

	Page
4.3b Distribution of SST across the Outer Banks coastal waters on 9 March 1986	49
4.4a Plot of the meso- β wind field along the Outer Banks of North Carolina on 8 March 1986 at 1800 GMT.	50
4.4b Plot of the meso- β wind field along the Outer Banks of North Carolina on 8 March 1986 at 1830 GMT.	51
4.4c Plot of the meso- β wind field along the Outer Banks of North Carolina on 8 March 1986 at 1900 GMT.	52
4.4d Plot of the meso- β wind field along the Outer Banks of North Carolina on 8 March 1986 at 1930 GMT.	53
4.4e Plot of the meso- β wind field along the Outer Banks of North Carolina on 8 March 1986 at 2000 GMT.	54
4.4f Plot of the meso- β wind field along the Outer Banks of North Carolina on 8 March 1986 at 2030 GMT.	55
4.4g Plot of the meso- β wind field along the Outer Banks of North Carolina on 8 March 1986 at 2100 GMT.	56
4.4h Plot of the meso- β wind field along the Outer Banks of North Carolina on 8 March 1986 at 2130 GMT.	57
4.4i Plot of the meso- β wind field along the Outer Banks of North Carolina on 8 March 1986 at 2200 GMT.	58
4.5a Distribution of chaff at 1903 GMT, 8 March 1986, as depicted by the CP-3 0.5 degree PPI display of radial velocity	61
4.5b Distribution of chaff at 2009 GMT, 8 March 1986, as depicted by the CP-3 0.5 degree PPI display of radial velocity	62
4.5c Distribution of chaff at 2103 GMT, 8 March 1986, as depicted by the CP-3 0.3 degree PPI display of radial velocity	63
4.5d Distribution of chaff at 2202 GMT, 8 March 1986, as depicted by the CP-3 0.3 degree PPI display of radial velocity	64
5.1 VAD analysis radii around the CP-3 and CP-4 radars for the 8 March 1986 MABL radar study.	68

LIST OF FIGURES (continued)

	Page
5.2a Time-height plot of horizontal wind speed during the 8 March 1986 MABL radar study for the VAD analysis radius of 5 kilometers	71
5.2b Time-height plot of vertical velocity during the 8 March 1986 MABL radar study for the VAD analysis radius of 5 kilometers	72
5.2c Time-height plot of horizontal divergence during the 8 March 1986 MABL radar study for the VAD analysis radius of 5 kilometers	73
5.2d Time-height plot of horizontal deformation during the 8 March 1986 MABL radar study for the VAD analysis radius of 5 kilometers	74
5.3a Time-height plot of horizontal wind speed during the 8 March 1986 MABL radar study for the VAD analysis radius of 10 kilometers	75
5.3b Time-height plot of vertical velocity during the 8 March 1986 MABL radar study for the VAD analysis radius of 10 kilometers	76
5.3c Time-height plot of horizontal divergence during the 8 March 1986 MABL radar study for the VAD analysis radius of 10 kilometers.	77
5.3d Time-height plot of horizontal deformation during the 8 March 1986 MABL radar study for the VAD analysis radius of 10 kilometers.	78
5.4a Time-height plot of horizontal wind speed during the 8 March 1986 MABL radar study for the VAD analysis radius of 15 kilometers	79
5.4b Time-height plot of vertical velocity during the 8 March 1986 MABL radar study for the VAD analysis radius of 15 kilometers	80
5.4c Time-height plot of horizontal divergence during the 8 March 1986 MABL radar study for the VAD analysis radius of 15 kilometers	81
5.4d Time-height plot of horizontal deformation during the 8 March 1986 MABL radar study for the VAD analysis radius of 15 kilometers	82

LIST OF FIGURES (continued)

	Page
5.5a Location of the 8 March 1986, 2103 GMT, VSLICE	87
5.5b VSLICE of radial velocity over Pamlico Sound, constructed from the volume of data taken by the CP-3 radar at 2103 GMT on 8 March 1986	88
5.6a Plot of horizontal wind speed and direction versus altitude from the 5 kilometer radius VAD analysis taken by the CP-4 radar at 1831 GMT on 8 March 1986. . . .	90
5.6b Plot of horizontal wind speed and direction versus altitude from the 5 kilometer radius VAD analysis taken by the CP-3 radar at 1934 GMT on 8 March 1986. . . .	91
5.6c Plot of horizontal wind speed and direction versus altitude from the 5 kilometer radius VAD analysis taken by the CP-3 radar at 2003 GMT on 8 March 1986. . . .	92
5.6d Plot of horizontal wind speed and direction versus altitude from the 5 kilometer radius VAD analysis taken by the CP-3 radar at 2034 GMT on 8 March 1986. . . .	93
5.6e Plot of horizontal wind speed and direction versus altitude from the 5 kilometer radius VAD analysis taken by the CP-3 radar at 2103 GMT on 8 March 1986. . . .	94
5.6f Plot of horizontal wind speed and direction versus altitude from the 5 kilometer radius VAD analysis taken by the CP-3 radar at 2131 GMT on 8 March 1986. . . .	95
5.6g Plot of horizontal wind speed and direction versus altitude from the 5 kilometer radius VAD analysis taken by the CP-3 radar at 2201 GMT on 8 March 1986. . . .	96
5.7a Plot of horizontal wind speed and direction versus altitude from the 10 kilometer radius VAD analysis taken by the CP-3 radar at 2003 GMT on 8 March 1986. . . .	98
5.7b Plot of horizontal wind speed and direction versus altitude from the 10 kilometer radius VAD analysis taken by the CP-3 radar at 2034 GMT on 8 March 1986. . . .	99
5.7c Plot of horizontal wind speed and direction versus altitude from the 10 kilometer radius VAD analysis taken by the CP-3 radar at 2103 GMT on 8 March 1986. . . .	100

LIST OF FIGURES (continued)

	Page
5.7d Plot of horizontal wind speed and direction versus altitude from the 10 kilometer radius VAD analysis taken by the CP-3 radar at 2131 GMT on 8 March 1986. . . .	101
5.7e Plot of horizontal wind speed and direction versus altitude from the 10 kilometer radius VAD analysis taken by the CP-3 radar at 2201 GMT on 8 March 1986. . . .	102
5.8a Plot of horizontal wind speed and direction versus altitude from the 15 kilometer radius VAD analysis taken by the CP-3 radar at 2034 GMT on 8 March 1986. . . .	104
5.8b Plot of horizontal wind speed and direction versus altitude from the 15 kilometer radius VAD analysis taken by the CP-3 radar at 2103 GMT on 8 March 1986. . . .	105
5.8c Plot of horizontal wind speed and direction versus altitude from the 15 kilometer radius VAD analysis taken by the CP-3 radar at 2131 GMT on 8 March 1986. . . .	106

LIST OF SYMBOLS

V_R	radial velocity
β	azimuth angle measured counterclockwise from east
θ	elevation angle
ϕ	angular width of the radar beam
r	horizontal range
ρ	atmospheric density
α	azimuth rotation rate of the radar beam
SR	slant range
n	radar transmission wavelength
d	spatial width of the radar beam
δ_v	Doppler bias error
K_ϕ	azimuthal or vertical wind shear of the Doppler velocity
$\delta\phi$	azimuthal or elevation inaccuracy of the radar beam position
PRF	pulse repetition frequency
N	number of pulses per sample
σ_{V_r}	Statistical uncertainty of the radial velocity measurement
σ_∞^2	variance of the Doppler spectrum resulting from azimuth rotation rate
γ	atmospheric lapse rate
γ_d	dry adiabatic lapse rate

1. INTRODUCTION

1.1 General Comments

During the winter of 1986, a multi-agency field project, the Genesis of Atlantic Lows Experiment (GALE), was realized. Its encompassing objective was the study of various mesoscale processes that may affect the rapid intensification of winter storms which periodically disrupt the United States east coast metropolitan complex. Perhaps the most notable such storm of the past decade was the Presidents' Day Snowstorm, 18-19 February 1979 (Bosart, 1981). Limited Fine Mesh and Seven-Layer Primitive Equation models failed to predict the explosive cyclogenesis which resulted in a 24 hour snowfall of nearly two feet in the vicinity of the District of Columbia.

One particular aspect of GALE was the analysis of Marine Atmospheric Boundary Layer (MABL) kinematics on a meso- γ scale, 2 to 20 kilometers, and the lower end of meso- β scale, 20 to 200 kilometers (Dirks, et al., 1988; Raman and Riordan, 1988). To attain the data necessary to perform such a study, two C-band pulsed Doppler radars, henceforth referred to as CP-3 and CP-4, were placed along the Outer Banks of North Carolina (Figure 1.1). These radars were provided by the National Center for Atmospheric Research, Field Observation Facility (NCAR FOF). The Outer Banks region was chosen as the study site as it is in this vicinity that east coast cyclogenesis normally occurs. Also, this location is close to the Gulf Stream.

This thesis is a case study which documents and interprets the spatial and temporal variation of MABL kinematic structure during a

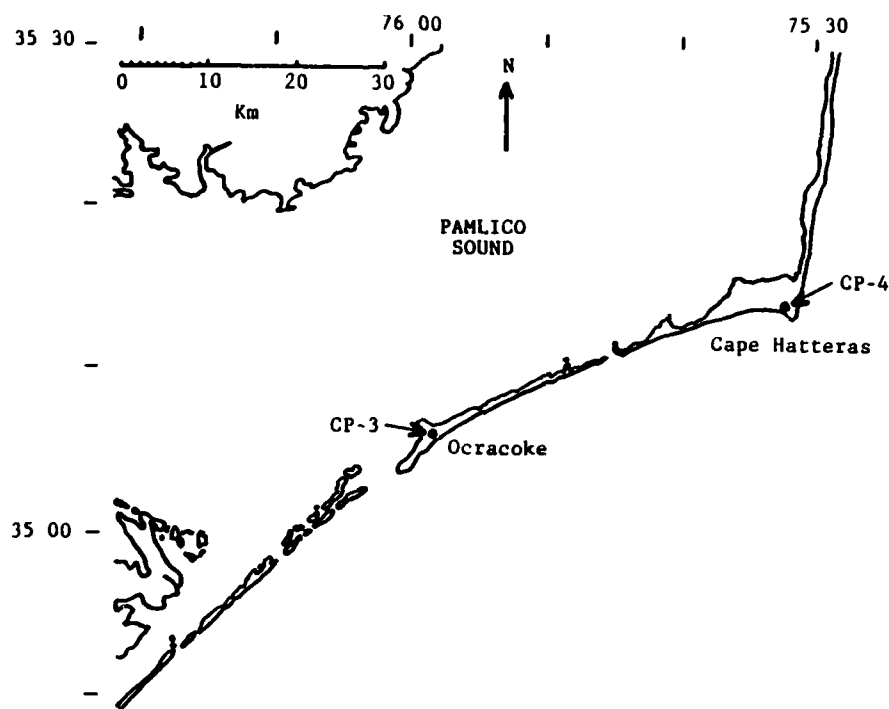


Figure 1.1 Location of the Doppler radars CP-3 and CP-4 along the Outer Banks of North Carolina during GALE.

Cold Air Outbreak (CAO). The single Doppler analysis technique referred to as Velocity Azimuth Display, henceforth VAD (Browning and Wexler, 1968), was used to attain numerical estimates for a variety of boundary layer properties. It is primarily upon these results that this study is based.

1.2 Literature Review

1.2.1 Doppler Radar Analysis Techniques

The original, most conformable and widely used single-Doppler technique is referred to as the Velocity Azimuth Display or VAD (Browning and Wexler, 1968) and is detailed in Section 3.3.1 of this thesis. Briefly, by scanning the radar beam about a vertical axis at a fixed elevation angle, harmonic analysis of the resultant curve fit to the plot of azimuth versus radial velocity yields estimates of the horizontal wind, divergence and deformation. The primary assumption is linearity of the wind field. Limitations of the VAD include the need to scan at relatively low elevation angles and restriction of the data analysis to moderate ranges. The work of Browning and Wexler is based upon previous works by Probert-Jones (1960), Lhermitte and Atlas (1961), Caton (1963), Atlas (1964), Lhermitte (1966) and Harrold (1966).

The VAD technique was further extended by Lhermitte (1968) and particularly by Wilson (1970) to attain estimates of second-order turbulent quantities. The vast majority of individual radial velocity data points attained during one revolution of the radar beam will deviate from the least-squares curve fit to that distribution of data.

These deviations are caused by local velocity variations related to the turbulent motion spectrum which can be described statistically by the variances and covariances of the longitudinal, lateral, and vertical components of atmospheric motions within the scan volume. Evaluations of these statistical quantities yields estimates of horizontal turbulent kinetic energy and vertical turbulent momentum flux, among others. Note that this technique is strongly dependent upon horizontal homogeneity of the wind field.

Although single-Doppler analysis represents a good tool for the observation of atmospheric motions, a more widely used and even more powerful analysis tool is that of dual-Doppler. Two basic variations of this scanning technique exist; a spatially and temporally synchronous scan referred to as COPLANE (Lhermitte and Miller, 1970; Miller and Strauch, 1974), and an asynchronous scanning technique referred to as a sector scan (Lhermitte, 1970). Both are briefly described in the following discussion.

The COPLANE technique involves a simultaneous scan by two coherent radars in a series of planes tilted about an axis along their baseline. Azimuth and elevation vary simultaneously in essentially a diagonal motion. The two radar beams are directed toward a common series of points in space. This synchronicity acts to greatly simplify the processing of the acquired data. The radial velocity equations from the two radars are combined with the integration of the mass continuity equation to yield three dimensional reconstruction of the wind field (three equations, three unknowns). Turbulence calculations are also possible with this technique. Note that while the post-experimental

data processing is much simpler than that of a sector scan, the strain imposed on the radar rotation mechanisms due to the simultaneous variation of azimuth and elevation often results in mechanical failures (Herzegh, 1986). Such malfunctions can be costly both to the experimental budget and in lost data acquisition potential.

The sector scan involves independent variation of elevation and azimuth over a precise scan volume of predetermined angular width and sequence of elevation angles. Points within the scan volume are not observed simultaneously, thus the acquired data is asynchronous. A correction scheme must be utilized to bring the data points to a common reference time. A correction technique is given by Gal-Chen (1982).

The single-Doppler analysis scheme has several advantages over dual-Doppler. Data acquisition and post-experimental processing for the former are neither as complex nor as expensive as for the latter. However, dual-Doppler analysis has the distinct advantage of achieving a two-dimensional reconstruction of the atmospheric flow pattern across either a horizontal or vertical plane. The analysis scheme selected by the user depends upon the desired results and experimental budget.

The analysis techniques discussed thus far represent the most widely accepted and utilized means of observing atmospheric kinematics. Since the early 1970's, Doppler radar observation techniques have grown in number and complexity. Many of the more recent developments remain either untested or have received limited use. A review of such techniques would represent an undertaking well beyond the scope of this thesis.

1.2.2 Characteristics of the Coastal Marine Atmospheric Boundary Layer (MABL)

The MABL differs from its terrestrial counterpart in several distinct aspects (LeMone, 1980). Because of the relatively high thermal capacity and low thermal conductivity characteristic of water, the magnitude and rate of sea-surface temperature (SST) change is much less than that of land. The sea surface also represents an unlimited source of moisture resulting in a virtually constant upward flux of water vapor and latent heat into the MABL. The air flowing over the sea surface modifies rather quickly, most often resulting in a nearly neutral thermal stratification for long fetches. A particular exception to this is the observed thermal instability characteristics of a Cold Air Outbreak (Raman, et al., 1986). Generalized behavior of the MABL during a Cold Air Outbreak (CAO) is described a bit further in this section of the thesis.

A commonly observed mesoscale circulation in the coastal MABL is the sea/land breeze, the result of a temperature difference between the land and water surfaces. Jeffreys (1922) was the first to address the basic dynamics of this phenomenon, recognizing that the circulation arises from the horizontal pressure gradient resulting from the unequal heating of the air above the surfaces of differing temperature. Both Schmidt (1946) and Haurwitz (1946) addressed the veering with time of the Northern hemisphere extratropical sea breeze, a result of the Coriolis force. Additionally, taking friction into account, maximum sea breeze intensity is achieved at approximately the same time as the maximum temperature difference between the land and water surfaces. In

the absence of friction, the sea breeze intensity would theoretically begin to diminish only when the land/water temperature difference had decreased to zero. More recently, an excellent review of the land/sea breeze was conducted by Atkinson (1981). Briefly, observations of this circulation phenomenon indicate a mean onset time around local noon, a duration of roughly 8 hours, a surface horizontal wind speed on the order of 5 meters per second, a vertical extent (lower limb) of several hundred meters and a total horizontal extent on the order of 100 kilometers. These values vary greatly as a function of latitude, the tropical sea breezes characteristically of greater intensity, spatial extent and duration.

A coastal region is typically characterized by discontinuities in surface roughness and/or temperature, primarily at the land/water interface. As air flows across such a discontinuity and if it is advected towards an area of increased roughness or temperature, an internal boundary layer forms (Elliot, 1958). The effect of a thermal discontinuity is typically much greater than that of a roughness discontinuity (Raynor, et al., 1979). Stunder and Raman (1985) reviewed and evaluated several formulations for calculating the height of the thermal internal boundary layer (TIBL) as a function of downwind distance from the surface discontinuity. It was found that the most important parameters for inclusion in such a formulation were horizontal wind speed, upwind lapse rate and downwind surface heat flux. Additionally, TIBL observations indicate a parabolic downwind growth.

Under conditions of moderately strong boundary layer winds and slight to moderate thermal instability, there commonly exists a linear

cellular convection pattern. The structure and dynamics this phenomenon, henceforth referred to as roll vortices, were well treated by LeMone (1973), the highlights of which follow. Evidence of such a boundary layer circulation is most readily observable in the form of linearly aligned rows of cumulus clouds or cloud streets. The horizontal spacing of the cloud streets, indicative of the roll vortex horizontal wavelength, is roughly three times the inversion height. The rolls are typically aligned 10 to 20 degrees to the left of the geostrophic wind and are characterized by lengths on the order of tens to hundreds of kilometers. The primary energy contributions to roll maintenance come from buoyancy and the cross-roll component of the mean PBL wind spiral. Roll vortices commonly occur in the MABL (LeMone, 1980).

Atlas, Chou and Byerly (1983) have shown coastline configuration to have a significant effect on the meso- β and lower end of the meso- α scale circulation pattern in the MABL during a CAO. Given a synoptic scale flow which roughly parallels that portion of the coastline downwind from a bend, and if the airflow upwind from that bend is predominately across a terrestrial surface, then the formation of a convergence zone along a line exactly downwind from that bend will be initiated by differential heating and moistening of the air flowing over the adjacent terrestrial and aqueous surfaces. The convergence zone acts to enhance the nearshore divergence and may contribute to offshore cyclogenesis.

1.2.3 Doppler Radar Studies of the Planetary Boundary Layer (PBL)

As reviewed by Kropfli (1983), the predominance of coherent radar studies of the PBL have been dual-Doppler observations of the clear-air

terrestrial convective boundary layer (CBL). Relatively few PBL studies have been single-Doppler or have involved the use of chaff as a reflective medium; such studies of the MABL are virtually nonexistent. The following discussion highlights the results of several papers which can be considered pertinent to the emphasis of this thesis.

Non-coherent radar observations of sea breeze fronts have been documented for nearly three decades (Atlas, 1960; Geotis, 1964; Meyer, 1971). Yanagisawa and Ishihara (1983) performed such observations along the east coast of Japan utilizing an X-band coherent radar. The Doppler velocity pattern within the approximately two kilometer wide linear echo revealed maximum wind speeds in the onshore direction of nearly 10 meters per second, horizontally centered on the echo between 200 and 400 meters Above Surface Level (ASL). As the sea breeze front passed over the 213 meter tower at the Meteorological Research Institute of Japan, comparison between tower wind sensing instruments and radar observations indicated agreement in wind speed and direction to within one tenth of a meter per second and two degrees in the azimuth, respectively.

Moninger and Kropfli (1982) observed the spatial and temporal variation of a chaff plume from an elevated stationary continuous point source utilizing an X-band coherent radar. Horizontal surfaces and vertical cross-sections of constant chaff density were contoured, revealing significant lateral and vertical variation of the plume to a downwind distance of 18 kilometers. Chaff density was correlated with reflectivity; no reference was made to the distribution of radial velocity.

Two prime examples of dual-Doppler clear air studies are by Doviak and Jobson (1979) and O'Bannon (1978). Though performed by different investigators at different locations, the atmospheric conditions under which the data sets were collected and the results achieved by each were virtually identical. Both utilized intrinsic tracers in the atmosphere to provide a return signal to the radar receiver. Data collection was performed in the dry Convective Boundary Layer (CBL) amidst mean boundary layer winds on the order of 5 ms^{-1} and a vertical shear of approximately $3 \times 10^{-3} \text{ s}^{-1}$ through the depth of the mixed layer. The perturbation or eddy field, attained by removing the mean wind from the total data field, revealed several interesting results. As would be expected, low altitudes show little or no organized cellular structure whereas with increasing altitude the perturbation field depicts greater organization and eddies of increasing scale lengths. Eddy sizes in the horizontal wind field were observed to vary between one and 15 kilometers over a 20 square kilometer region. Areas of simple convergence and divergence and counter-rotating vortices, as in flow around obstacles, were observed. Such behavior would be expected in a boundary layer characterized by moderate shear. Finally, weak echo interiors of cellular patterns suggested that refractive index fluctuations were a primary cause of the signal return.

Frisch, et al. (1976) attained results coincident with those mentioned above. The only significant difference was that chaff was utilized as the reflective medium. Under light wind conditions, dominant horizontal scale lengths of cellular structures were observed to range between 2 and 5 kilometers. Below approximately 400 meters ASL,

cell scales were essentially too small to be adequately detected by the radar network. Also, lower level divergence was coupled with upper level convergence and vice versa.

A study comparing temporally coincident VAD analyses performed by two S-band radars, separated by a distance of 40 kilometers, was performed by Rabin and Zrnic (1980) in the optically clear CBL under moderately strong winds averaging between 6 and 8 meters per second. Though many interesting results were presented, the revelation most pertinent to this study was the existence of an inverse relationship between the sampling area and the observed fluctuations in the divergence field. Essentially, the smaller the VAD analysis radius (less than 20 kilometers) the greater the temporal variation of divergence measurements, indicating that at such scales the cellular structures chiefly responsible for values of this kinematic property are of a transient nature. This finding is in agreement with that of Readings, et al. (1973) who documented, via X-band single Doppler radar measurements, the migration of hummocks atop the mixed layer capping inversion, each about 100 meters in amplitude, 500 meters in diameter and propagating at about 4 meters per second along the mean mixed layer wind. These hummocks were concluded to be a reflection of the upward limb of the convective cells occurring within the mixed layer beneath. The fact that these hummocks are essentially overshooting convective elements is supported by the findings of Caughey and Palmer (1979), a single-Doppler study which also revealed that sparseness of data above two-thirds the mixed layer depth is not uncommon and is attributable to

the effects of downward entrainment associated with the return flow between thermal plumes.

Kelly (1981) observed and documented boundary layer structure during a 1978 lake-effect snowstorm utilizing an S-band Doppler radar located two kilometers inland from the eastern shoreline of Lake Michigan. Amidst westerly winds of 12 to 14 ms^{-1} , radar observations revealed the presence of Longitudinal Horizontal Rolls (LHRs), often referred to as roll vortices (LeMone, 1973). Air temperatures obtained from a local sounding at a height of 160 meters ASL indicate an air/water thermal contrast on the order of 15 degrees Celsius. The reflectivity maxima, linearly oriented along the mean mixed layer wind, were horizontally spaced at between 3 and 5 kilometers. Along the bands of reflectivity maxima, strong convergence typified the lower third of the mixed layer with divergence dominating the upper third. As would be expected, varying the azimuth at constant elevation resulted in alternating bands of convergence and divergence.

A recent investigation by Atlas, et al. (1986) examined the structure of the unstable MABL as viewed by lidar and aircraft observations. The results were consistent with several of the findings discussed to this point. The lidar reflectivity was directly correlated with the concentration of sea salt aerosols (SSAs) and to a lesser extent with the flux of heat and moisture. Hence, updrafts were characterized by cores of high reflectivity with the converse true of downdrafts. The mixed layer flow was dominated by strong, well organized roll vortices or LHRs amidst a mean boundary layer wind from the north at approximately 12 ms^{-1} and an air/sea thermal contrast of 12 to 13 degrees

Celsius at 50 meters ASL. The strongest portions of the up and down-drafts were typically found just below mid-level of the mixed layer with magnitudes of between 2 and 4 ms^{-1} . The low-level convergence corresponding to these observed locally strong updrafts was likewise vigorous at $1-2 \times 10^{-2} \text{ s}^{-1}$. Local Entrainment Zones (LEZs) had amplitudes of 100 to 200 meters and a horizontal scale on the order of several hundred meters. These LEZs, occurring locally on the edges of the convective elements, were superimposed on capping inversion undulations with wavelengths of roughly two kilometers, consistent with the presence of LHRs. The roll axes were oriented north-south along the mean wind and asymmetrical, tilting eastward with increasing height. This asymmetry is attributable to the strong transverse shear. Those rolls having the vorticity of the shear were dominant.

With the exception of this treatise, there have been to date no single-Doppler MABL chaff studies. However, results of a dual-Doppler MABL chaff study were presented by Kropfli and Wilczak (1986). The objective was to gain insight into the details of the horizontal flow regime over Santa Barbara Channel, an area where ozone concentrations are periodically nearly twice the Federal ambient air quality standards. The shallow, stable MABL was probed by two Doppler radars located along the north shoreline of the channel and separated by a distance of 46 kilometers. Chaff was continuously released from two aircraft flying at an altitude of about 300 meters ASL. The reconstructed horizontal flow pattern was a composite of data collected over a period of several hours and well depicted the overwater mesoscale

eddy configuration. Validity of the results were strongly dependent upon the assumption of a quasi-stationary flow regime over the channel.

1.3 Objectives of This Study

The primary objectives governing the execution of this thesis are the analysis of:

1. temporal variations of the horizontal wind, vertical velocity, horizontal divergence and deformation in the coastal MABL over the period of several hours, and
2. spatial variations of the coastal MABL on a meso- γ and meso- β scale, and in particular the horizontal circulation patterns which arise under the particular synoptic conditions present during the data collection period.

These variations are important in that some are perhaps solely inherent to the coastal MABL.

Beyond the primary objectives, this thesis represents an excellent opportunity to illustrate the utility of a single Doppler radar as a remote sensing tool for gaining insight into MABL kinematics. The over water application is particularly interesting in that such studies have previously been essentially nonexistent.

2. EXPERIMENTAL DESIGN

2.1 Radar Characteristics

The principle characteristics of the two pulsed Doppler radars employed in this study, CP-3 and CP-4, are virtually identical and are listed in Table 2.1 (GALE, 1985).

Table 2.1 Principle Characteristics of the Doppler Radars
Used in the 8 March 1986 MABL Study

Radar Characteristic	Parameter Value
Wavelength (λ)	5.46 centimeters
Pulse duration (τ)	1 microsecond
Range resolution (Δr)	150 meters
Peak transmitting power	400 kilowatts
Angular beamwidth (ϕ)	1.1 degrees
Range gate length (l)	150 meters
Pulse repetition frequency (PRF)	625 to 1667 pulses per second
Number of range gates	256 to 1024
Number of pulses per sample (N)	16 to 1024
Azimuth rotation rate (α)	0 to 25 degrees per second
Elevation rotation rate	0 to 15 degrees per second

Note that the last five parameters are variable. Choosing the appropriate parameter value involves making certain "tradeoffs." Details of this topic are addressed in the following section.

2.2 Selection of Values for Radar Variables

There are essentially five variable radar parameters for which values must be selected. They include pulse repetition frequency, number of range gates, number of pulses per sample, azimuth rotation rate, and elevation rotation rate. The last of these, elevation rotation rate, is not of direct concern for a VAD analysis in which elevation increments are very small. Such is the case for this study as the largest elevation increment is only 0.5 degrees. However, the first four variables are relevant to the design of this experiment, the discussion of which follows.

The PRF is, as the name implies, the frequency at which pulses of microwave energy are transmitted by the radar. This parameter affects three aspects of the experimental design, as discussed below.

The first two effects are related and can be addressed concurrently. The PRF is directly proportional to the maximum velocity which can be unambiguously measured by the radar and is inversely proportional to the maximum range to which data can be acquired. This is shown mathematically by equations 1 and 2 (Battan, 1981).

$$V_{\max} = (\text{PRF}) \frac{\lambda}{4} \quad (1)$$

$$r_{\max} = \frac{1}{2}(c/\text{PRF}) \quad (2)$$

The inverse nature of these relationships represents a compromising situation. The greater the maximum range of data acquisition, the lower the velocity which can be unambiguously measured. To achieve an

optimal dataset, the environmental conditions particular to the study period must be of prime consideration in determining the PRF value. As stated previously, the dataset applicable to this study was acquired during the latter stages of a CAO. A typical midlatitude value for MABL height (h) during such conditions would not be expected to exceed a value on the order of 1000 meters for the region between shore and cloud edge (Stage, 1983). Given a boundary layer circulation pattern having a vertical scale length consistent with the MABL height scale, an example of which are roll vortices (LeMone, 1973), then the minimum sampling interval must be no less than $2h$ for unambiguous structure recovery. This is referred to as the Nyquist rate (Stanley, et al., 1984). Hence, for this study the maximum allowable beamwidth would be approximately 500 meters which, for an angular beamwidth of 1.1 degrees, occurs at a horizontal range of about 29 kilometers. Given a PRF of 1667 pps, the corresponding r_{\max} value is 90 kilometers, exceeding the range requirements of this study by a factor of three. The V_{\max} resulting from a 1667 pps PRF is 22.8 meters per second. Considering that such a windspeed represents a gale force wind, this limit is also exceedingly sufficient.

A range gate is simply a data storage space. The radar receiver instantaneously measures the frequency shift of the backscattered electromagnetic pulses at spatial intervals of 150 meters which corresponds to a temporal interval of 0.5 microseconds. The product of the range gate length and number of range gates yields the range to which data is collected. Considering that the maximum range of desirable data was determined to be on the order of 30 kilometers, the minimum number of

gates, 256, was selected as it results in a data collection range of 38.4 kilometers. The fewest number of range gates is desirable in that as the number of gates increases, the required storage space also increases. Essentially, this is one means of controlling expenses.

The number of pulses per sample (N) is inversely related to both the statistical uncertainty of V_r and the potential number of data points per revolution. Once again, a compromising situation exists for the determination of a radar variable. A low number of pulses per sample yields a relatively large number of potential data points yet results in a relatively high statistical uncertainty of V_r . A more quantitative discussion of these effects can be found in Section 3.1 of this thesis.

The azimuth rotation rate (α) of the radar antenna affects the potential number of data points in any given revolution and the temporal resolution of the VAD scan volume. A large α results in a relatively small number of potential data points. The fewer the data points the poorer the spatial resolution. However, a large α also results in a VAD scan volume of relatively short duration. The more quickly a volume of atmosphere is observed the less variability in the kinematic properties characteristic of that volume. The result is enhanced temporal resolution. In determining an appropriate α , the experimental designers sought to keep the distance over which the air flow pattern would be displaced during the course of a VAD scan volume roughly an order of magnitude less than the diameter of that scan volume. Anticipating a VAD analysis radius of not less than 5 kilometers and a mean MABL horizontal windspeed on the order of 4 meters per second, an α of

15 degrees per second with a maximum of 15 elevation increments (resulting in a 6 minute scan volume duration) would allow for an air flow pattern displacement of 1440 meters. Hence, given the above circumstances, an α of 15 degrees per second was deemed sufficiently fast to insure adequate temporal resolution.

The azimuth rotation rate also affects the variance of the Doppler spectrum. The details of the topic are discussed in Section 3.3.1.1 of this thesis, "Inherent Errors."

2.3 Chaff Dispersal

In the case of a CAO, the height of the mixed layer is well defined by the presence of a subsidence inversion. In the absence of hydrometeors, chaff must be dispersed by aircraft to provide backscattering of the transmitted microwave pulses. The chaff utilized in this study was aluminum coated strands of mylar, 25 microns in diameter, cut in lengths equal to half the transmission wavelength of the radar. The aluminum coating acts to enhance the reflectivity while the half wavelength maximizes resonance, further enhancing the signal return. Its terminal fall speed is approximately 0.3 meters per second.

Five lines of chaff were released by aircraft beginning at 1746 GMT. The chaff dispersal aircraft flew at an altitude of approximately 500 meters, mid-level of the mixed layer, along an east-west line roughly 55 kilometers in length. Figure 2.1 illustrates the location of the flight track.

Selection of the flight track location was based on several considerations. Advection of the chaff into the radar network is most

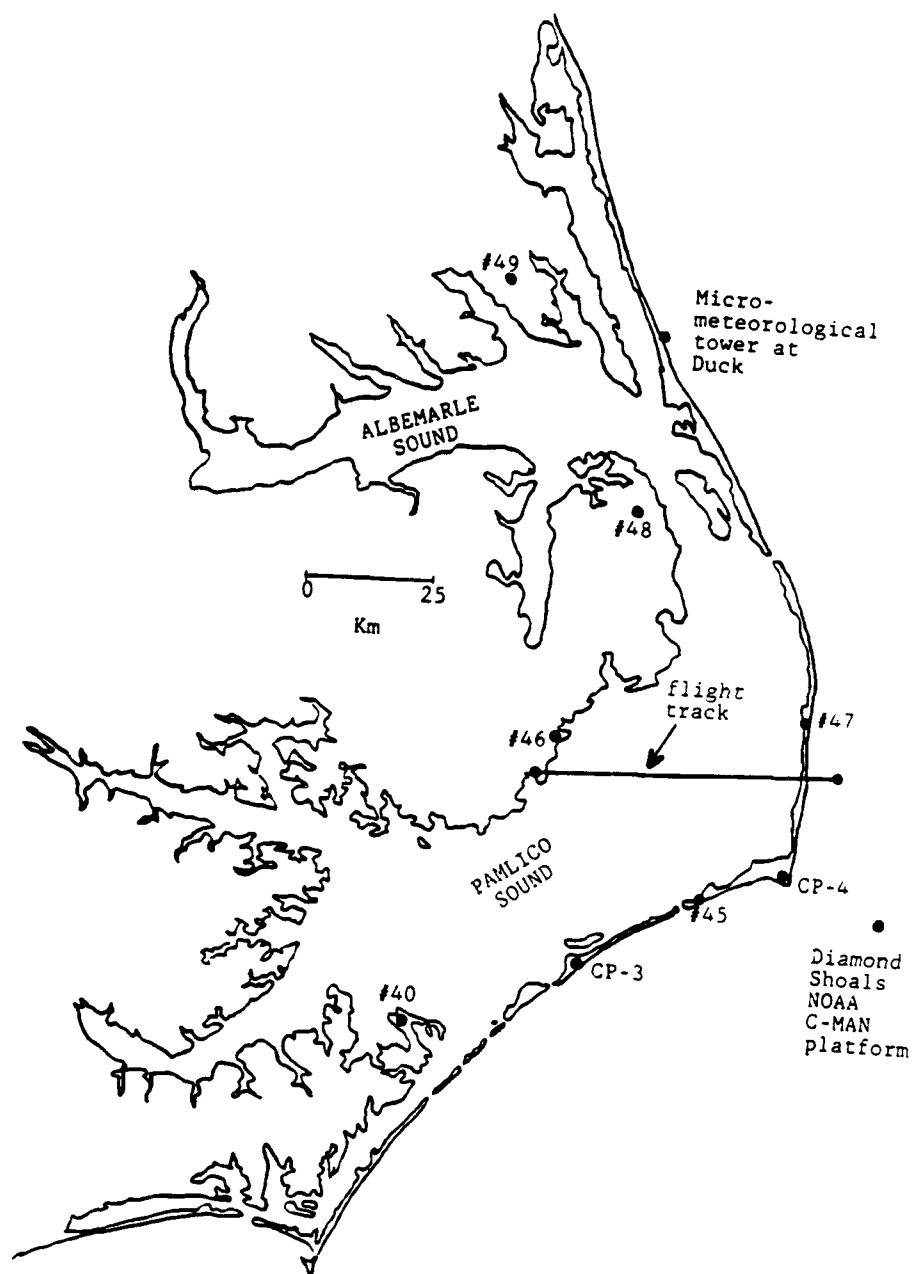


Figure 2.1 Location of the chaff dispersal flight track for the 8 March 1986 MABL study.

effective if the line orientation is orthogonal to the mean boundary layer wind. The length of the line was designed such that, after being advected into the radar coverage area, the chaff would provide echo over a range of at least 15 to 20 kilometers around each radar. The minimum upwind distance for release of the chaff is a function of the expected rate of diffusion by means of turbulent mixing. From communication with several radar meteorologists who have conducted similar experiments, an upwind temporal distance of 40 minutes was considered to be sufficient to insure thorough diffusion of chaff within the MABL. Assuming a mean boundary layer wind speed on the order of 4 meters per second, an upwind temporal distance of 40 minutes then corresponds to a spatial distance of roughly 10 kilometers. The minimum distance between the point of chaff release and the CP-4 radar was approximately 15 kilometers.

The scan description and listing for this case study are detailed in Section 5.1.2, the discussion of VAD analysis results.

3. DATA ACQUISITION

3.1 Rawinsonde

The National Weather Service (NWS) office at Buxton, North Carolina, collected upper air temperature, humidity and wind data at three hour intervals from 1800 GMT on 8 March 1986 until 0000 GMT on 9 March 1986. The Buxton location was roughly a kilometer away from the CP-4 radar site during GALE. The proximity of the acquired rawinsonde data allows for the utilization of derived temperature and humidity profiles as a means of calculating the magnitude of boundary layer stability parameters during the 8 March radar study. These results are discussed in Section 5.1.1 of this writing.

3.2 Portable Automated Mesonet (PAM)

The PAM system is, as the name implies, an automated surface observation network providing high temporal resolution measurements of all standard meteorological variables (Dirks, et al., 1988). The PAM stations were placed in a gridded pattern, primarily in the eastern portions of the Carolinas, and were separated by horizontal distances on the order of 50 kilometers. Figure 3.1 depicts the locations of PAM stations in the vicinity of the radar network. Also shown in this figure are the locations of the micrometeorological tower at Duck, North Carolina, and the National Oceanic and Atmospheric Administration (NOAA) Coastal-Marine Automated Network (C-MAN) platform at Diamond Shoals.

Half-hourly plots of the meso- β winds during the study period were constructed from these data sources and are discussed in Section 4.3 of

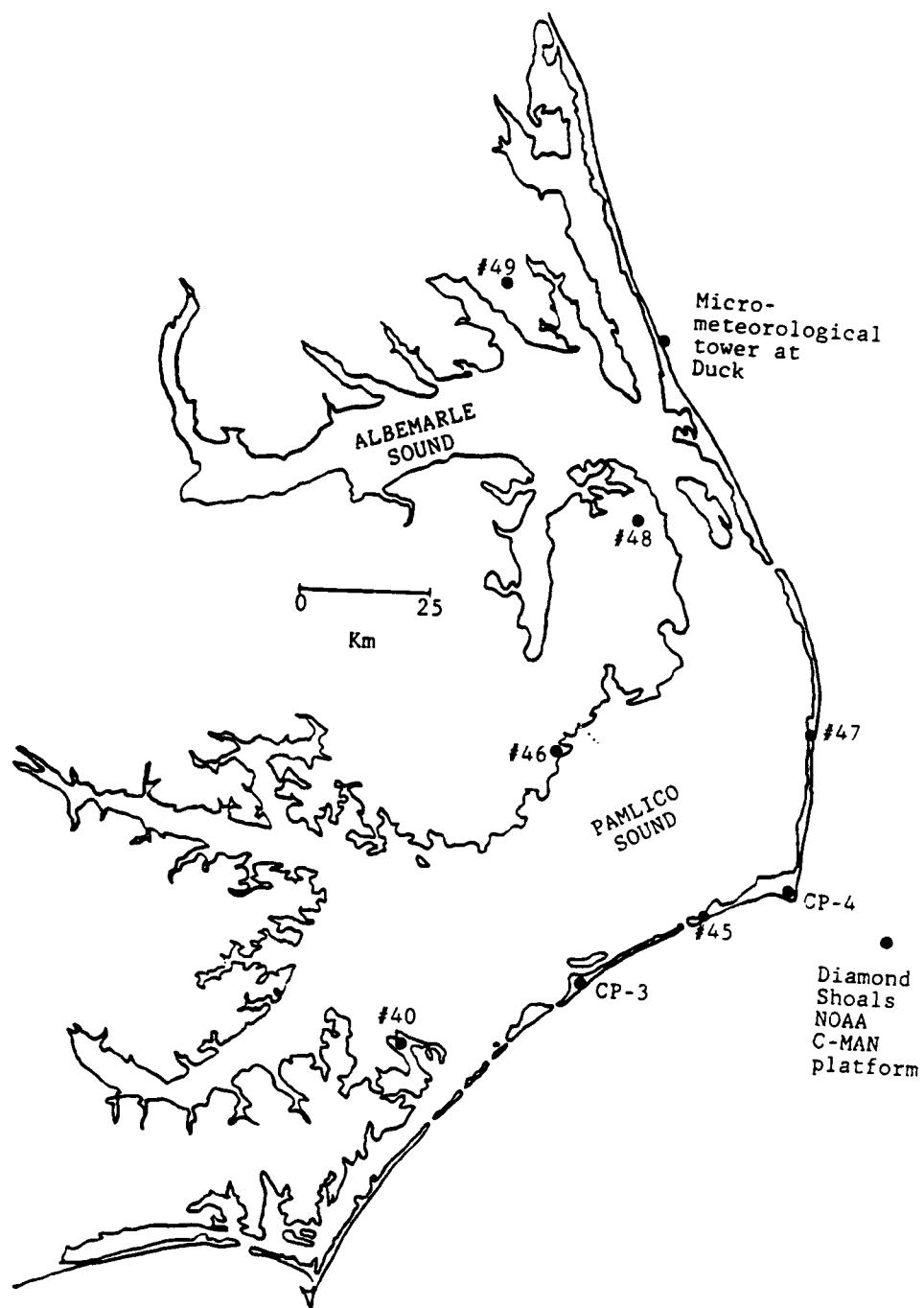


Figure 3.1 Location of PAM stations 40 and 45 through 49, the micrometeorological tower at Duck and the Diamond Shoals NOAA C-MAN platform.

this thesis. Additionally, Sea Surface Temperature (SST) distribution maps for Pamlico Sound, the Atlantic shelfwaters and the Gulf Stream are presented in Section 4.4.

3.3 Doppler Radar

3.3.1 Description of the Velocity Azimuth Display (VAD) Technique

If there are scatterers present in the atmosphere to provide signal return to the radar receiver, a Doppler radar can measure their instantaneous velocities along the direction of the radar beam. This velocity measurement is known as radial velocity, V_r , and is a measure of the Doppler frequency shift of the electromagnetic wave pulses, transmitted by the radar, resulting from the motion of the scatterers or "targets," relative to the radar. The radial velocity measurement represents a spatially weighted average of all scatterers present in the pulse volume. The strongest return value is received from the center of the pulse volume and decreases linearly with increasing distance from the center point. Numerically averaging the results of a pre-specified number of consecutive pulses yields a single data point, sometimes referred to as a beam of data. A pulse repetition frequency (PRF) of 1667 pulses per second (pps) equates to a pulse transmitted every 0.6 milliseconds. Multiplying this value with a pulse per sample value of 64 results in a beam of data taken every 38.4 milliseconds. Taking the product of this value and an azimuth rotation rate of 15 degrees per second yields a radar beam azimuthal rotation of 0.576 degrees per beam of data. Hence, a maximum of 625 beams per revolution are possible, given the parameter values used for these calculations.

The VAD technique represents a means of quantifying a variety of kinematic properties of the wind field in the vicinity of a pulsed Doppler radar. These properties include horizontal wind speed and direction, vertical velocity, horizontal divergence, and stretching and shearing deformation. The radar beam is rotated over 2π radians about a vertical axis while holding constant the elevation angle, relative to horizontal. By extracting the signal return, in the manner previously described, from the "range gate" (see Section 3.2) most closely corresponding to the desired horizontal range, a plot of radial velocity versus azimuth is attained. Assuming a wind field which roughly approximates horizontal homogeneity, such an output resembles a sinusoidal curve which is a periodic function. Mathematically this is represented by a Fourier series with a period of 2π . Solution of the Fourier coefficients through the second order terms yields values for the horizontal kinematic properties previously listed. Details of this procedure will be addressed at a point further in this section of the thesis.

The basic equation for radial velocity can be expressed in the form (Lilly, 1983),

$$V_r = (u \cos \beta + v \sin \beta) \cos \theta + w \sin \theta, \quad (3)$$

where β is the azimuth angle, measured counterclockwise from east, and θ is the elevation angle, measured upward from the horizon. Assume a wind field which varies linearly across a horizontal plane and has a value of zero at the center. This is represented mathematically by a first order Maclaurin series, given by equations 4 through 6.

$$u = u_0 + x \frac{\partial u}{\partial x} + y \frac{\partial u}{\partial y} \quad (4)$$

$$v = v_0 + x \frac{\partial v}{\partial x} + y \frac{\partial v}{\partial y} \quad (5)$$

$$w = w_0 + x \frac{\partial w}{\partial x} + y \frac{\partial w}{\partial y} \quad (6)$$

Substituting the above equations into equation 3 yields an equation for radial velocity in a linear wind field, equation 7.

$$\begin{aligned} V_r = & w_0 \sin \theta + \frac{\partial w}{\partial x} x \sin \theta + \frac{\partial w}{\partial y} y \sin \theta \\ & + u_0 \sin \beta \cos \theta + \frac{\partial u}{\partial x} x \sin \beta \cos \theta \\ & + \frac{\partial u}{\partial y} y \sin \beta \cos \theta + v_0 \cos \beta \cos \theta \\ & + \frac{\partial v}{\partial x} x \cos \beta \cos \theta + \frac{\partial v}{\partial y} y \cos \beta \cos \theta \end{aligned} \quad (7)$$

Now substitute $x = r \cos \theta \sin \beta$ and $y = r \cos \theta \cos \beta$, where r is horizontal range, into equation 7. After extensive algebra and trigonometric substitution, a V_r formulation in spherical coordinates for a linear horizontal wind field is achieved, equation 8.

$$\begin{aligned} V_r = & w_0 \sin \theta + \frac{1}{2} r \cos^2 \theta \left(\frac{\partial u}{\partial x} + \frac{\partial v}{\partial y} \right) \\ & + \frac{1}{2} r \cos^2 \theta \cos 2\beta \left(\frac{\partial v}{\partial y} - \frac{\partial u}{\partial x} \right) \\ & + \left(\frac{\partial w}{\partial x} r \sin \theta + u_0 \right) \sin \beta \cos \theta \end{aligned}$$

$$\begin{aligned}
& + \left(\frac{\partial w}{\partial y} r \sin \theta + v_0 \right) \cos \beta \cos \theta \\
& + \frac{1}{2} r \cos^2 \theta \sin 2\beta \left(\frac{\partial v}{\partial x} + \frac{\partial u}{\partial y} \right)
\end{aligned} \tag{8}$$

Allowing $V_r(\beta)$ to be the periodic function, with a period of 2π , and holding r and θ constant, the corresponding Fourier series is given by equations 9 through 12.

$$V_r(\beta) = a_0 + \sum_{n=1}^{\infty} [a_n \cos(n\beta) + b_n \sin(n\beta)] \tag{9}$$

$$a_0 = \frac{1}{2\pi} \int_0^{2\pi} V_r d\beta \tag{10}$$

$$a_n = \frac{1}{\pi} \int_0^{2\pi} V_r \cos(n\beta) d\beta \tag{11}$$

$$b_n = \frac{1}{\pi} \int_0^{2\pi} V_r \sin(n\beta) d\beta \tag{12}$$

Values of the coefficients a_0 , a_n , and b_n are calculated by a least-squares fit to the radial velocity versus azimuth data for a given revolution or sweep. The analytic function for V_r , equation 8, is then substituted into equations 10 through 12. Equations 11 and 12 are evaluated through the second order terms. Such an approach results in estimates of horizontal divergence, the v and u components of the horizontal wind, stretching and shearing deformation from solution of the

coefficients a_0 , a_1 , b_1 , a_2 , and b_2 , respectively. The resultant formulations are given by equations 13 through 17.

$$\text{horizontal divergence} \equiv \left(\frac{\partial u}{\partial x} + \frac{\partial v}{\partial y} \right) = \frac{2(a_0 - w_0 \sin \theta)}{r \cos^2 \theta} \quad (13)$$

$$v_0 = \frac{a_1 - r \sin \theta \cos \theta \frac{\partial w}{\partial y}}{\cos \theta} \quad (14)$$

$$u_0 = \frac{b_1 - r \sin \theta \cos \theta \frac{\partial w}{\partial x}}{\cos \theta} \quad (15)$$

$$\text{stretching deformation} \equiv \left(\frac{\partial u}{\partial x} - \frac{\partial v}{\partial y} \right) = \frac{-2a_2}{r \cos^2 \theta} \quad (16)$$

$$\text{shearing deformation} \equiv \left(\frac{\partial u}{\partial y} - \frac{\partial v}{\partial x} \right) = \frac{2b_2}{r \cos^2 \theta} \quad (17)$$

Note that only stretching deformation was utilized in this study. Also note that given a low elevation angle or a small $\frac{\partial w}{\partial y}$ and $\frac{\partial w}{\partial x}$, equations 14 and 15 can be simplified to those given by equations 18 and 19.

$$v_0 \approx \frac{a_1}{\cos \theta} \quad (18)$$

$$u_0 \approx \frac{b_1}{\cos \theta} \quad (19)$$

The value estimates of the VAD-derived kinematic properties are spatially located at the center of the horizontal circle around which the

functions are integrated. The author would like to note that the derivation of the VAD technique to this point was achieved through personal communication with R. E. Marshall.

Vertical velocity is one property of motion which cannot be directly estimated by the VAD technique. However, such an estimate is attainable through modification of the horizontal divergence formulation. Assuming stationarity of the mass density field, the resultant form of the mass continuity equation can be substituted into equation 13 to achieve (Doviak and Zrnic, 1984)

$$\frac{\partial}{\partial z}(\rho w_0) = \frac{-2\rho}{r\cos^2\theta}(a_0 - w_0\sin\theta). \quad (20)$$

Equation 20 can be solved analytically, given an estimate of w_0 at some height z_1 , the solution of which is given by

$$\begin{aligned} \rho w_0 = & \exp\left[-\int_{z_1}^z P(z)dz\right] \int_{z_1}^z Q(z) \exp\left[\int_{z_1}^z P(z)dz\right] dz \\ & + \rho w_0(z_1) \exp\left[-\int_{z_1}^z P(z)dz\right], \end{aligned} \quad (21)$$

where $P(z) = -2\sin\theta/r\cos^2\theta$ and $Q(z) = 2\rho a_0/r\cos^2\theta$ (Doviak and Zrnic, 1984). The boundary condition $w_0 = 0$ at $z_1 = 0$ was utilized in the analysis of this dataset.

3.3.1.1 Inherent Errors. A variety of error sources are inherent not only in the VAD technique, but in Doppler radar measurements of atmospheric motions in general. In this section of the thesis, a

description of these errors and the applicability of each to the acquired VAD dataset will be addressed.

The spatial beamwidth (d) is a function of angular beamwidth (ϕ) and slant range (SR), where slant range is the distance between the radar and the target along the beam axis. Equation 22 mathematically represents this relationship.

$$d = 2[SR \tan(\phi/2)] \quad (22)$$

The spatial beamwidth corresponding to the VAD analysis radii of 5, 10 and 15 kilometers are 96, 192 and 288 meters, respectively. Thus, pulse dimensions extend 48, 96 and 144 meters above and below the altitude of the radar beam axis for those ranges of VAD analysis. Essentially, spatial resolution decreases linearly with increasing slant range.

The statistical uncertainty of the radial velocity measurement for each beam of data, σ_{V_r} , is a function of the radar transmission wavelength, pulse repetition frequency and number of pulses per sample (Dennenberg, 1971).

$$\sigma_{V_r} = \left[\frac{0.9(\lambda)(PRF)}{8\sqrt{\pi}(N)} \right]^{\frac{1}{2}} \quad (23)$$

For a PRF of 1667 and a N of 64, the statistical uncertainty has a value of 0.30 meters per second.

Another error source is the increase in variance of the Doppler spectrum resulting from the azimuth rotation rate of the radar antenna (Doviak and Zrnic, 1984).

$$\sigma_{\alpha}^2 = (\alpha \lambda \cos \theta / 2\pi \phi)^2 \ln 2 \quad (24)$$

Doppler spectrum refers to the distribution of frequency shifts resulting from the backscattering of the transmitted radar signal by all scatterers present in a pulse volume. The increased variance associated with α can be directly related to a diminished accuracy of the radial velocity measurement. From the above formulation, the Doppler spectrum variance corresponding to the rotation rate of 15 degrees per second and the low elevation angles used in this study was calculated to be $0.010 \text{ m}^2 \text{ s}^{-2}$.

By taking the square root of the sum of $(\sigma_{V_r})^2$ and σ_{α}^2 , a combined standard deviation of 0.32 ms^{-1} for any given pulse volume can be attributed to the radial velocity data. This uncertainty is particularly alarming when considering that typical vertical velocities for this study are of the same order of magnitude. However, the results of an informal study conducted at NCAR FOF indicate that such uncertainties are random in space and when averaged over a scan, they tend to become very small (Herzogh, 1987).

Inaccuracies in beam position due to azimuthal or elevation position inaccuracy, $\delta\phi$, will result in what has been referred to as Doppler bias error, δ_v (Doviak, et al., 1976).

$$\delta_v = K_{\phi} r (\delta\phi) \quad (25)$$

In the above equation, K_{ϕ} is the azimuthal or vertical wind shear of the Doppler velocity. During the 8 March study, maximum beam position inaccuracies for CP-3 and CP-4 were approximately 0.05 degrees and 0.2

degrees, respectively (technical note from P. Herzegh). A study of wind gradients in convective storms showed that, for rainshowers, a median value of observed radial and tangential shear within the convective boundary layer (CBL) was on the order of $3 \text{ to } 5 \times 10^{-3} \text{ s}^{-1}$ over a scale length of 150 meters (Battan and Theiss, 1971; Donaldson, et al., 1972). Vertical velocities within the CBL, corresponding to convective activity of this intensity, are typically on the order of a few meters per second (Wallace and Hobbs, 1977). However, vertical velocities within MABL circulation patterns during a CAO on 2 March 1986, from dual Doppler analysis by CP-3 and CP-4, were roughly an order of magnitude less (Marshall, 1987). Assuming that the observed shear over the same scale length and altitude range is also an order of magnitude less, then an approximate value of 4×10^{-4} per second can be assigned to K_ϕ for this study. Using this value, the previously referenced antenna inaccuracies and the appropriate VAD analysis ranges, the corresponding maximum Doppler bias error ranged from 0.002 to 0.005 meters per second for CP-3 and 0.007 meters per second for CP-4.

Even in a weakly convective boundary layer, deviations from linearity of the actual wind field may result from cellular structures of a meso- γ scale (Waldteufel and Corbin, 1979). Divergence and vertical velocity values derived by a VAD analysis may differ from those characteristic of the surrounding meso- β wind field. The amount by which these will differ depends upon the spatial extent of the cellular structure, its proximity to the VAD scan volume and the intensity of its circulation. Such contamination of divergence and vertical

velocity values would be difficult to quantify. However, deviations from anticipated results, perhaps best depicted by the time-height plots of each of these kinematic properties, would indicate the possibility of such an occurrence.

Other sources of error include inhomogeneities in the horizontal distribution of precipitation fall speeds and reflectivity inhomogeneities. Neither is applicable to the results of this study as the chaff filaments are uniform.

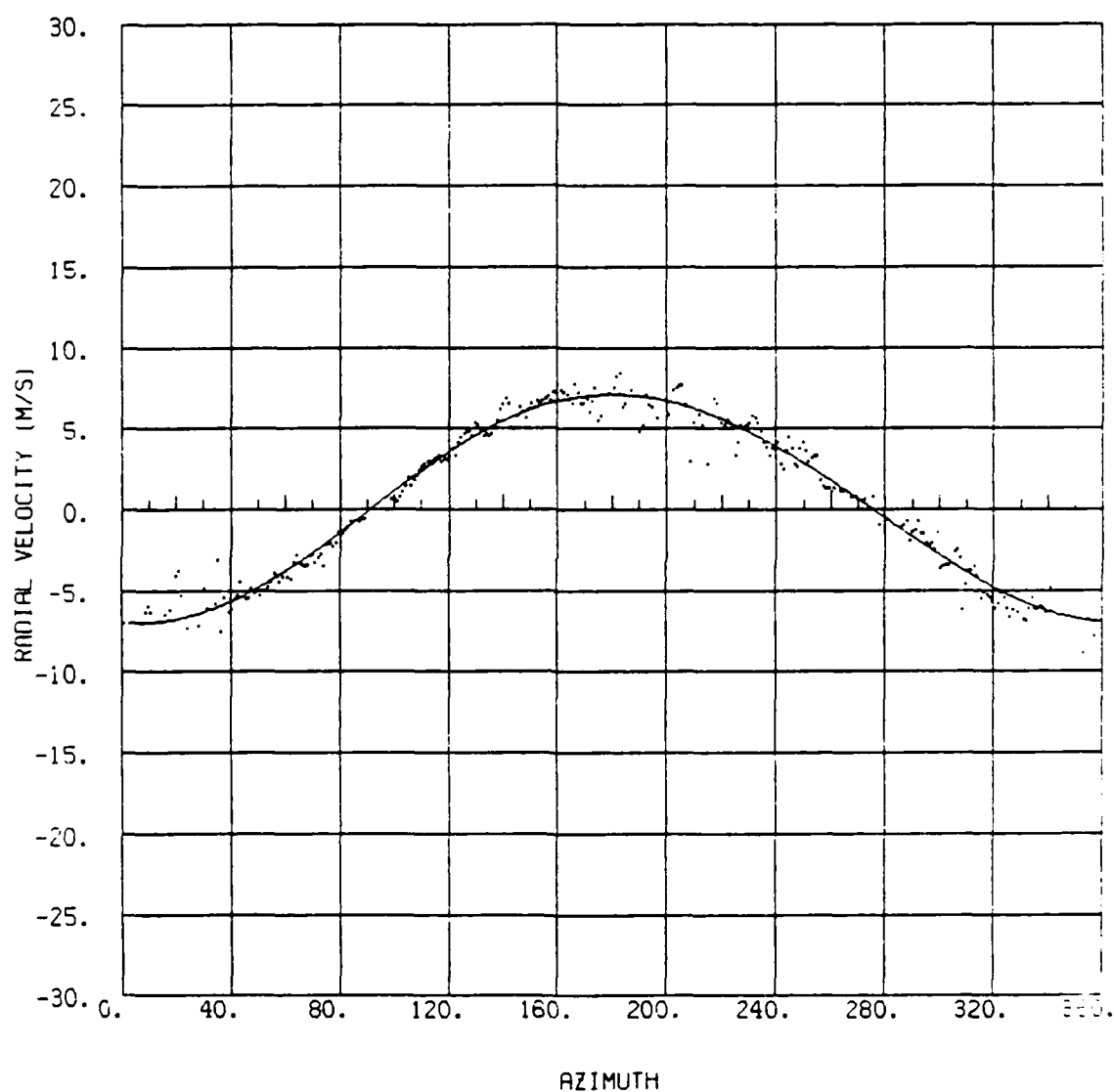
3.3.1.2 Data Editing. Post-experimental processing of radar field data from this study was conducted at the NCAR FOF facility in Boulder, Colorado. The software utilized by this agency allows for editing of data during the curve fitting portion of the VAD analysis. As previously mentioned, a least-squares curve is fit to the plot of radial velocity versus azimuth. After the initial curve fitting, the data is edited, and the curve is adjusted to reflect any changes in the distribution of data points about the first curve. The default editing specifications were applied to this dataset, under the advice of NCAR scientists. All data points beyond 2.5 standard deviations from the initial curve and those with a value of less than ± 0.5 meters per second were deleted. The former is simply a means of eliminating any points which radically depart from the first curve; the latter is an attempt to eliminate the effects of ground clutter as, in the case of terrestrial source, such returns result from scatterers which are fixed in position relative to the radar and are thus indicated by a radial velocity value of zero. Spurious returns resulting from ocean surface

waves would be very difficult to edit, due to the fact that they are in motion relative to the radar receiver, and most likely could only be done manually, if at all. However, considering the relative position of such scatterers within the pulse volume, their low profiles and the relatively small portion of the pulse volume which would be occupied by such undesirable targets, their effect on the dataset will be minimally weighted and only present at very low elevation angles.

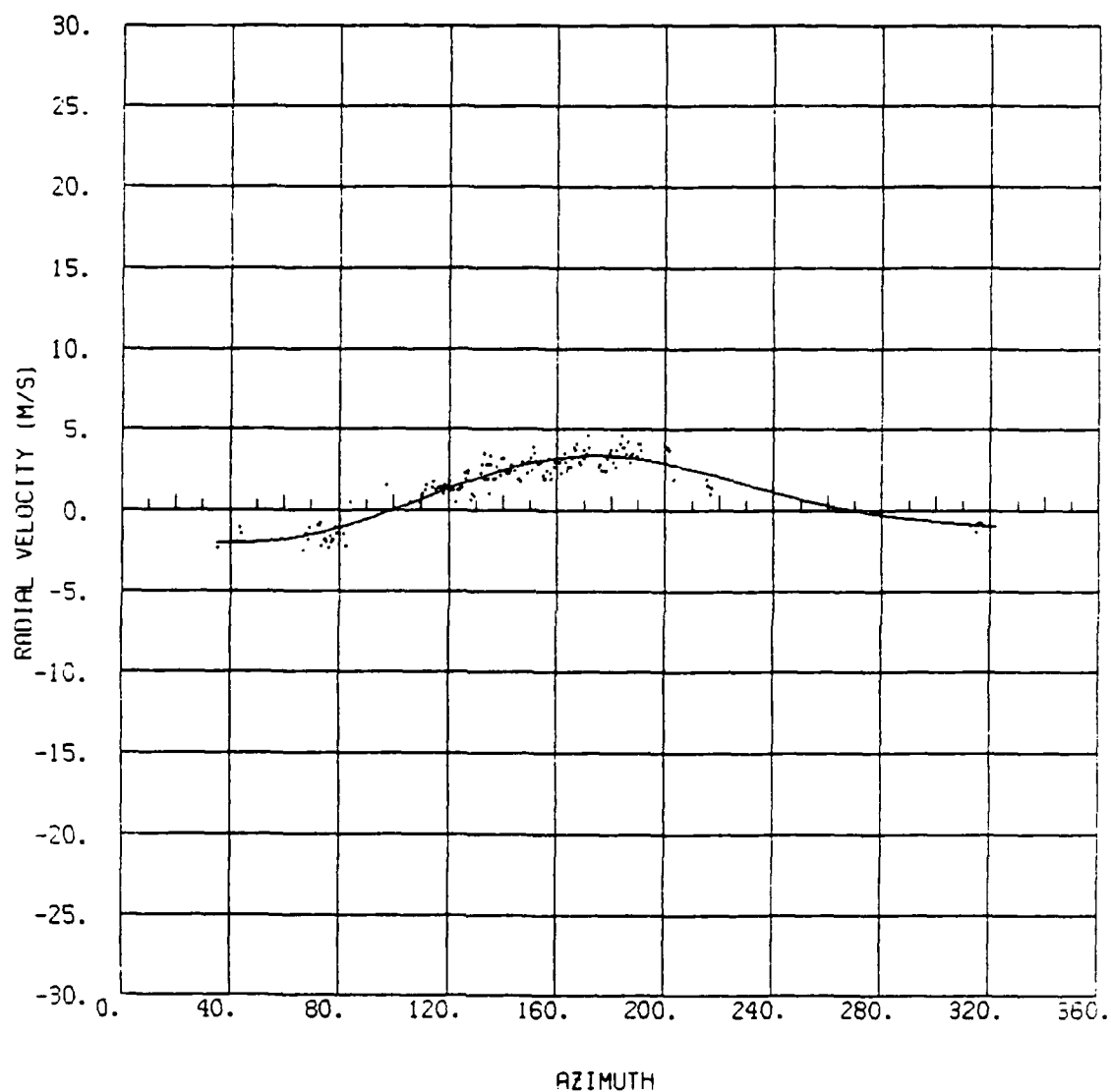
Following completion of the VAD analyses, a manual form of editing was employed. The ratio of data points remaining after the automated editing procedure to the total number of beams per revolution was calculated for each scan. If this ratio was $2/3$ or better, the resultant kinematic property estimates were accepted unconditionally, again based upon the recommendation of NCAR FOF scientists. Ratios of less than $2/3$ were examined on a case by case basis. If the data points were distributed over a wide range of azimuthal variation such that a good curve fit was obtained, the scan results in question were retained. This is a qualitative and arbitrary means of editing but, in the absence of a better alternative was considered sufficient. Figures 3.2a through 3.2c depict an unconditionally accepted scan, a conditionally accepted scan and a rejected scan, respectively.

3.3.2 Description of the Vertical Slice (VSLICE) Technique

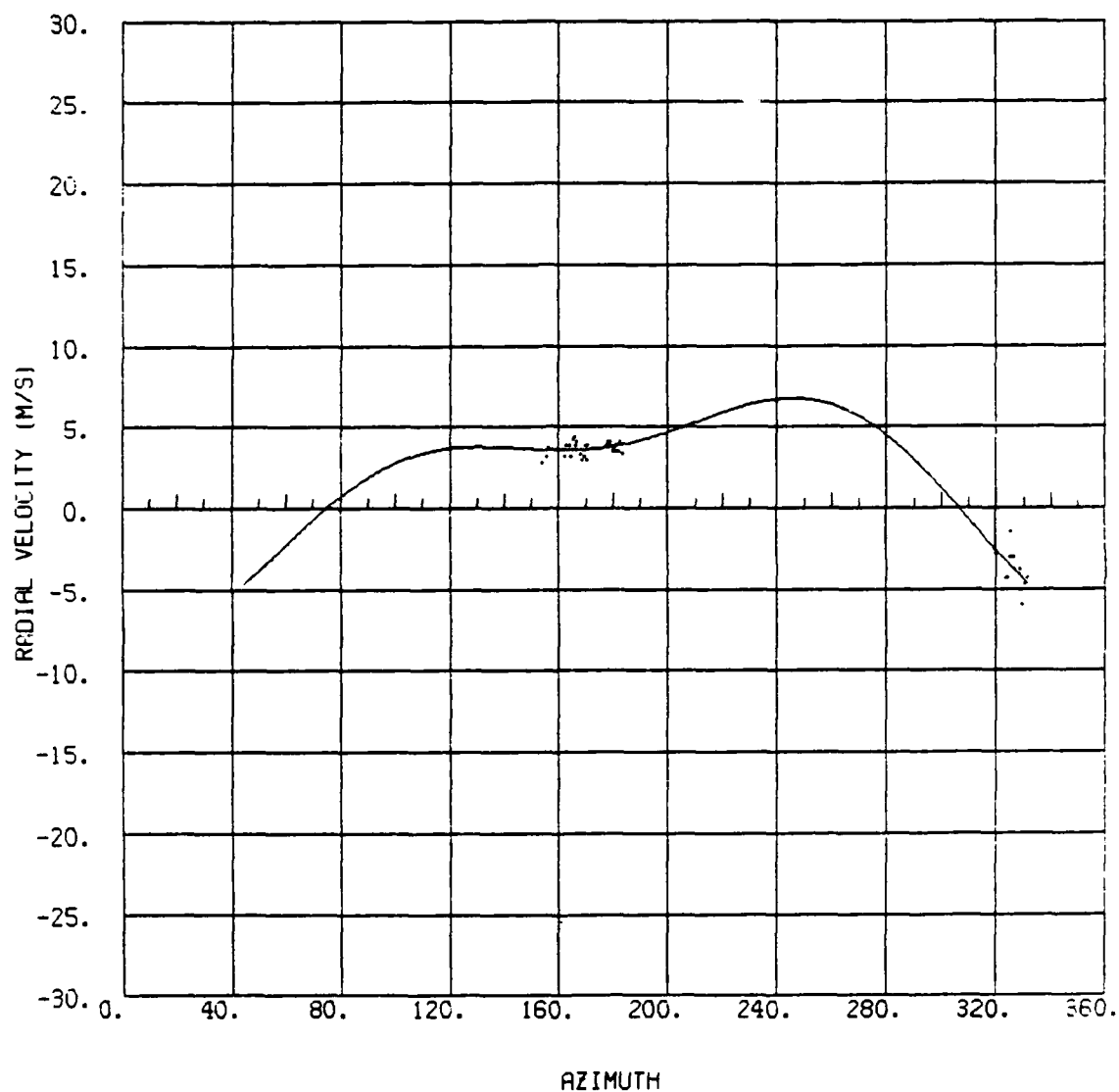
The VSLICE is, as the name implies, a cross sectional representation of the atmosphere depicting the distribution pattern of either radial velocity or reflectivity across a vertically oriented plane. The endpoints are user designated and can be anywhere within the



3.2a Plot of radial velocity versus azimuth from the 4.8 degree scan, VAD radius of 5 kilometers taken by the CP-4 radar at 1835 GMT, 8 March 1986. Seventy-seven percent of the possible data points remained after editing; this scan was unconditionally accepted.



3.2b Plot of radial velocity versus azimuth from the 2.4 degree scan, VAD radius of 15 kilometers taken by the CP-3 radar at 2106 GMT, 8 March 1986. Thirty-three percent of the possible data points remained after editing; this scan was conditionally accepted.



3.2c Plot of radial velocity versus azimuth from the 3.2 degree scan, VAD radius of 15 kilometers taken by the CP-3 radar at 2108 GMT, 8 March 1986. Eight percent of the possible data points remained after editing; this scan was rejected.

radars' range of data collection. The VSLICE is an unpublished data display technique developed by Jonathan Corbett of NCAR FOF, a qualitative description of which follows.

The selection of two endpoints, in combination with a user specified lower and upper limit of vertical extent, defines the boundaries of the vertical plane. Each point within this plane can be specified in spherical coordinates, relative to the radar. Radial velocity or reflectivity data from the range gate corresponding to the slant range, azimuth and elevation angle most closely defining each point is extracted from the dataset and displayed on the video screen as a small rectangle. The relative size of each rectangle is a function of the spatial extent of the pulse volume. Since the width of the pulse volume is a function of spatial beamwidth, the size of each rectangular data point varies directly with the slant range at which the vertical plane is intersected by the radar beam. The contiguous display of all of these finite rectangles yields the vertical slice (Corbett, 1987).

One VSLICE constructed from the 8 March dataset was incorporated into the discussion of results, Section 5.2.1 of this thesis. Note that the same types of errors described in Section 3.3.1.1 apply to this technique. Also note that there is no data editing involved in VSLICE.

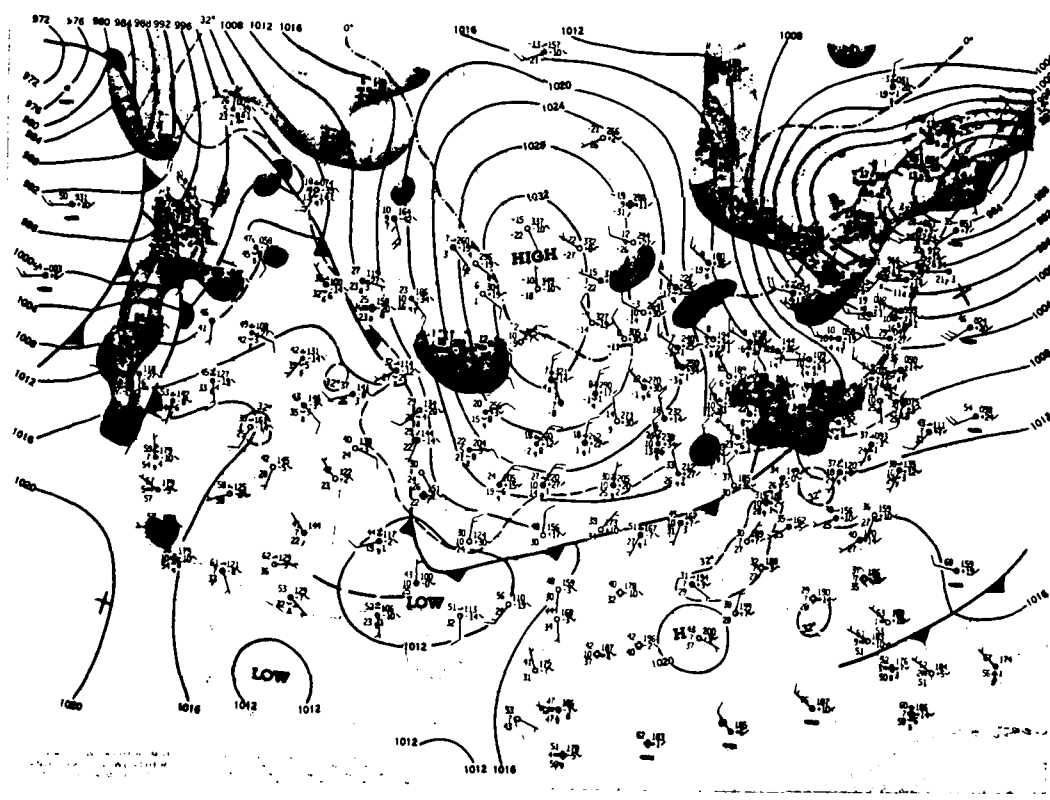
4. SYNOPTIC AND MESOSCALE OVERVIEW

4.1 Synoptic Setting

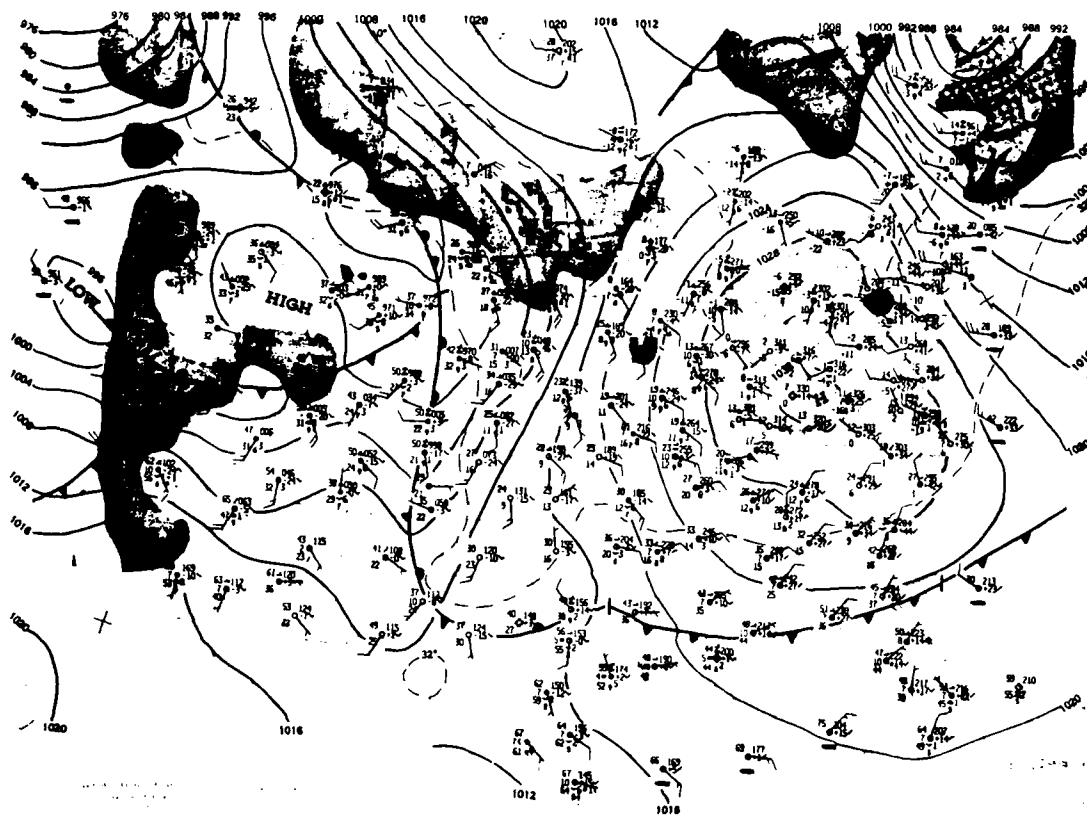
At 1200 GMT on 7 March 1986, the primary synoptic scale feature of interest for the GALE study area was a polar cold front originating from an intense dual-centered low pressure system over extreme southeastern Canada. The front extended southwestward along the northeastern United States coast, passing through the District of Columbia, northwestern Virginia and the central portions of Kentucky and Tennessee. Ahead of the front was a weak southwesterly flow across the Carolinas, mostly cloudy skies and temperature/dewpoint readings in the upper 30's and mid 20's, respectively. Behind the front, through Kentucky and Tennessee, winds were northwesterly at 10 to 15 knots with temperatures and dewpoints in the 20's and teens, respectively. Limited mixed precipitation was present along the Appalachians. Figure 4.1a depicts the synoptic setting just described.

The polar front raced southeastward such that within 24 hours the post-frontal high pressure feature, centered over the North Dakota/Minnesota border the previous morning, was situated over the border of Ohio and West Virginia. Clear skies, a northerly flow at 10 knots and temperature/dewpoint readings in the 20's and single digits, respectively, typified the North Carolina coastal area (Figure 4.1b).

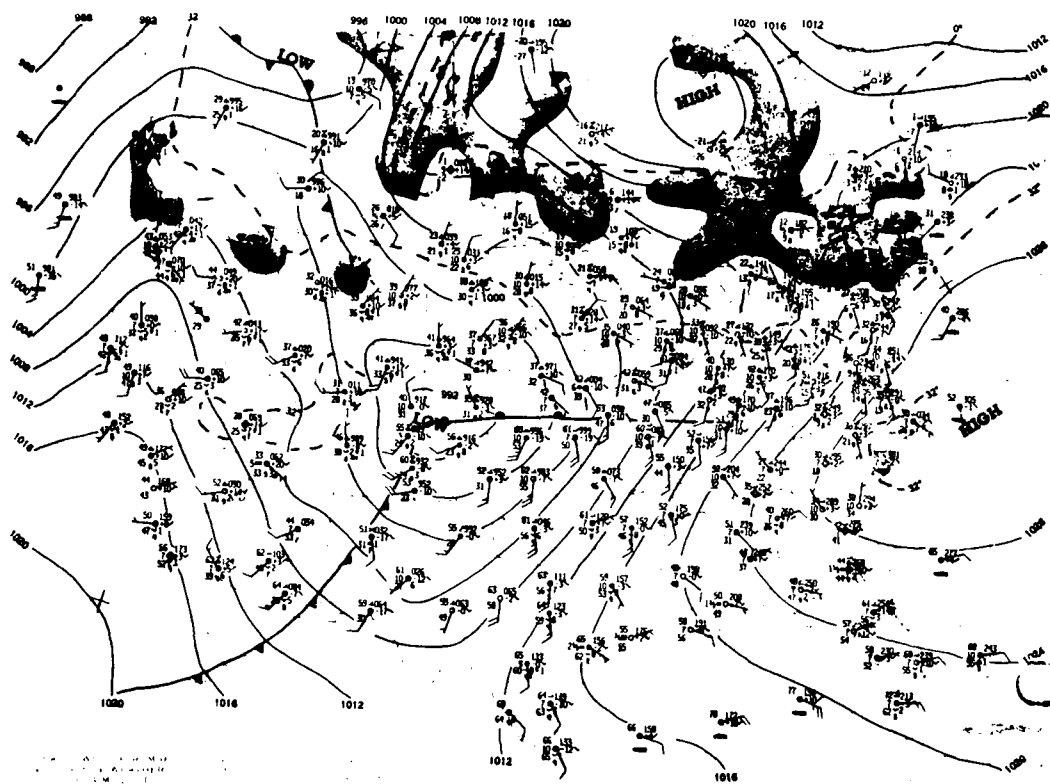
By 1200 GMT on 9 March 1986, the synoptic high had migrated southeastward and was centered approximately 250 kilometers east-southeast of Cape Hatteras (Figure 4.1c). The winds across eastern North



4.1a Synoptic map of the United States on 7 March 1986 at 1200 GMT.



4.1b Synoptic map of the United States on 8 March 1986 at 1200 GMT.



4.1c Synoptic map of the United States on 9 March 1986 at 1200 GMT.

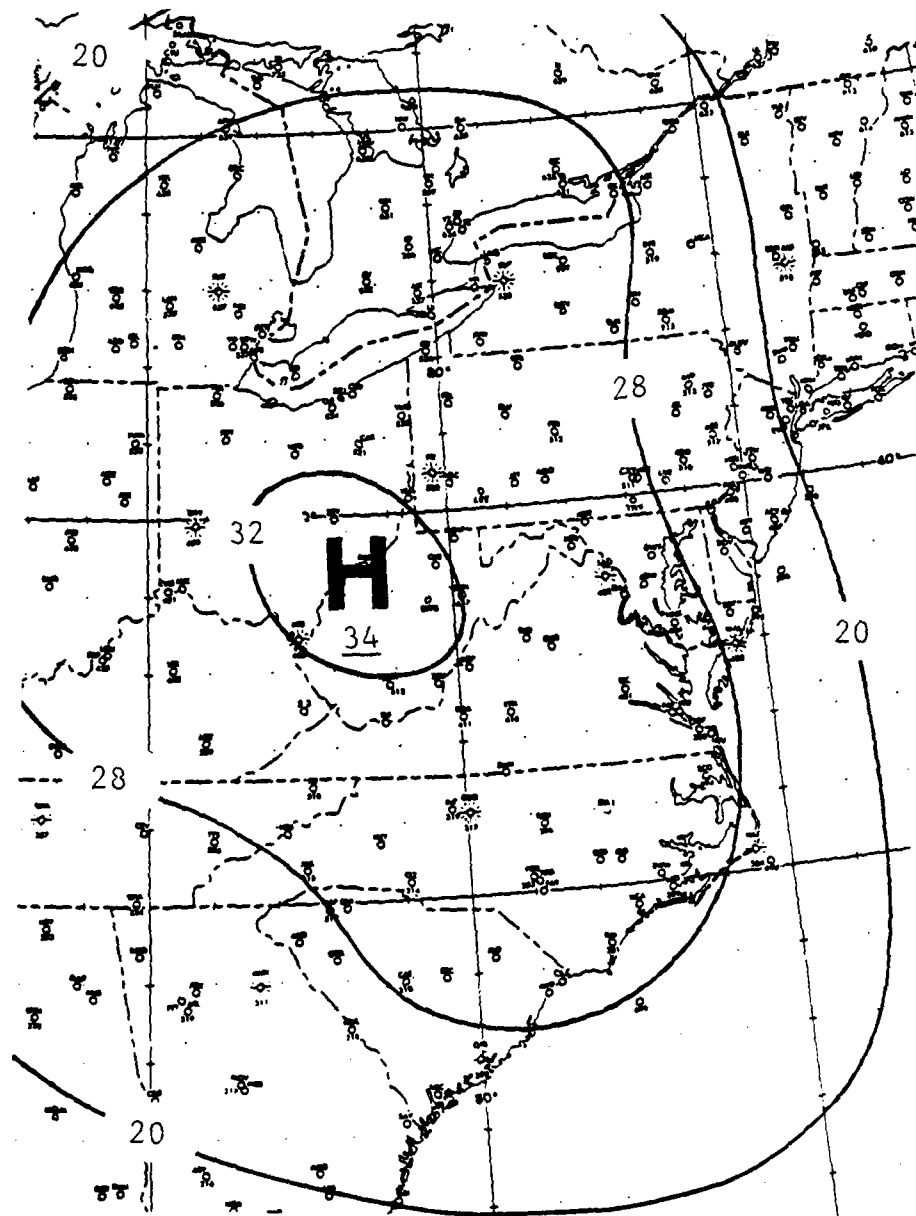
Carolina were light southeasterly with fair to partly cloudy skies, temperatures near freezing and dewpoints still in the single digits.

Figures 4.1a, 4.1b and 4.1c were taken from Daily Weather Maps, Weekly Series March 3-9, 1986, Department of Commerce, United States of America.

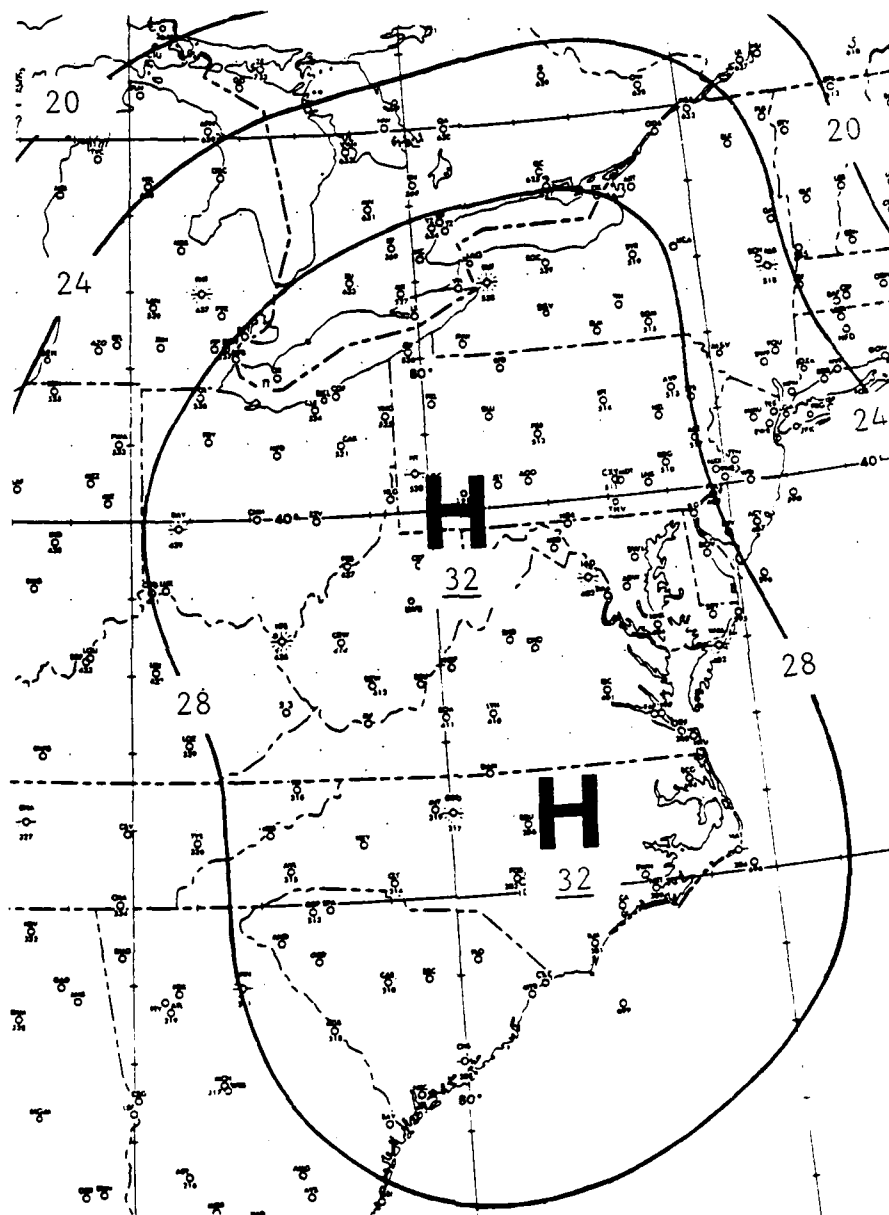
4.2 Meso- α Setting

Figures 4.2a, 4.2b and 4.2c depict the meso- α scale pressure patterns across the eastern United States at 1200 and 1800 GMT on 8 March 1986 and 0000 GMT on 9 March 1986, respectively. These figures are presented to give a somewhat better spatial and temporal resolution of the position of the synoptic high which dominated the mid-Atlantic states during the data collection period of this study. Noteworthy from the figures is the rapid transition of the horizontal pressure pattern in the vicinity of the Outer Banks, North Carolina. The moderate northerly winds present at the beginning of the experiment became light and northeasterly during the several hours of data collection. By the end of the study period, 2200 GMT, the center of the synoptic high was located along the western edge of Pamlico Sound resulting in a very weak horizontal pressure gradient in the vicinity of the radar network.

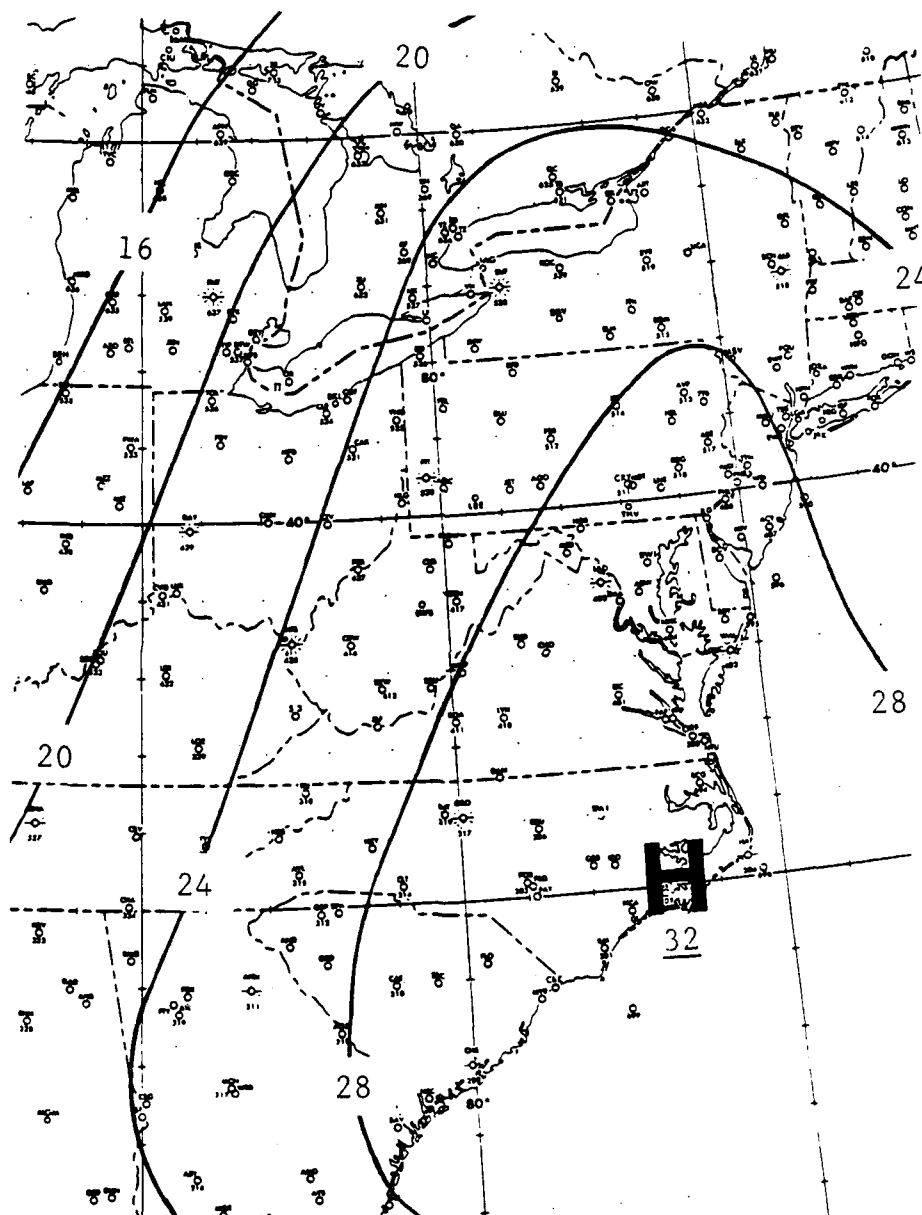
The information used to construct the figures referenced in this section was obtained from surface analyses prepared by the United States Department of Commerce NOAA/NWS/NMC.



4.2a Meso- α map of the eastern United States
on 8 March 1986 at 1200 GMT.



4.2b Meso- α map of the eastern United States
on 8 March 1986 at 1800 GMT.



4.2c Meso- α map of the eastern United States
on 9 March 1986 at 0000 GMT.

4.3 Meso- β Surface Temperature and Wind Field Analysis

4.3.1 Surface Temperature Distribution

The distribution of sea surface temperatures (SST) along the North Carolina Coastline for 7 and 9 March (8 March unavailable) are depicted by Figures 4.3a and 4.3b, respectively. The imagery was derived from NOAA polar-orbiting satellite observations, courtesy of Fred Vukovitch, Research Triangle Institute, Research Triangle Park, North Carolina. The spatial resolution is one kilometer. The SST across the area over which radar data was collected is on the order of 7 degrees Celsius. Just beyond this area, to the east, is a strong SST gradient of approximately 1 degree Celsius per kilometer over a distance of 10 to 15 kilometers. This gradient represents transition into the western edge of the Gulf Stream.

All PAM stations along coastal North Carolina reported surface temperatures within 1 degree Celsius of freezing throughout the data collection period. The combination of SST and land surface temperature (LST) yields a surface temperature distribution which will be referenced in subsequent discussion.

4.3.2 Wind Field Analysis

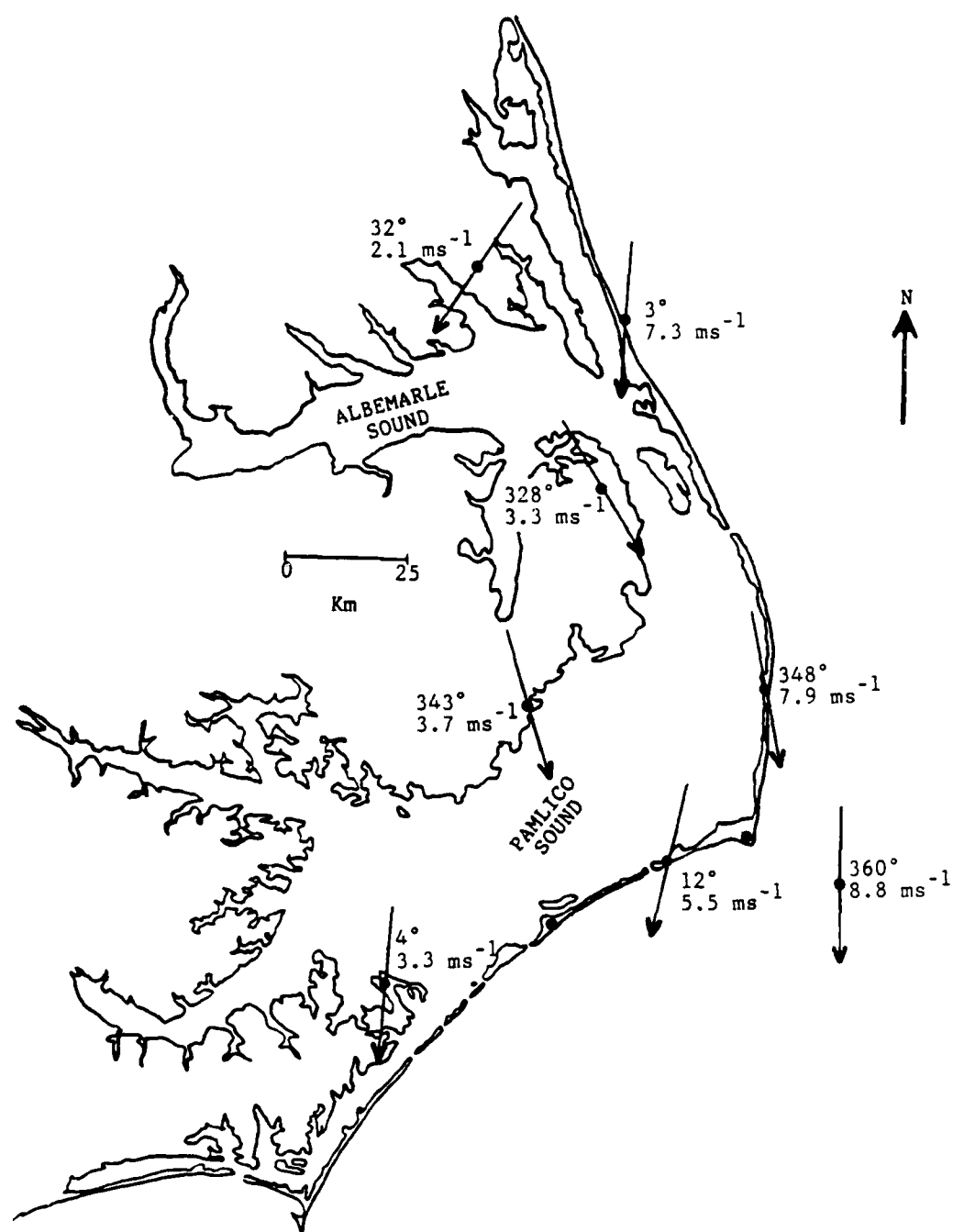
Half-hourly plots of wind speed and direction are given by Figures 4.4a through 4.4i. The data used to construct these plots were acquired from the PAM stations listed in Section 3.2, the micrometeorological tower at Duck, North Carolina, and the Diamond Shoals C-MAN platform. Wind observations from both Duck and Diamond Shoals were reported hourly and are thus missing (indicated by an "M") from the wind



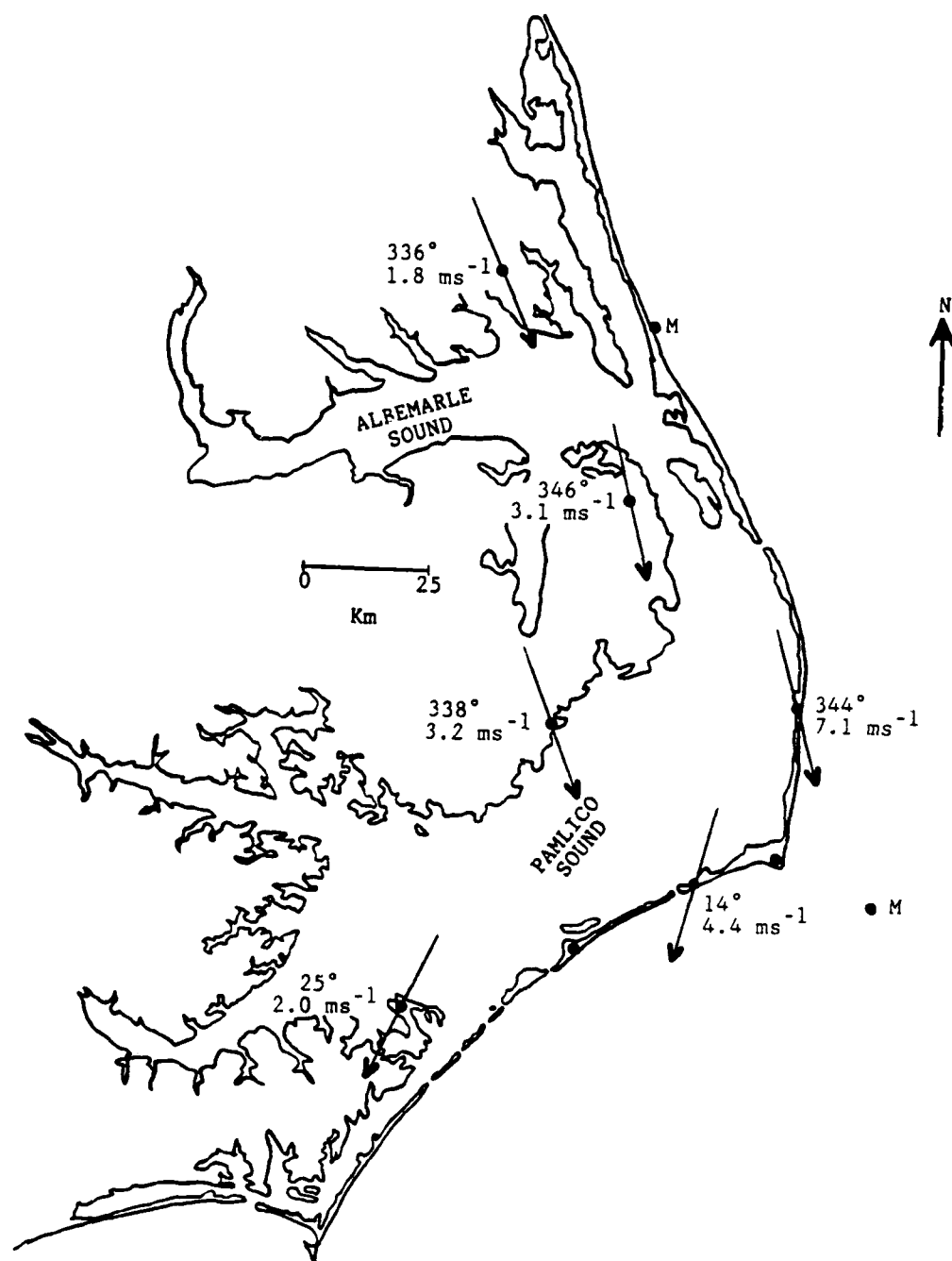
Figure 4.3a Distribution of SST across the Outer Banks coastal waters on 7 March 1986.



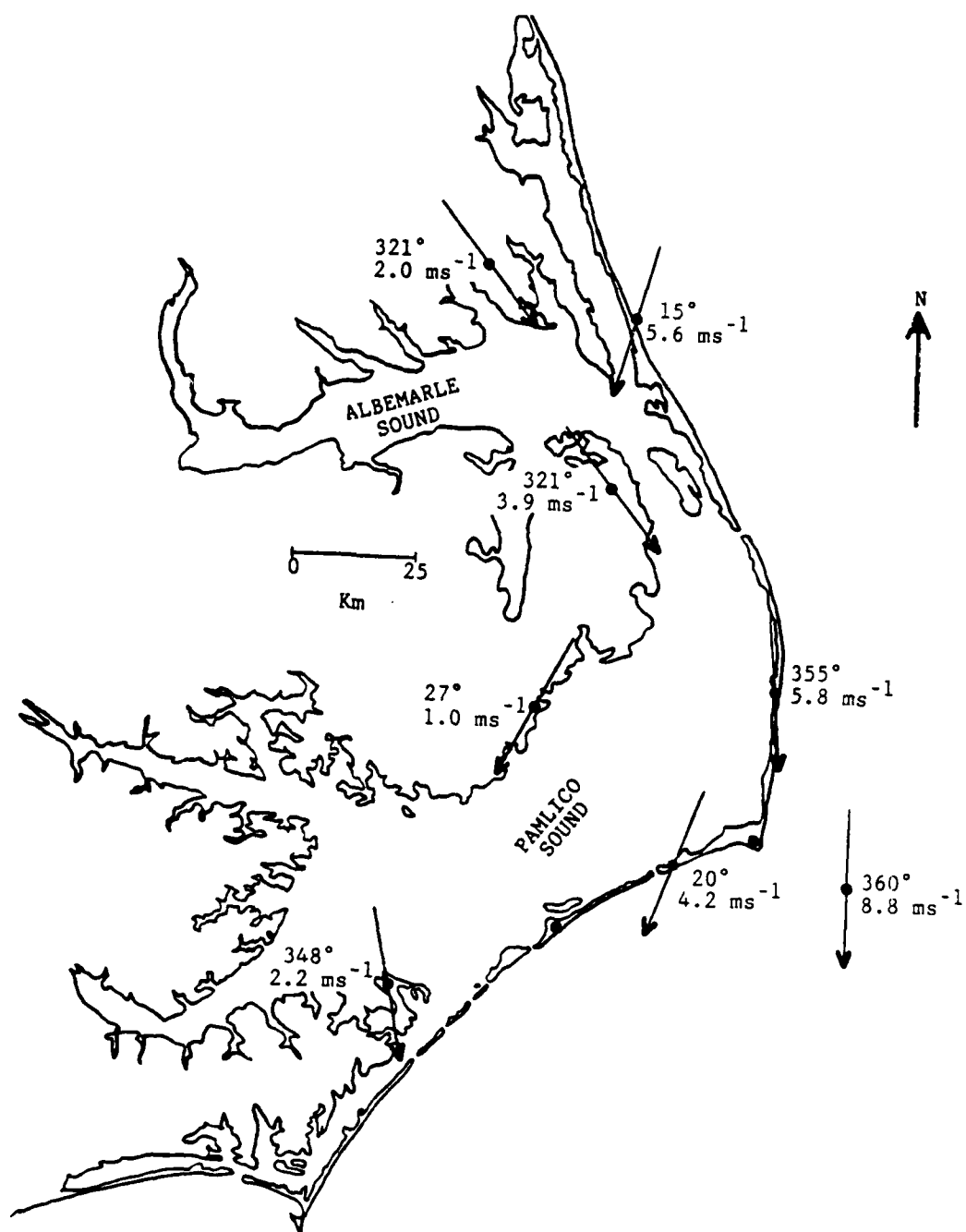
Figure 4.3b Distribution of SST across the Outer Banks coastal waters on 9 March 1986.



4.4a Plot of the meso- β wind field along the Outer Banks of North Carolina on 8 March 1986 at 1800 GMT.



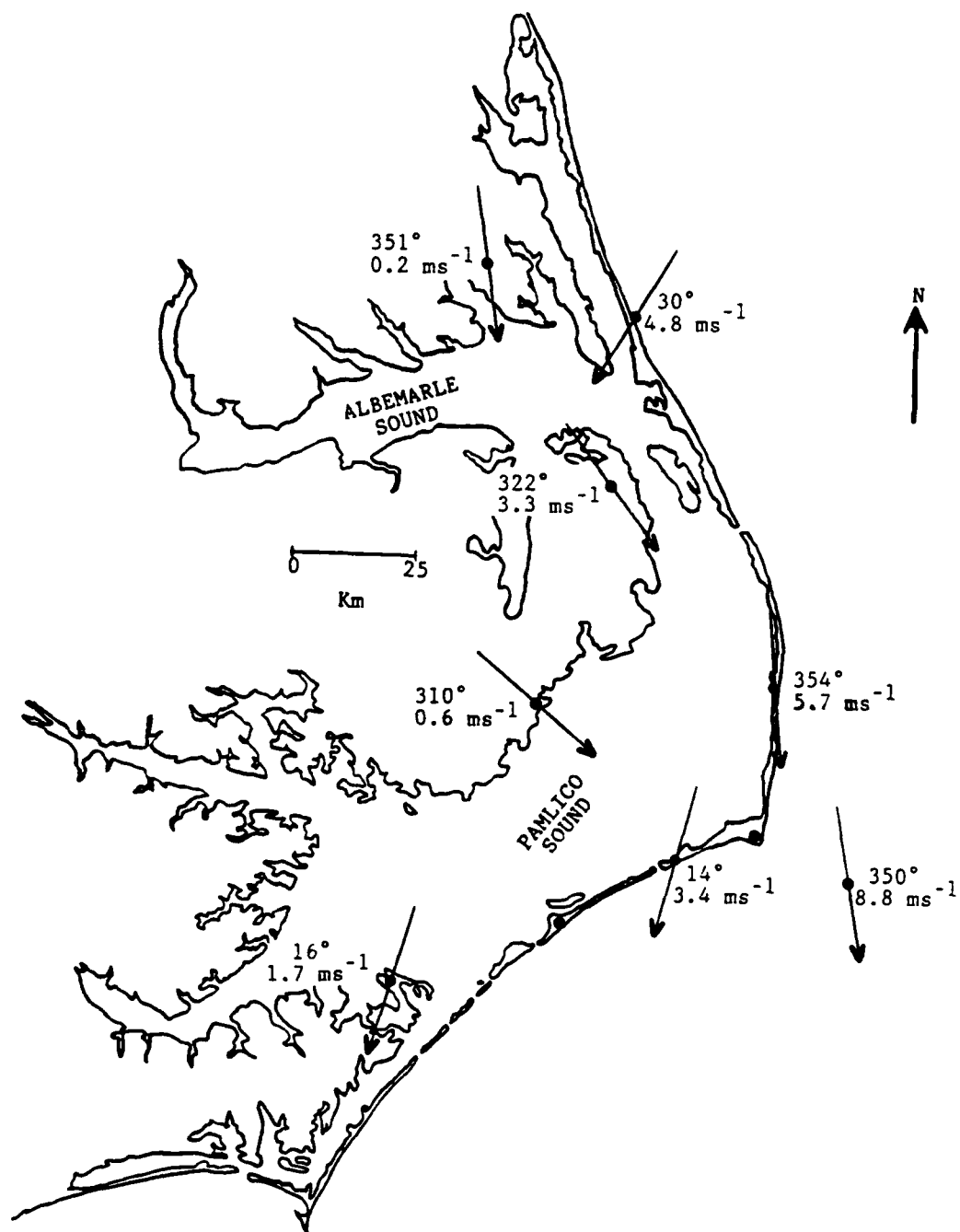
4.4b Plot of the meso-β wind field along the Outer Banks of North Carolina on 8 March 1986 at 1830 GMT.



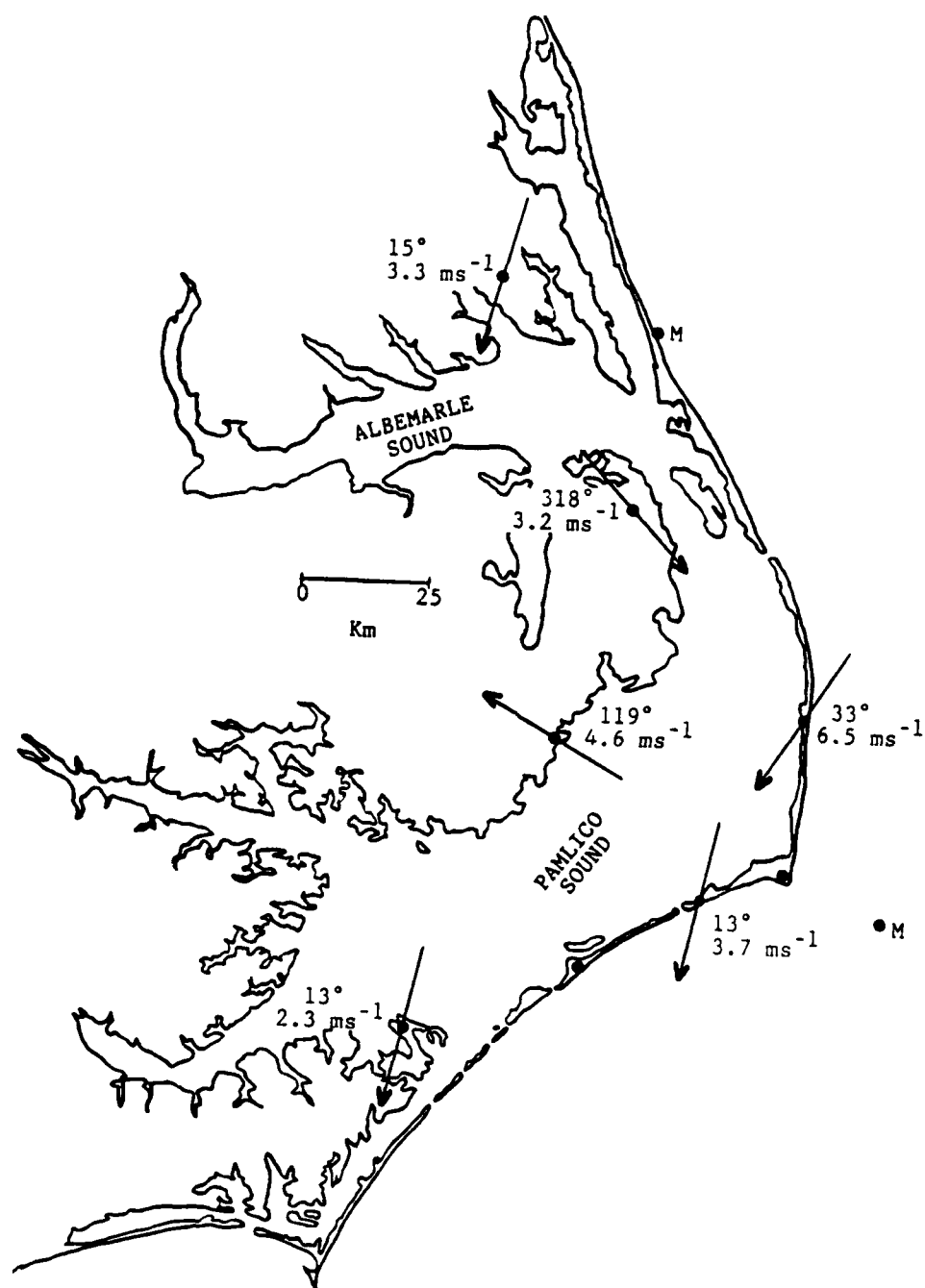
4.4c Plot of the meso-β wind field along the Outer Banks of North Carolina on 8 March 1986 at 1900 GMT.



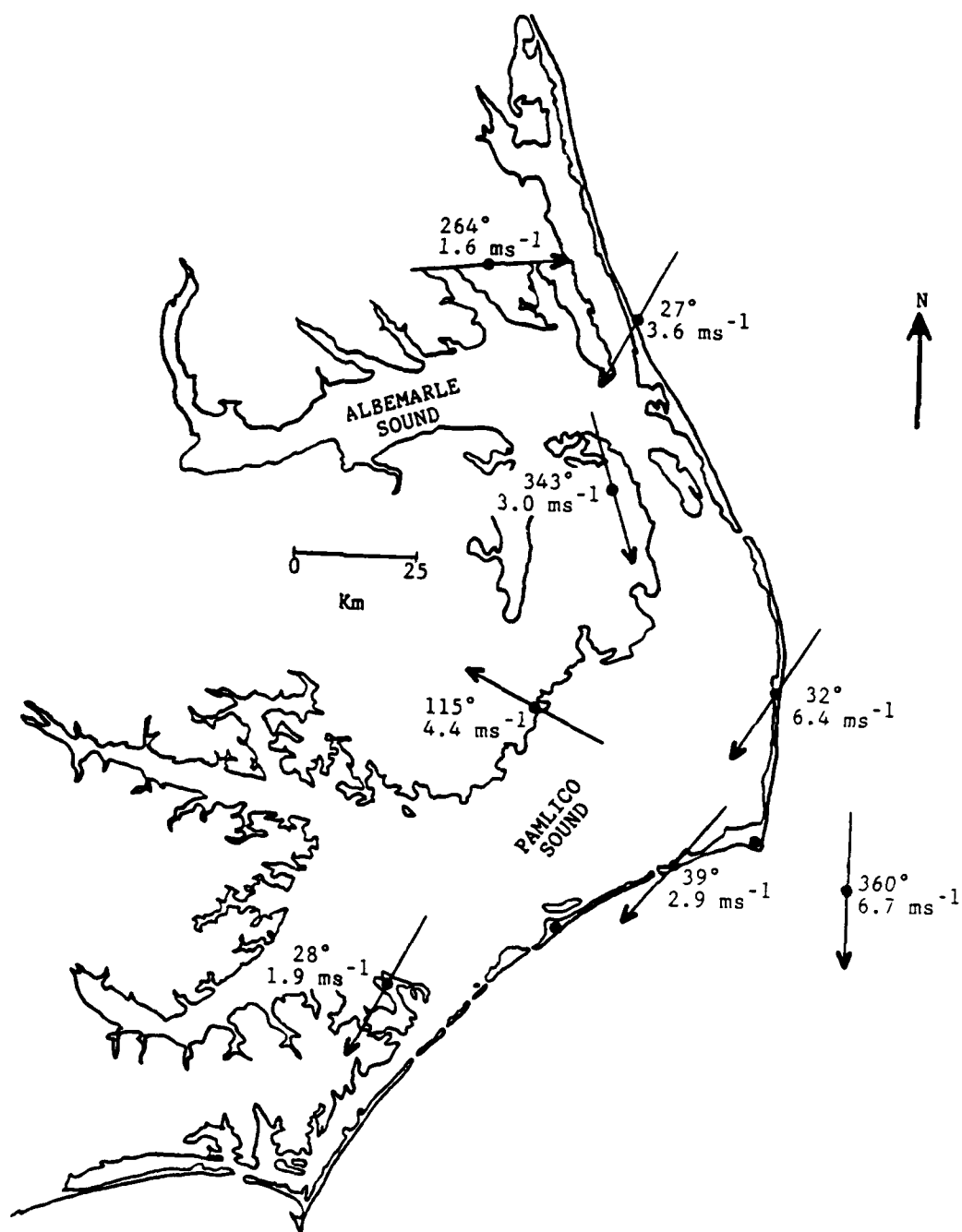
4.4d Plot of the meso-β wind field along the Outer Banks of North Carolina on 8 March 1986 at 1930 GMT.



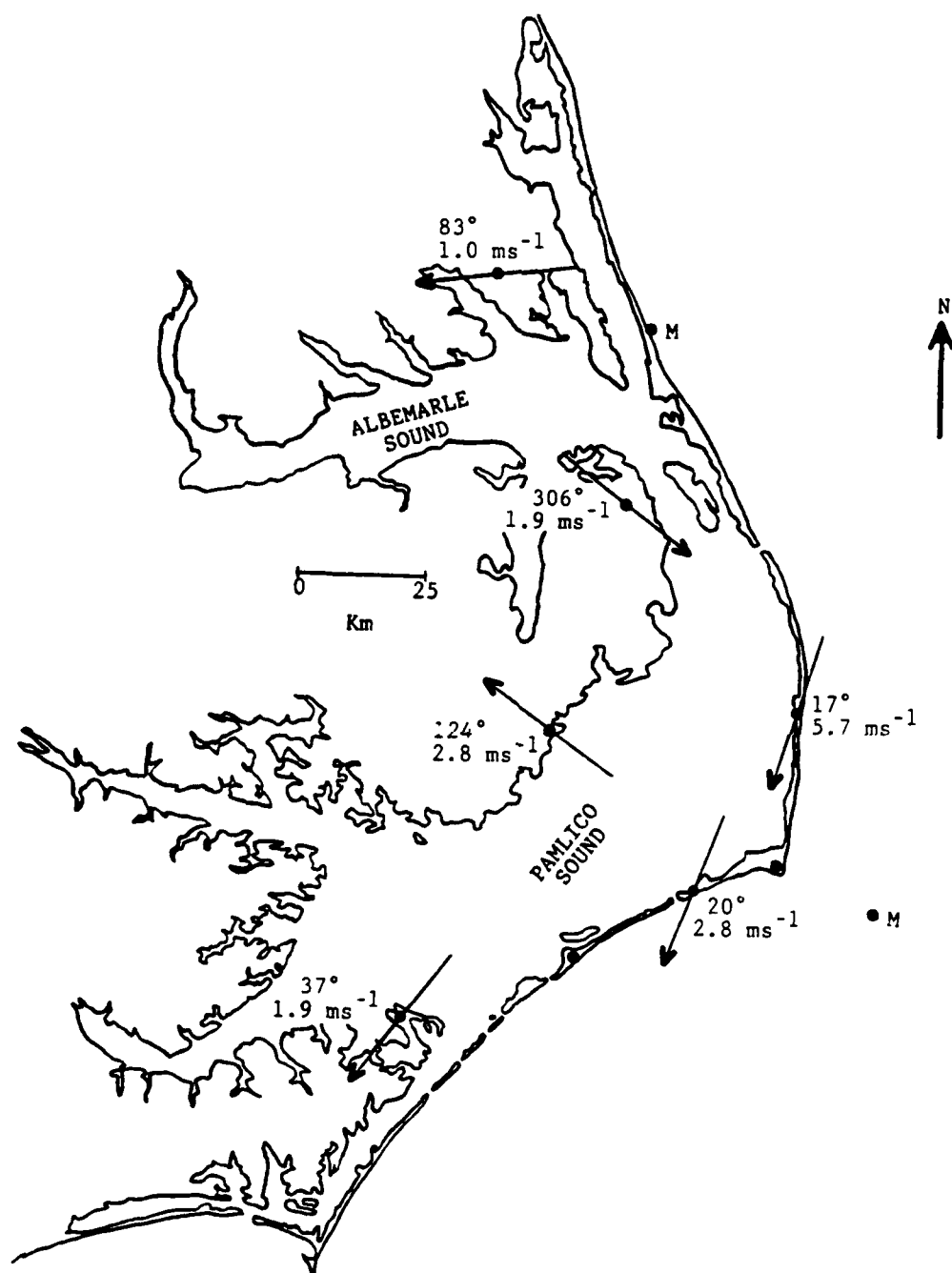
4.4e Plot of the meso- β wind field along the Outer Banks of North Carolina on 8 March 1986 at 2000 GMT.



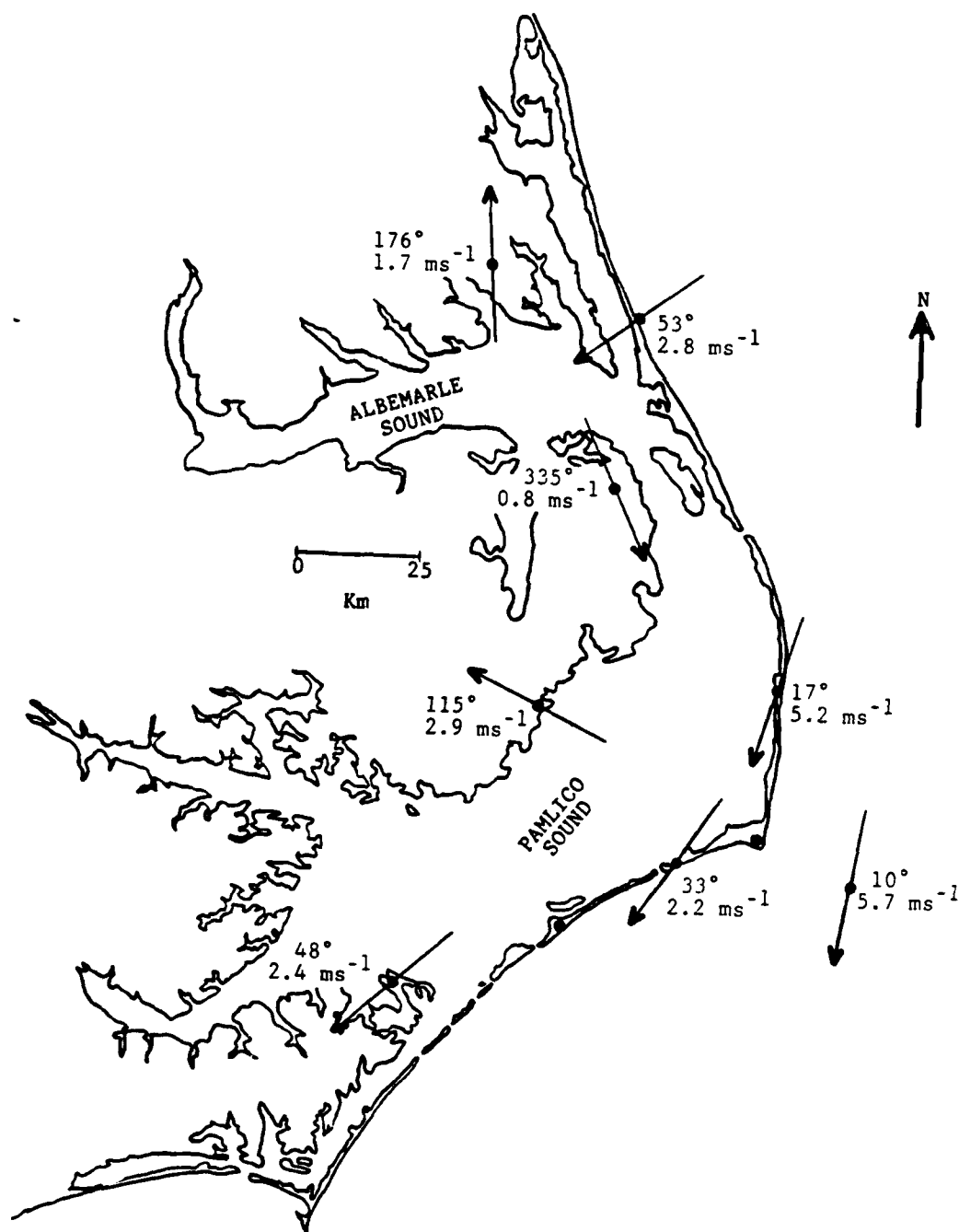
4.4f Plot of the meso-β wind field along the Outer Banks of North Carolina on 8 March 1986 at 2030 GMT.



4.4g Plot of the meso- β wind field along the Outer Banks of North Carolina on 8 March 1986 at 2100 GMT.



4.4h Plot of the meso-β wind field along the Outer Banks of North Carolina on 8 March 1986 at 2130 GMT.



4.4i Plot of the meso- β wind field along the Outer Banks of North Carolina on 8 March 1986 at 2200 GMT.

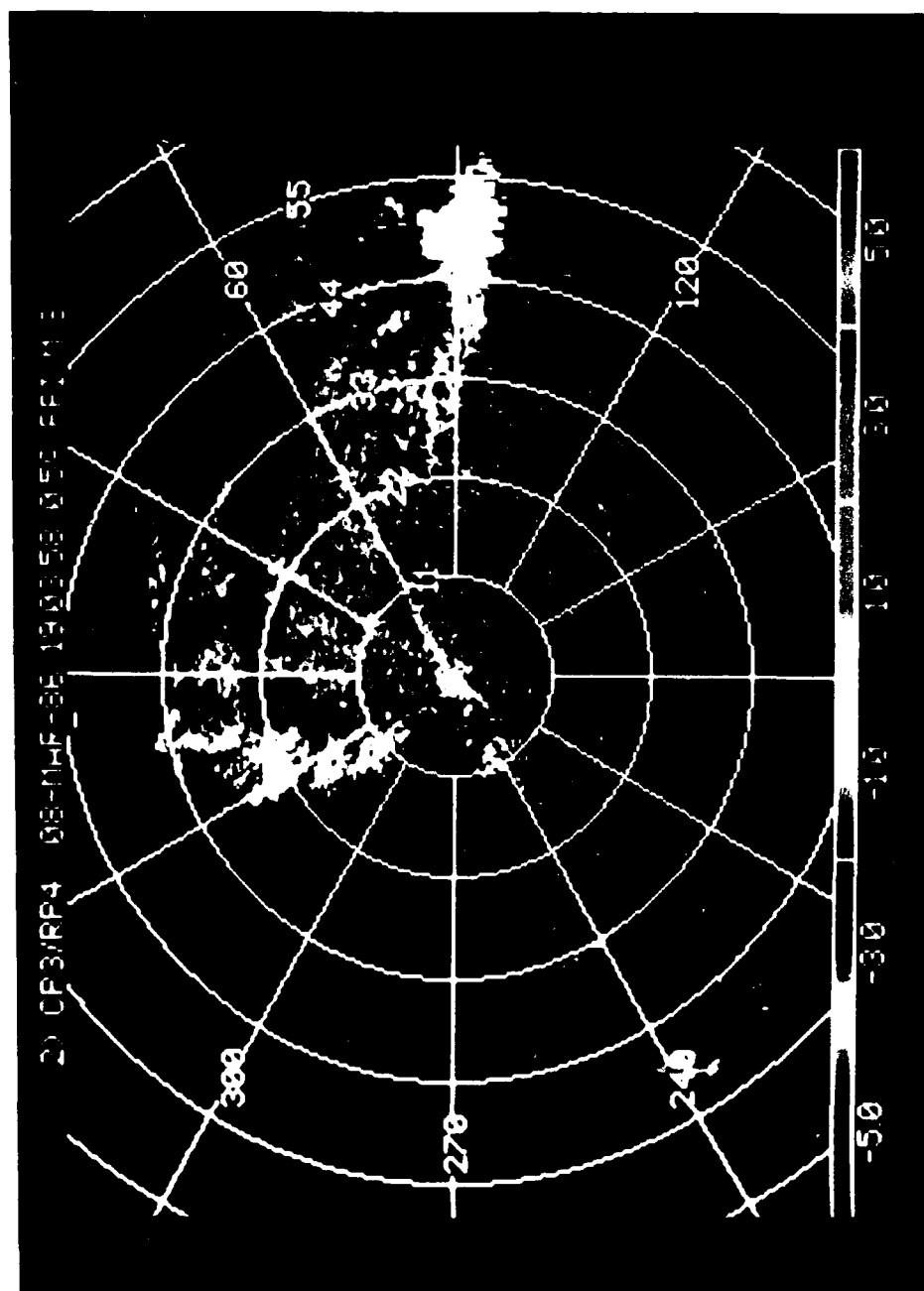
plots on the half hour. Note that these wind data were acquired at heights of 30 and 50 meters above the ocean surface for Duck and Diamond Shoals, and are thus larger in magnitude as a result of the diminished effect of surface friction. Also note that the Diamond Shoals wind direction is reported only to the nearest 10 degrees azimuth.

Several interesting trends and phenomena were evident from these data. As previously noted, the horizontal pressure gradient weakened during the study period as the synoptic high quickly approached the Outer Banks area. This resulted in a generally consistent wind speed decrease across the radar network. Also, the winds at Duck indicated a consistent, relatively strong onshore flow after 2000 GMT. Considering the fact that the SST at Duck was approximately 7 degrees Celsius warmer than the contiguous land mass, this counter-gradient flow cannot be part of a sea breeze circulation. Instead, this component of onshore flow likely resulted from a combination of anticyclonic shear, arising from the surface roughness discontinuity induced wind differential, and veering affected by the Coriolis force. Most notable, however, was the onset of the southeasterly wind at PAM station 46, 2030 GMT. This low-level counter-gradient flow extended well into the radar network with time. During the hour prior to the onset, this reporting station exhibited a weak, highly variable wind. Likewise, the northernmost reporting station, PAM 49, depicted a similar scenario in the same time frame. Unfortunately, this area was beyond the radar dataset. However, radar documentation of the counter-gradient flow over Pamlico Sound is treated in Section 5.2.

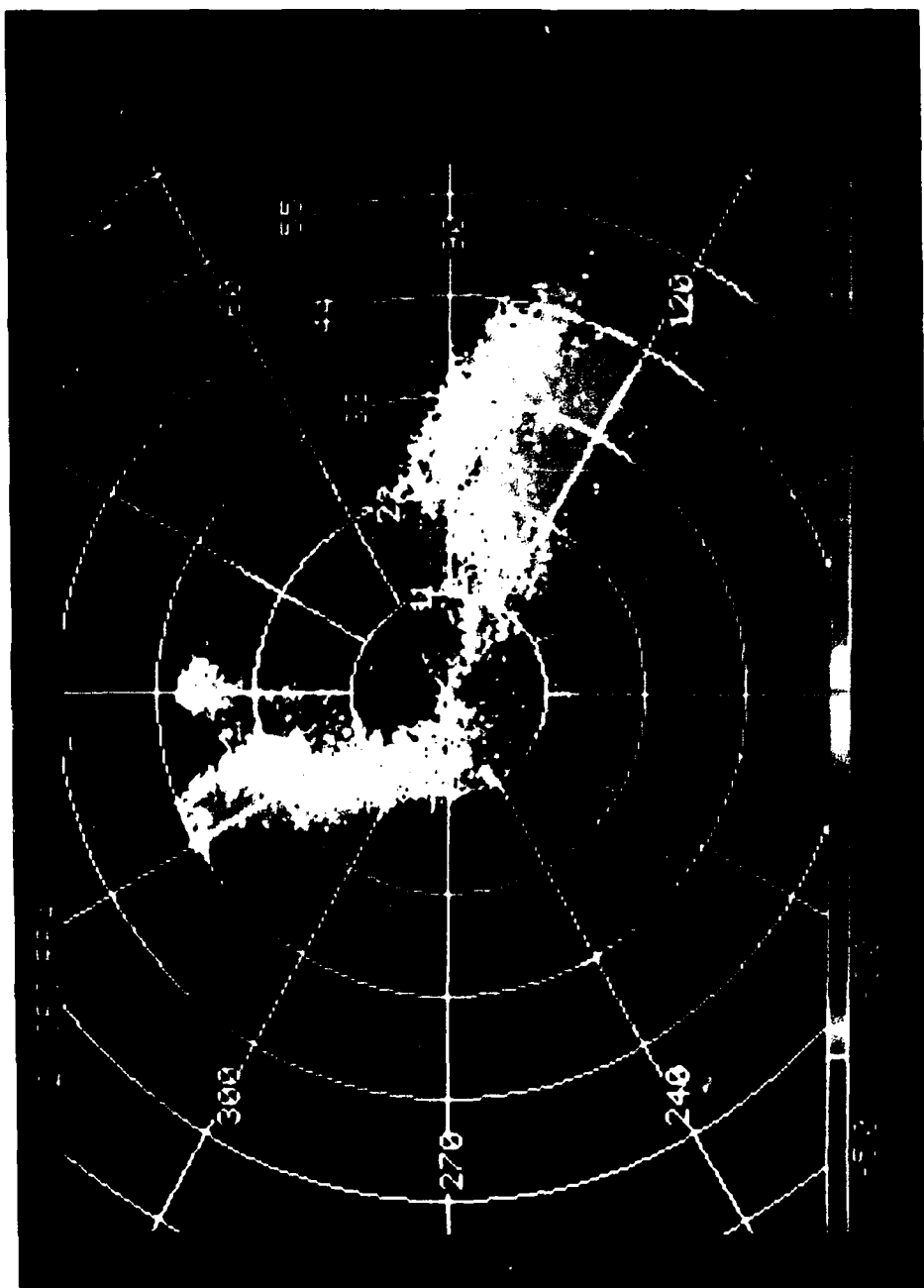
Figures 4.5a through 4.5d are reproductions of the PPI velocity display from the CP-3 radar at elevation angles of 0.3 to 0.5 degrees, hourly between 1900 and 2200 GMT. They well depict the advection of chaff and provide further insight into the meso- β wind flow across the radar network during the study period. Two particularly interesting features were evident, the discussion of each follows.

That portion of the echo originally occupying the northeast quadrant of the display exhibited considerable south-southwestward movement while the chaff to the north-northwest showed very little movement. This differential advection is probably due to upwind surface roughness differences. Simply, because the mean boundary layer wind essentially paralleled the upwind coastline, the windspeed over the western portion of Pamlico Sound was decreased by the substantially greater roughness of the underlying upwind terrestrial surface. This effect was diminished with greater distance from shoreline, resulting in an approximately linear oceanward increase in advection of the chaff area.

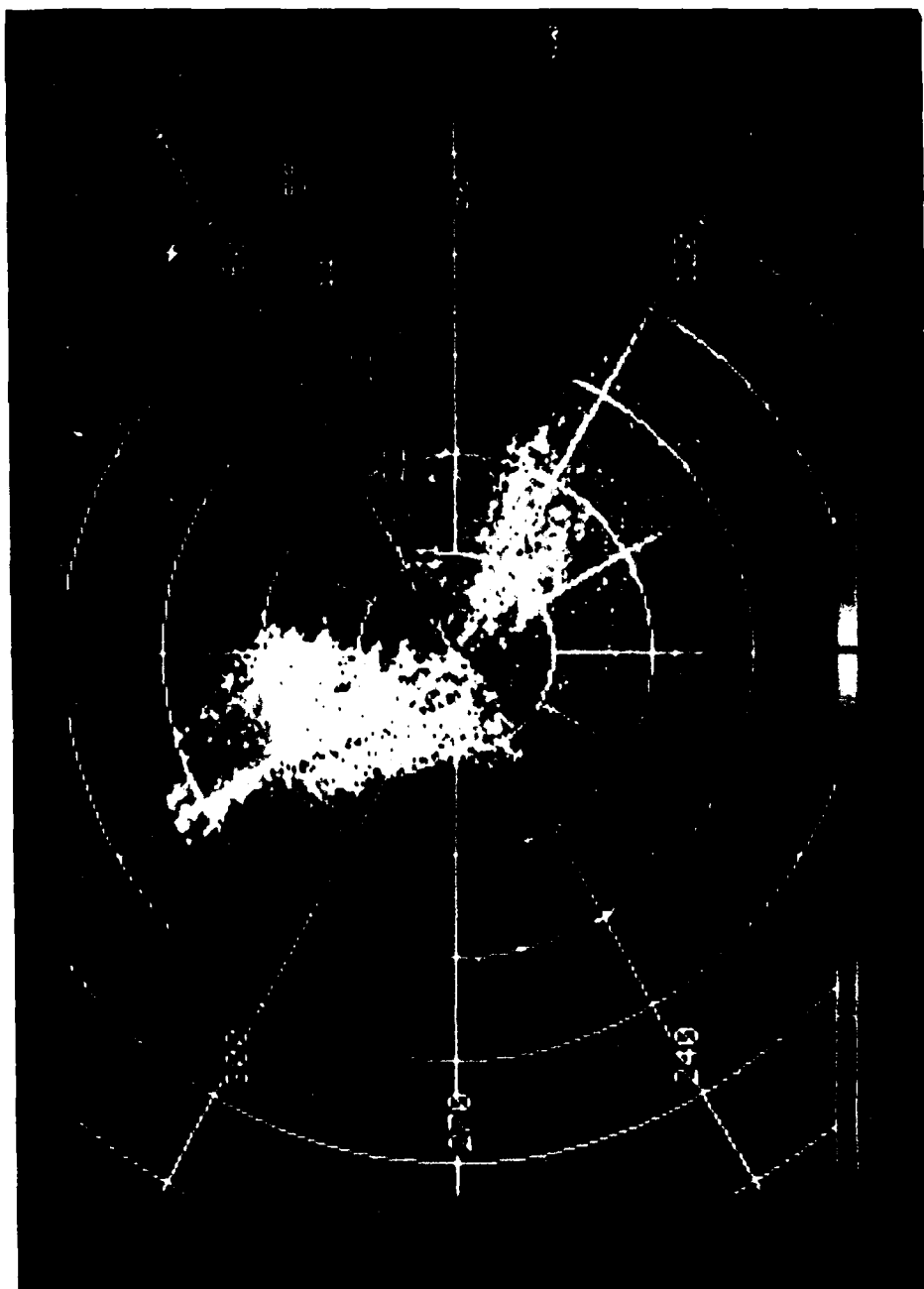
Also of interest was the narrowing and elongation of the chaff echo, particularly evident over Pamlico Sound. By convention, the color white in the PPI velocity display depicts a radial velocity of 0 meters per second, and typically, in a linearly varying horizontal wind field, lies between negative and positive (approaching and receding) radial velocities. Therefore, a "white line" can be interpreted as a line orthogonal to the wind direction in its vicinity. With this in mind, scrutiny of Figures 4.5a through 4.5c reveals a predominately east-southeast wind over Pamlico Sound while the winds over the shelf-waters are congruent with the north-northeast gradient flow, consistent



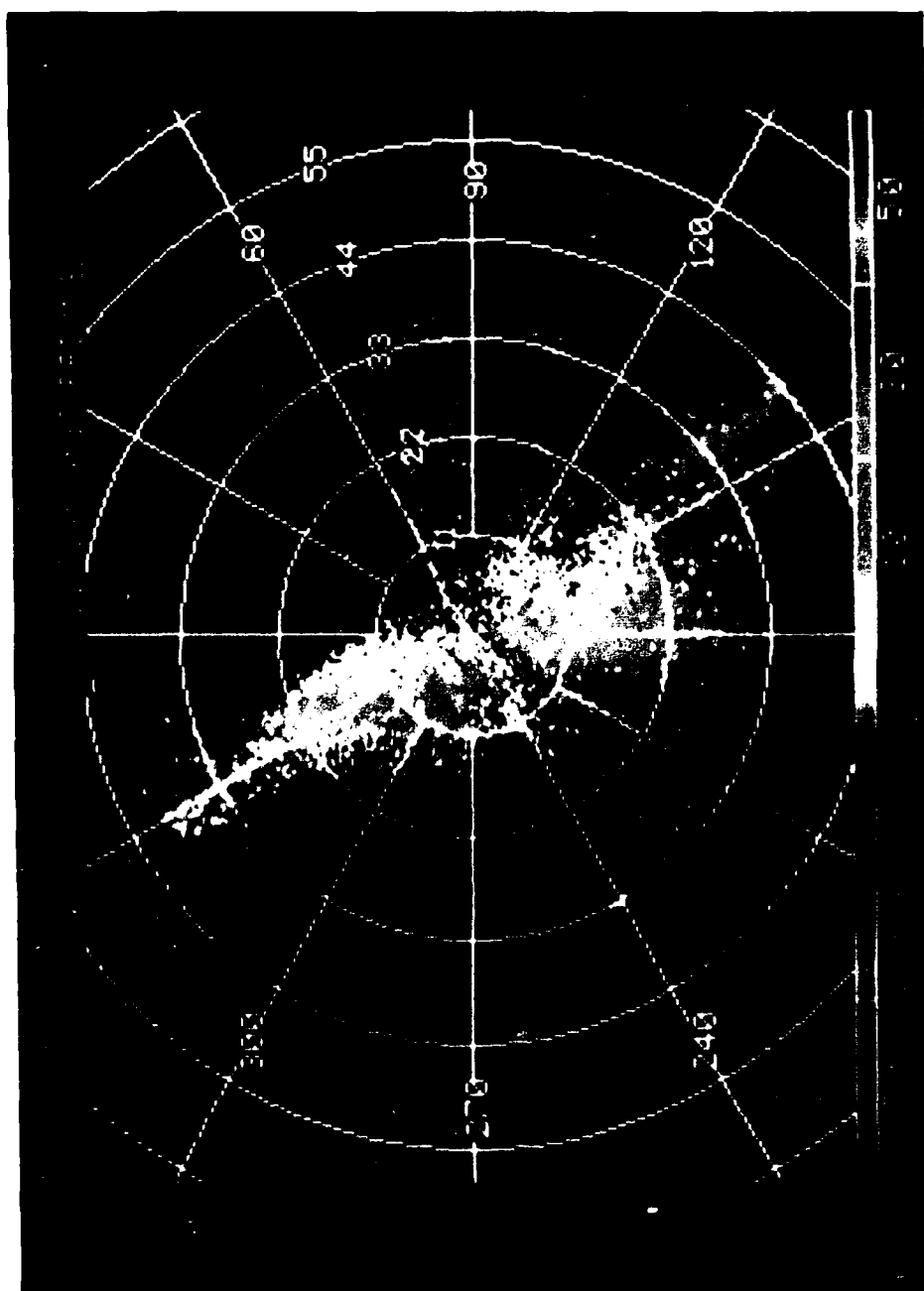
4.5a Distribution of chaff at 1903 GMT, 8 March 1986, as depicted by the CP-3 0.5 degree PPI display of radial velocity.



4.5b Distribution of chaff at 2009 GMT, 8 March 1986, as depicted by the CP-3 0.5 degree PPI display of radial velocity.



4.5c Distribution of chaff at 2103 GMT, 8 March 1986, as depicted by the CP-3 0.3 degree PPI display of radial velocity.



4.5d Distribution of chaff at 2202 GMT, 8 March 1986, as depicted by the CP-3 0.3 degree PPI display of radial velocity.

with the reported winds from several fixed stations already discussed. It is thus evident that a considerable degree of divergence and stretching deformation was present across the outer banks area during the study period.

The onshore component of this phenomenon is likely attributable to the anticyclonic shear/coriolis force rationale discussed in the preceding paragraph. The oceanward elongation likely resulted from the underlying SST differences depicted by Figures 4.3a and 4.3b. Pamlico Sound and the coastal shelfwaters were at approximately 6 degrees Celsius. The Mid-shelf Front, a SST discontinuity found between the shelfwaters and the western edge of the Gulf Stream, was located 15 to 20 kilometers west of the Outer Banks. The horizontal thermal gradient associated with this transition zone was on the order of 2 degrees Celsius per kilometer such that the SST west of the "Front" were 19 to 20 degrees Celsius. The Gulf Stream was on the order of 30 kilometers beyond the Mid-shelf Front and had a SST of 23 to 24 degrees Celsius. Given the strong differential heating of the air passing over the waters just described, and the tendency for air of greater density to diverge towards air of lesser density, it is reasonable to expect that the oceanward narrowing and elongation of the chaff field resulted from these circumstances.

5. DISCUSSION OF RESULTS

5.1 Temporal Variations of MABL Structure

This section of the result thesis focuses on the evident stability transition which occurred during the 8 March case study. Lapse rates derived from in situ rawinsonde launches are presented as verification, followed by discussion of VAD-derived time-height plots of selected kinematic properties.

5.1.1 Rawinsonde Derived Lapse Rates

The National Weather Service (NWS) at Buxton, North Carolina (Cape Hatteras), launched rawinsondes at 3 hour intervals on 8 March 1986. Atmospheric temperature lapse rates (γ) were calculated through the depth of the boundary layer from rawinsonde data at 1800 and 2100 GMT, 8 March, and 0000 GMT, 9 March, and are listed in Table 5.1.

Table 5.1 Boundary Layer Lapse Rates Derived From
NWS Rawinsonde Data, Cape Hatteras,
North Carolina, 8 March 1986.

Time (GMT)	β (deg C/km)
1800	-12.80
2100	- 8.52
0000	- 6.67

Comparing the calculated lapse rates with the dry adiabatic lapse rate, γ_d , the relative thermal stability can be inferred. Given the defined γ_d value of -9.8 degrees Celsius per kilometer, it is readily apparent that just prior to 2100 GMT the boundary layer transitioned from

unstable to neutral conditions, progressively continuing to a stable lapse rate. Considering a SST several degrees warmer than the land surface over which the rawinsonde data were acquired, the overwater transition likely occurred a bit later than the calculated lapse rates would indicate. Nevertheless, the trend of increasing stability with time is evident.

5.1.2 VAD-Derived Time-height Plots of Kinematic Properties

The VAD Doppler radar analysis technique, detailed in Section 3.3.1, was applied to the 8 March dataset to achieve spatially and temporally averaged values of kinematic properties at half-hourly intervals, 1830 to 2200 GMT. Data for the 1830 volume was taken with the CP-4 radar at Cape Hatteras. All subsequent volumes were taken by the CP-3 radar at Ocracoke. Note that a VAD volume was not possible by either radar at 1900 as the area of chaff was between the radars at this time. The radius of analysis was varied between 5 and 15 kilometers in 5 kilometer increments. Figure 5.1 is a schematic of the analysis radii around the CP-3 and CP-4 radars. Table 5.2 lists the details of the VAD volumes processed for this study. Recall that a scan refers to one complete azimuthal revolution and that an azimuth rotation rate of 15 degrees per second equates to an elapsed time of 24 seconds per scan.

Before interpreting the time-height plots of horizontal wind speed, divergence, stretching deformation and vertical velocity, it is important to briefly detail the method by which they were synthesized. Table 5.3 lists the locations of data points within the plots, by

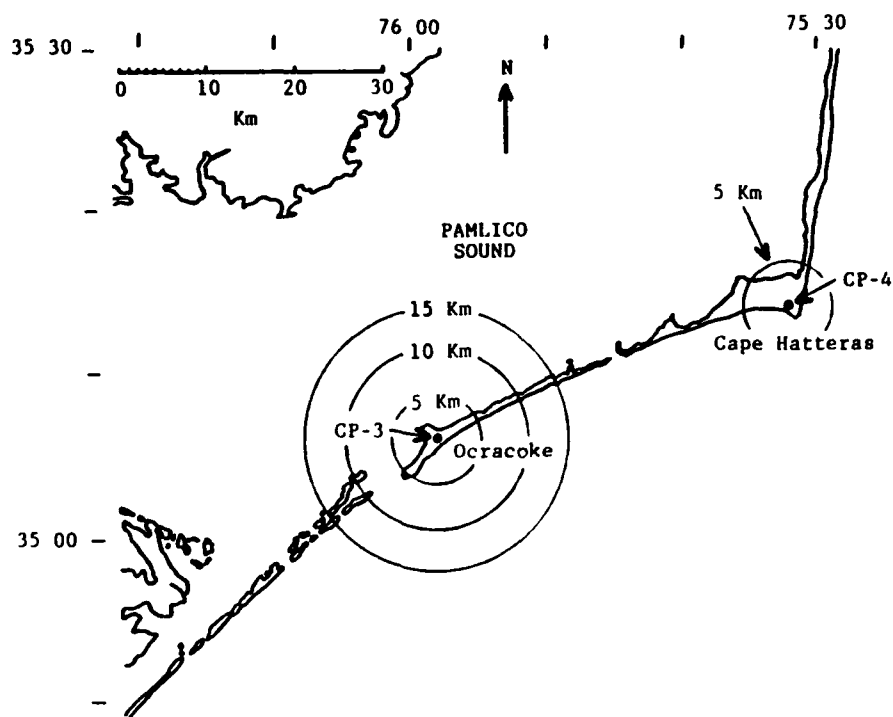


Figure 5.1 VAD analysis radii around the CP-3 and CP-4 radars for the 8 March 1986 MABL radar study.

Table 5.2 Descriptive Listing of the VAD Volumes Processed
for the 8 March 1986 MABL Study

Radar	Volume Start	# of Scans	Volume Duration	Elevation Increments	Maximum Elevation	VAD Radii
CP-4	1831:46	14	5:36	0.5 ⁰	6.5 ⁰	5
CP-3	1934:38	14	5:36	0.5 ⁰	6.5 ⁰	5
CP-3	2003:37	14	5:36	0.5 ⁰	6.5 ⁰	5,10
CP-3	2034:34	15	6:00	0.2 ⁰	4.2 ⁰	5,10,15
CP-3	2103:25	15	6:00	0.2 ⁰	4.2 ⁰	5,10,15
CP-3	2131:04	15	6:00	0.2 ⁰	4.2 ⁰	5,10,15
CP-3	2201:43	15	6:00	0.2 ⁰	4.2 ⁰	5,10

Table 5.3 Altitude Locations, in 50 Meter Increments,
of Data Points Within the 8 March
Time-height Plots, by Analysis Radius.

Time (GMT)	Analysis Radii		
	5 km	10 km	15 km
1831	50-400 m		
1934	50-550 m		
2003	50-550 m	50-800 m	
2034	50-400 m	50-750 m	50-700 m
2103	50-400 m	50-750 m	50-700 m
2131	50-400 m	50-750 m	50-650 m
2201	50-400 m	50-650 m	

analysis radius, and applies uniformly to all kinematic properties addressed in this study. For simplicity of plotting, the data points were selected in altitude increments of 50 meters. Given a constant elevation angle and horizontal range, the information obtained from a particular scan pertains to a specific height above the horizon and does not typically equate to precise 50 meter increments. Hence, to achieve the desired increment, some approximation was necessary. Specifically, the calculated kinematic property values associated with the actual height most closely corresponding to the desired altitude were used. The average deviation of actual versus desired height was just over 5 meters, an order of magnitude less than the altitude increment itself.

Figures 5.2a through 5.2d are the time-height plots of horizontal wind speed, vertical velocity, horizontal divergence, and horizontal deformation, respectively, for the 5 kilometer analysis radius. Figures 5.3a through 5.3d and 5.4a through 5.4d follow the same sequence, but for the 10 and 15 kilometer radii, respectively. Each analysis series will be examined independently, in the order of increasing radius, with comparison discussion interspersed at appropriate points.

At the onset of the study period, all kinematic properties had values indicative of a fully turbulent boundary layer environment. The horizontal wind speed was relatively strong, as were the upward vertical velocity, low-level convergence and deformation. Between 1830 and 1930 GMT, the boundary layer turbulence characteristics changed significantly. The horizontal wind speed and deformation decreased by roughly half their former values, and the strong upward vertical

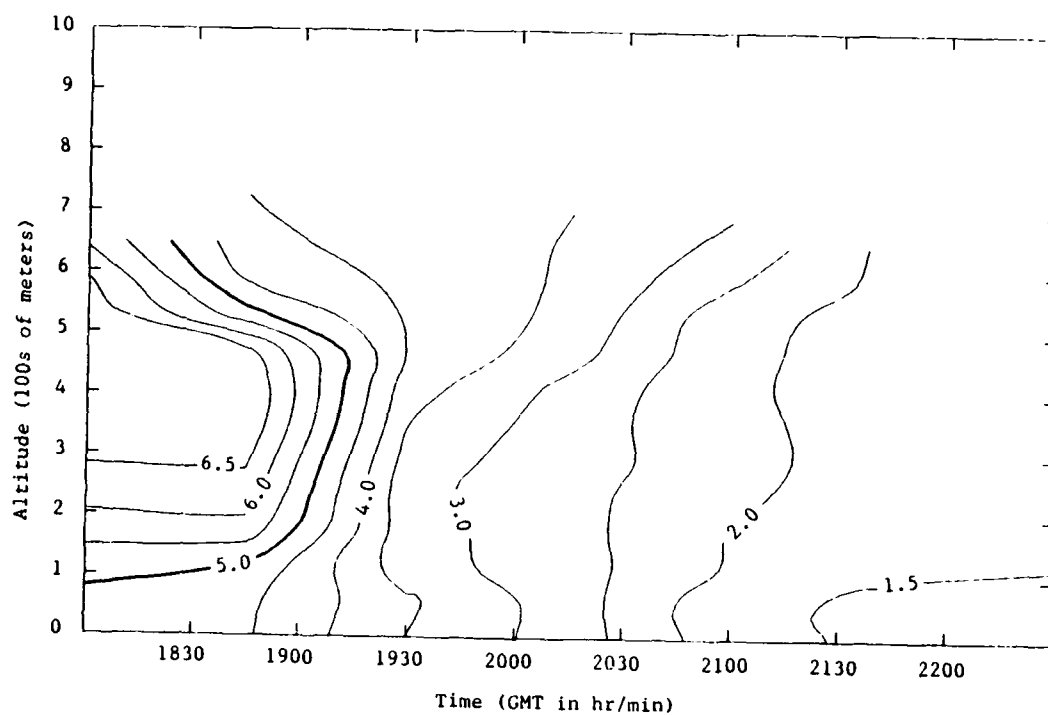


Figure 5.2a Time-height plot of horizontal wind speed (ms^{-1}) during the 8 March 1986 MABL radar study for the VAD analysis radius of 5 kilometers.

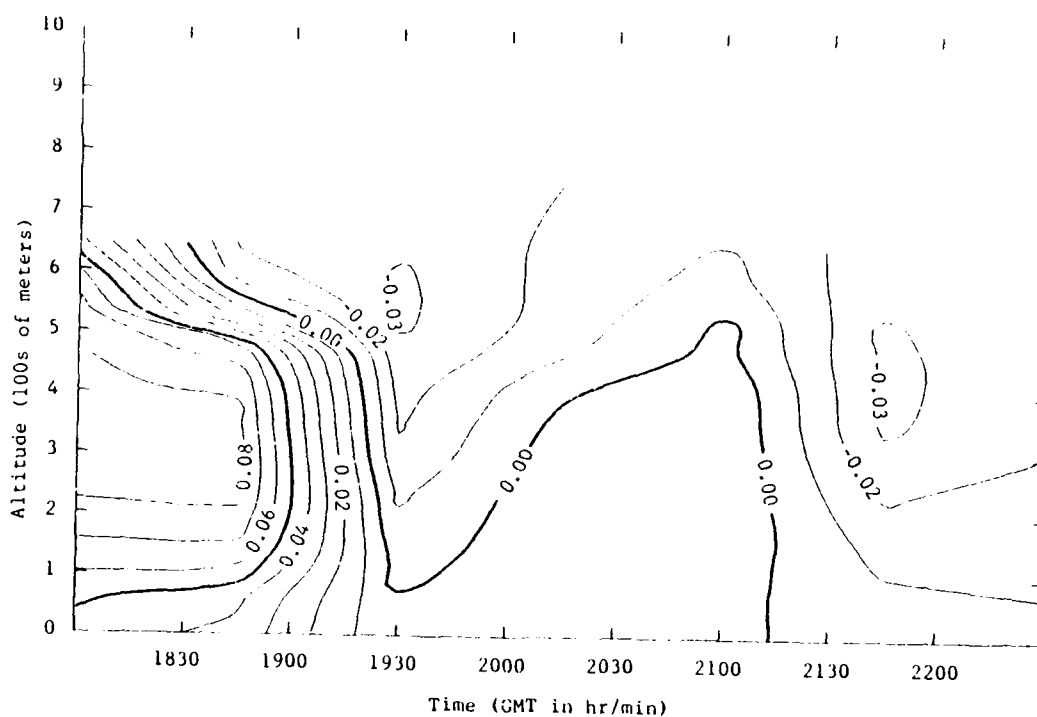


Figure 5.2b Time-height plot of vertical velocity (ms^{-1}) during the 8 March 1986 MABL radar study for the VAD analysis radius of 5 kilometers.

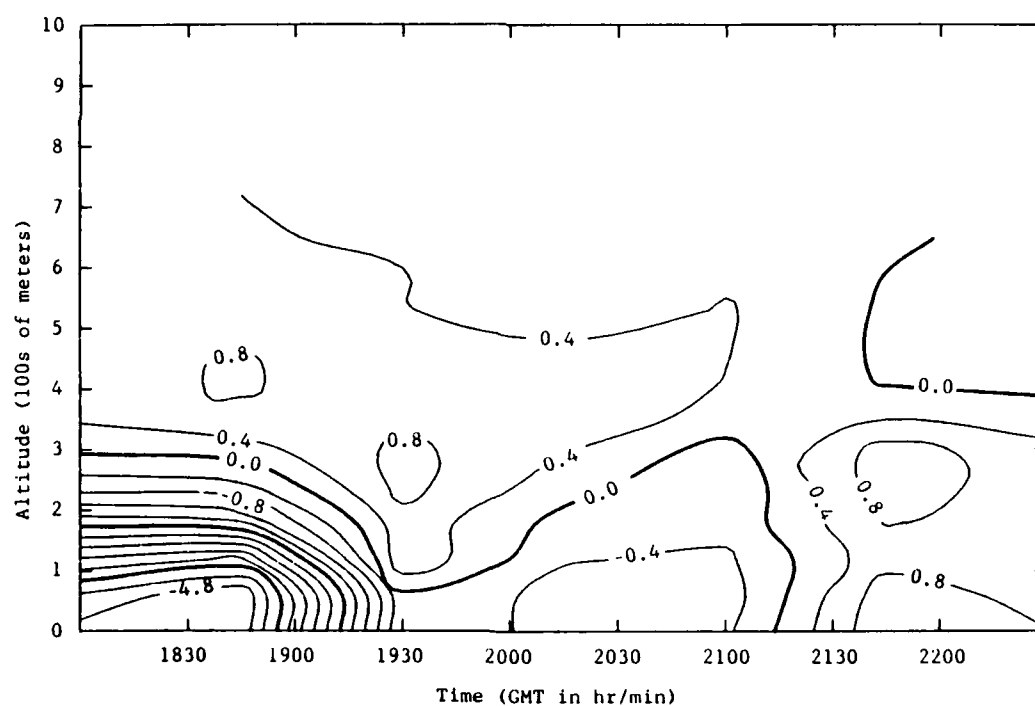


Figure 5.2c Time-height plot of horizontal divergence (10^4 s^{-1}) during the 8 March 1986 MABL radar study for the VAD analysis radius of 5 kilometers.

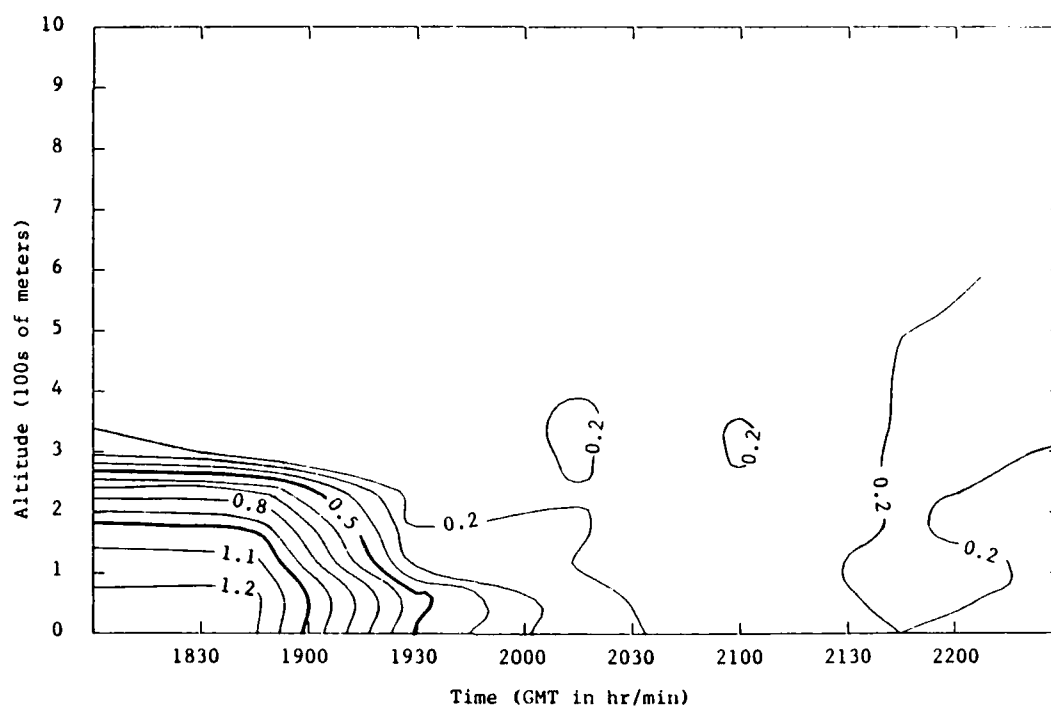


Figure 5.2d Time-height plot of horizontal deformation (10^{-3} s^{-1}) during the 8 March 1986 MABL radar study for the VAD analysis radius of 5 kilometers.

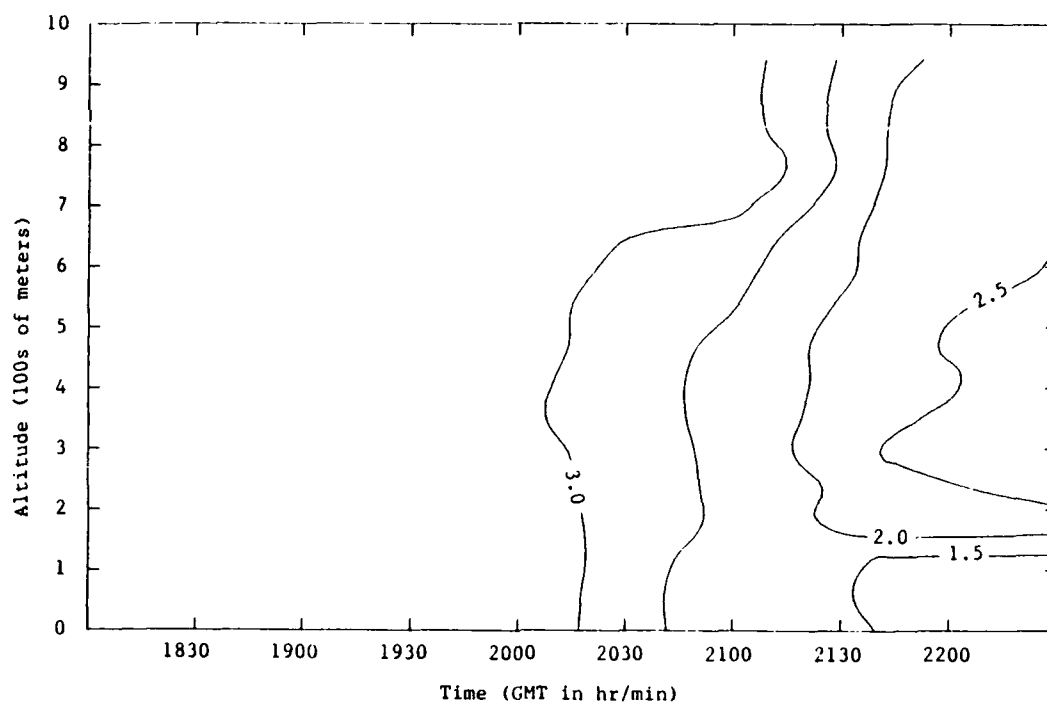


Figure 5.3a Time-height plot of horizontal wind speed (ms^{-1}) during the 8 March 1986 MABL radar study for the VAD analysis radius of 10 kilometers.

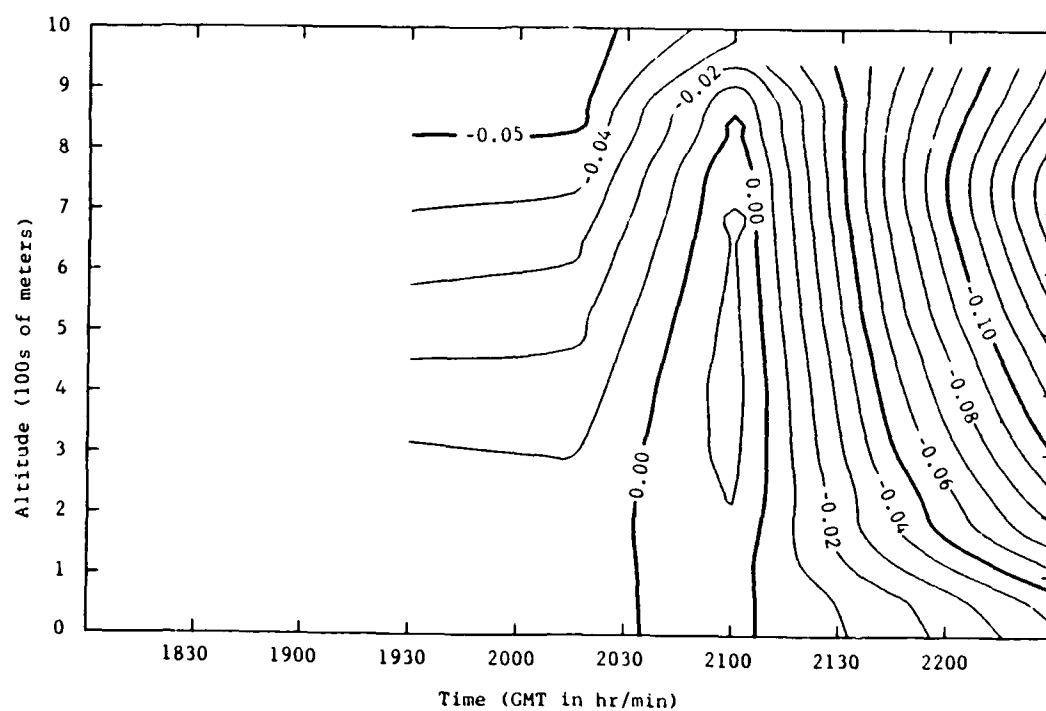


Figure 5.3b Time-height plot of vertical velocity (ms^{-1}) during the 8 March 1986 MABL radar study for the VAD analysis radius of 10 kilometers.

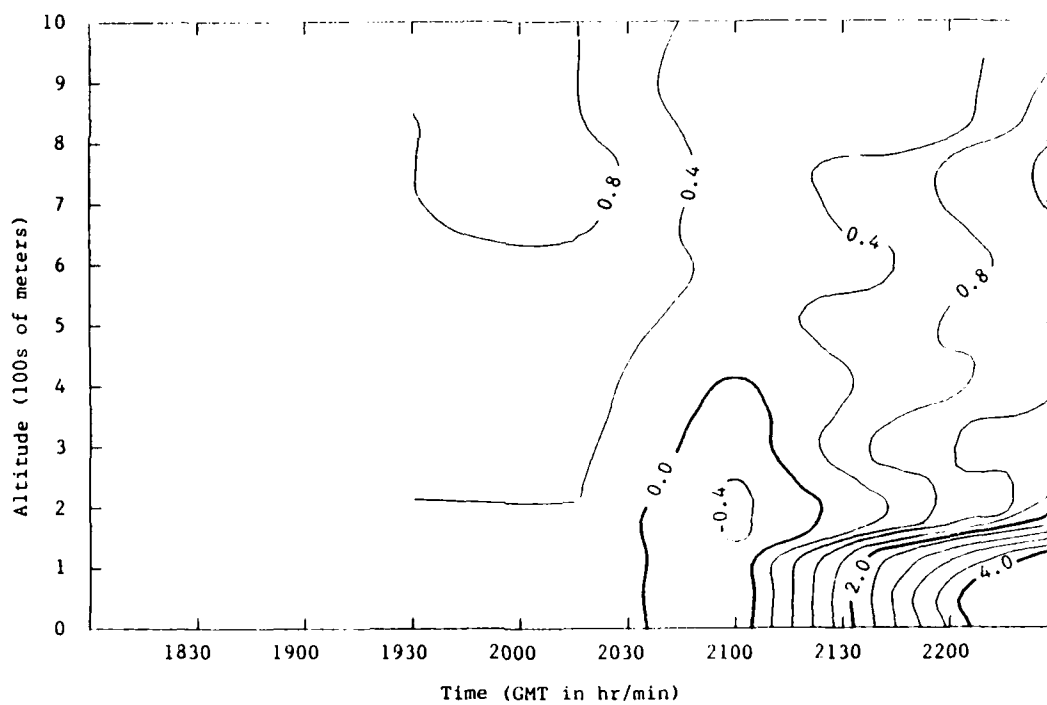


Figure 5.3c Time-height plot of horizontal divergence (10^{-4} s^{-1}) during the 8 March 1986 MABL radar study for the VAD analysis radius of 10 kilometers.

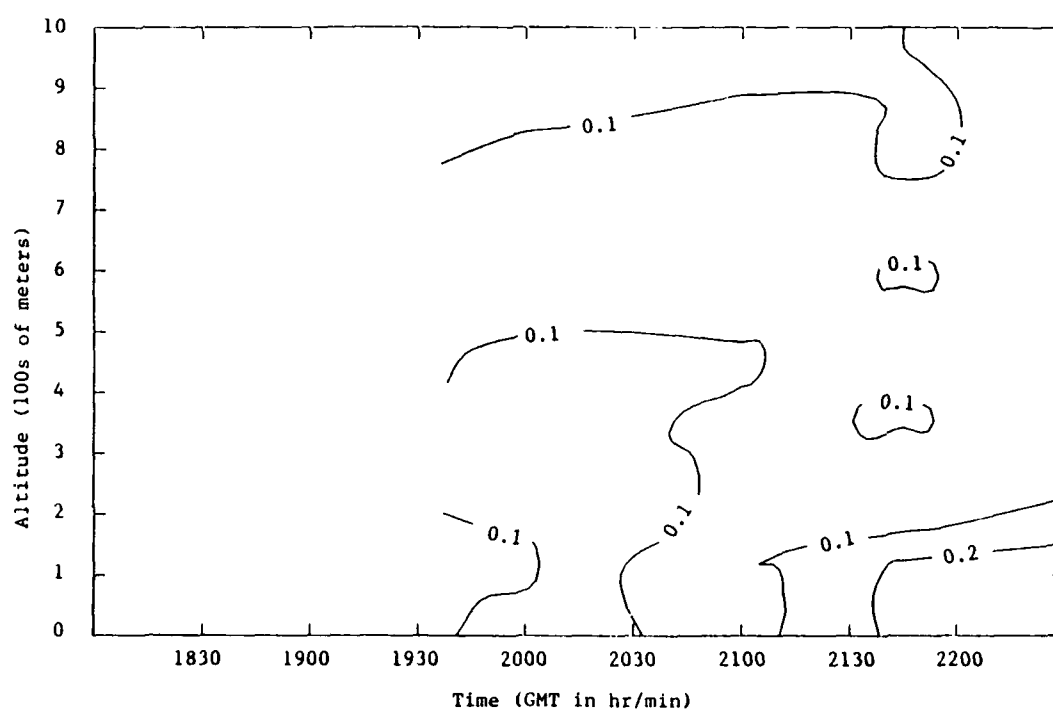


Figure 5.3d Time-height plot of horizontal deformation(10^{-3}s^{-1}) during the 8 March 1986 MABL radar study for the VAD analysis radius of 10 kilometers.

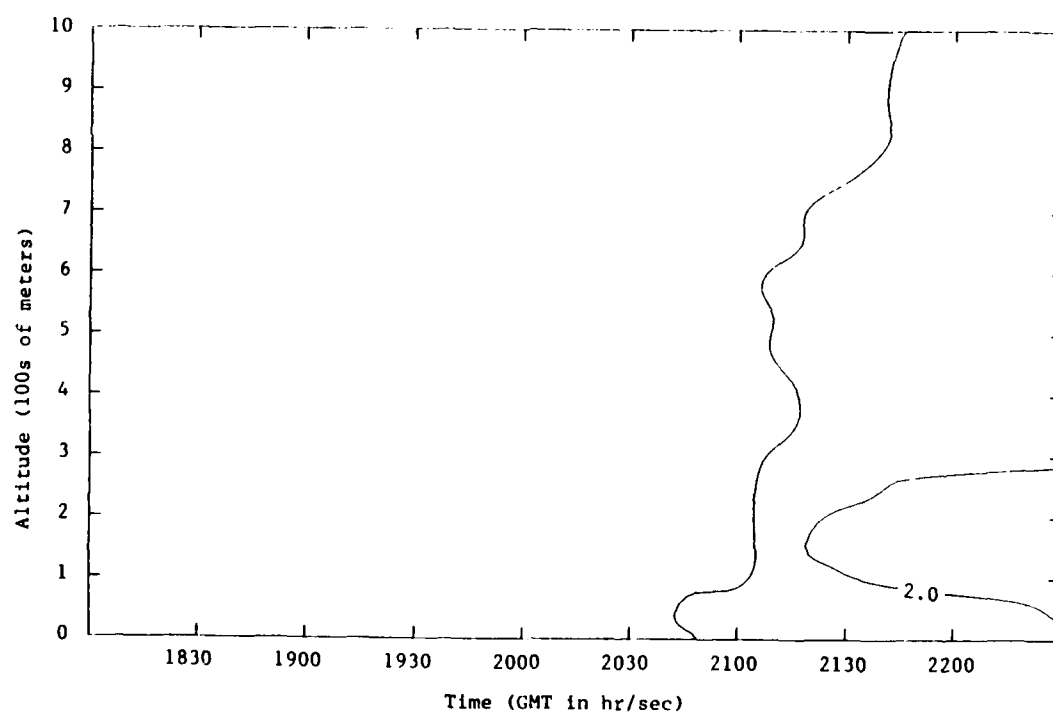


Figure 5.4a Time-height plot of horizontal wind speed (ms^{-1}) during the 8 March 1986 MABL radar study for the VAD analysis radius of 15 kilometers.

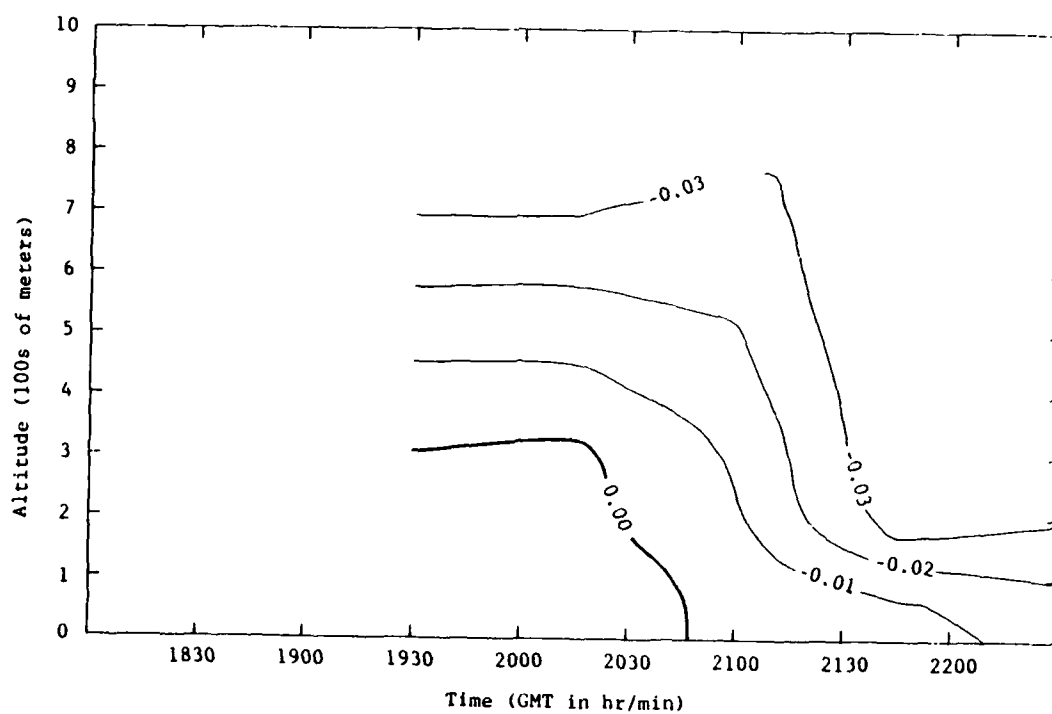


Figure 5.4b Time-height plot of vertical velocity (ms^{-1}) during the 8 March 1986 MABL radar study for the VAD analysis radius of 15 kilometers.

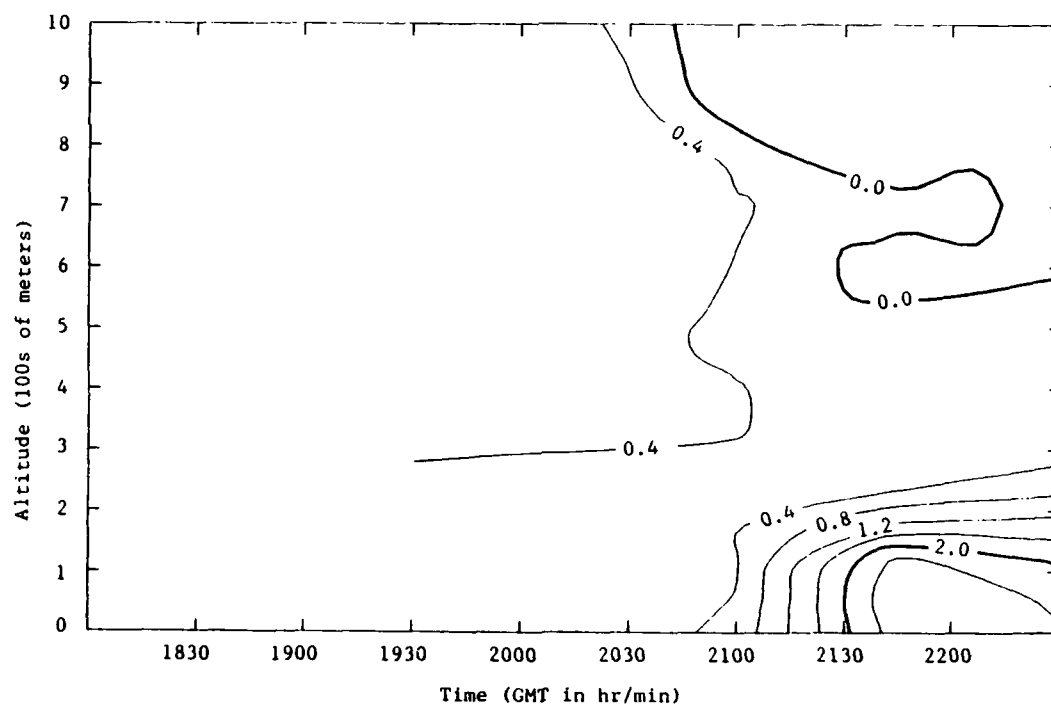


Figure 5.4c Time-height plot of horizontal divergence (10^{-4} s^{-1}) during the 8 March 1986 MABL radar study for the VAD analysis radius of 15 kilometers.

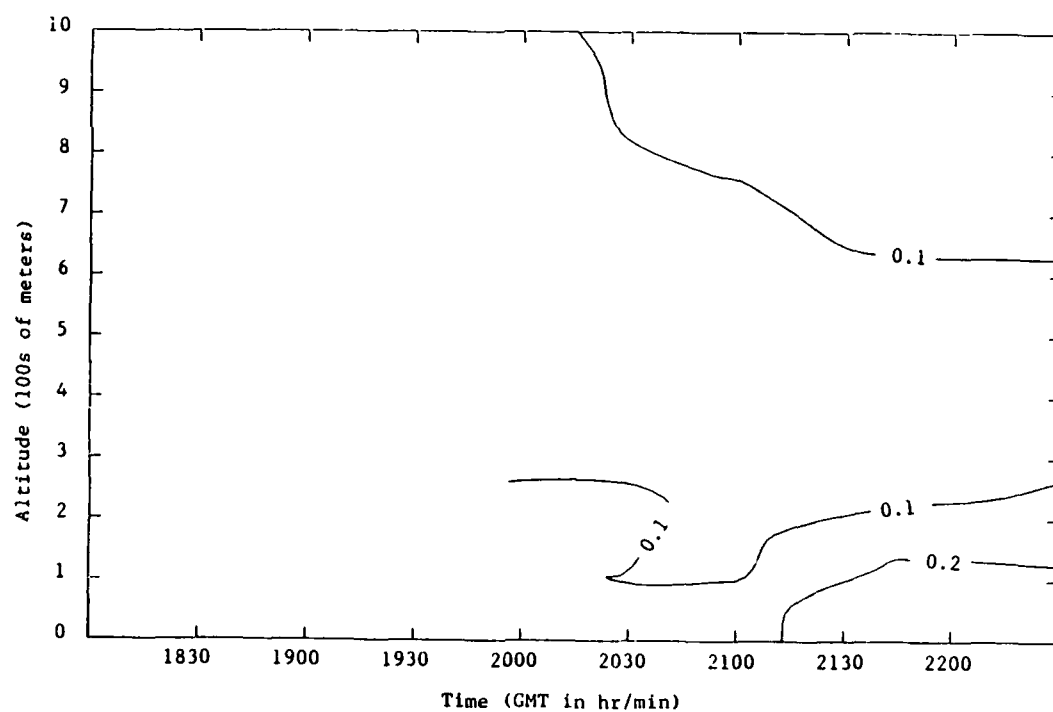


Figure 5.4d Time-height plot of horizontal deformation (10^{-3} s^{-1}) during the 8 March 1986 MABL radar study for the VAD analysis radius of 15 kilometers.

velocity changed to subsidence in all but the lowest 100 meters. Likewise, the vigorous convergence which previously characterized the lower 300 meters of the MABL changed to weak divergence in all but the lowest 75 meters, where convergence was minimal.

The sudden change in turbulence characteristics trend to stability during the first hour of the study period reversed itself rather quickly. By 2000 GMT, both convergence and upward vertical velocity were increasing. Within an hour, weak positive vertical velocity once again extended upward to about 500 meters, and convergence dominated the lower 300 meters of the MABL. The trend of diminishing horizontal wind speed and deformation continued as before. Recalling that the NWS rawinsonde data indicated the stability transition at approximately 2100 GMT, the reason for the brief episode of relative stability around 1930 GMT is rather obscure. A certain degree of disparity can be attributed to the fact that the 1830 VAD analysis was performed on data acquired with the CP-4 radar at Cape Hatteras whereas the 1930 and subsequent VADs are from the CP-3 radar, located over 40 kilometers away at Ocracoke. When considering the relatively small area over which data were analyzed, the sizeable distance between the radars, and a temporal separation of an hour in a rapidly changing atmospheric environment, a discontinuity in the 5 kilometer time-height plots is certainly understandable. However, these facts do not fully account for how quickly and the degree to which the kinematic properties change amidst the slowly evolving meso- α and β scenarios (as detailed in Chapter 4).

The final hour of the study period shows an unmistakable transition to stability. By 2130 GMT, subsidence and divergence are pervasive through the depth of the boundary layer, coinciding with the transition time indicated by the rawinsonde derived lapse rates. Note, however, that horizontal deformation, which was virtually nonexistent at 2100 GMT, shows a weak but definite increase after 2130 GMT. Comparing the divergence and deformation plots, not only during the last hour but through the entire period, it is readily apparent that deformation values are directly related to changes in the magnitude of divergence.

Figure 5.3a through 5.3d represent the same sequence of time-height plots as just described, but for a 10 kilometer VAD analysis radius. Note that for these figures, the data do not begin until 2000 GMT and thus do not depict the initial fully turbulent MABL. However, the brief episode of stability, subsequent return to turbulent instability, and final transition to a fully stable environment are depicted by these figures. Of particular interest is the enhanced pronouncement of these transitions. The early transition to stability depicted by the 10 kilometer analyses were of greater duration and intensity than for the 5 kilometer analyses. Subsidence and divergence extended downward through the depth of the mixed layer and remained as such until after 2030 GMT. The return to turbulent instability, though brief, was likewise more pronounced. Upward vertical velocity, though relatively weak, had values better than twice those of the corresponding 5 kilometer analysis, and reached a height of over 800 meters ASL. Low level convergence, though comparable in magnitude, extended upward nearly one

hundred meters further in the 10 kilometer analysis. Both the 5 and 10 kilometer time-height plots showed an abrupt transition to stable conditions shortly after 2100 GMT. Again, divergence and subsidence values are significantly greater in the 10 kilometer analyses, roughly three times those in the 5 kilometer plots.

The primary differences between the results of the 5 and 10 kilometer analyses were the relative brevity of the return to turbulent instability in the 10 kilometer plots, and the substantially greater intensity of these same plots in both property values and spatial extent. A viable explanation for these differences lies in the observation by Rabin and Zrnic (1980) that the smaller the VAD sampling area, the greater the temporal and spatial variation of divergence measurements, and that at such small scales (VAD analysis radii of less than 20 kilometers) the cellular structures chiefly responsible for this phenomenon are of a transient nature. Note that in an essentially closed circulation pattern, as was the case here with a subsidence inversion-capped MABL, the kinematic properties of divergence, vertical velocity, and deformation are substantially interdependent. Hence, the inverse relationship between divergence variability and sampling area can likewise be extended to vertical velocity and deformation analyses.

Figures 5.4a through 5.4d represent the same sequence of time-height plots, but for a 15 kilometer radius of analysis. These results are rather limited when considering that the temporal range of data extends over a period of only one and one-half hours. In spite of this limitation, several items of interest were evident. The transition to stability occurred earlier, just prior to 2100 GMT, than with analyses

of smaller sampling areas. Also, Figure 5.4a depicts a slight decrease in horizontal wind speed between 100 and 250 meters ASL. Another revelation is the decrease of vertical velocity and divergence values, roughly half their corresponding magnitude in the 10 kilometer analysis. Finally, though weak in all but the lowest 200 meters at 2130 GMT, divergence dominates virtually the entire depth of the mixed layer. This last observation is attributable to the fact that the rather extensive near shore meso- β divergence, previously discussed in Chapter 4, probably exerted a significantly greater influence on this largest of analysis radii. The other noted differences between the 10 and 15 kilometer analysis radii may also relate to the greater influence of meso- β effects on increased sampling area.

5.2 Low-level Wind Shear

5.2.1 VSLICE Profile

The VSLICE technique, briefly described in Section 3.3.2, was employed at 2103 GMT, along a line roughly 20 kilometers to the west-northwest of CP-3, the location of which is schematically depicted in Figure 5.5a. The VSLICE is presented as Figure 5.5b. Note that in this figure the white crosses are spaced at 5 kilometer and 500 meter horizontal and vertical intervals, respectively. Now recall that positive radial velocity indicates movement away from the radar, and vice versa. Of particular interest in this figure is the transition from negative to positive radial velocity in the lowest 250 meters, across the VSLICE from right to left, while above this height the radial velocity is essentially negative. This distribution of radial velocities

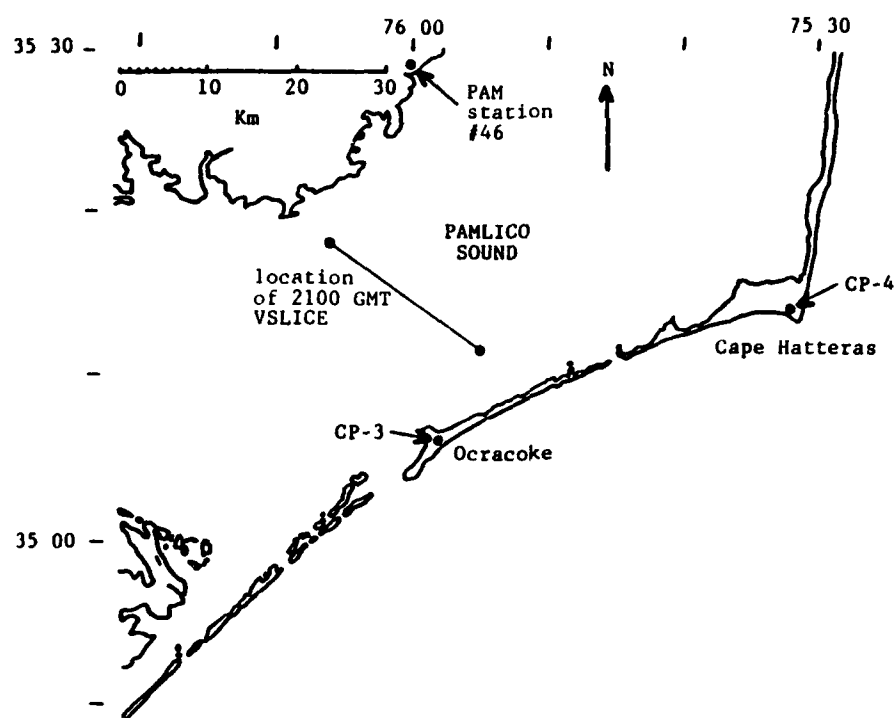


Figure 5.5a Location of the 8 March 1986, 2103 GMT, VSLICE.

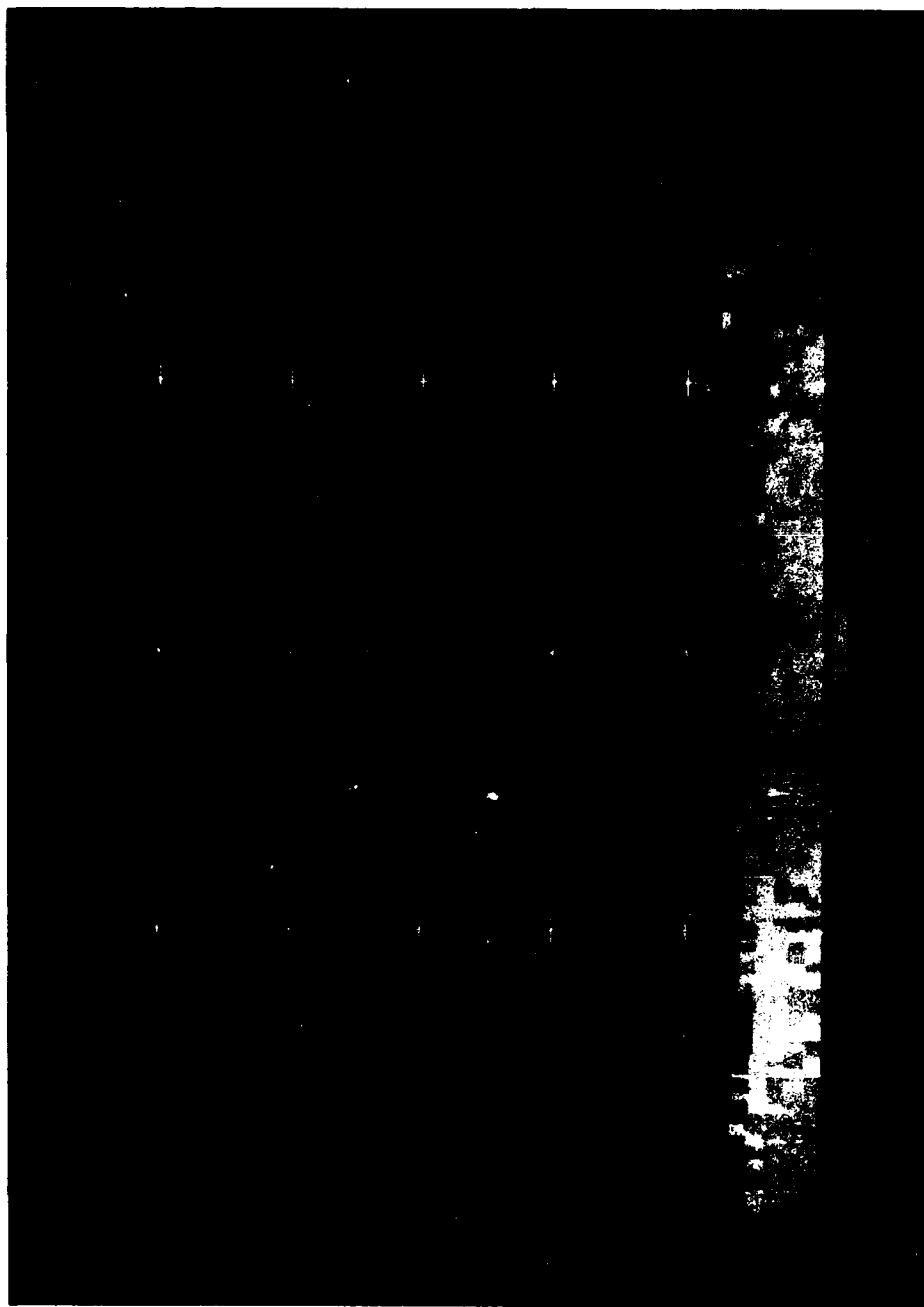


Figure 5.5b VSLICE of radial velocity over Pamlico Sound, constructed from the volume of data taken by the CP-3 radar at 2103 GMT on 8 March 1986.

depicts the spatial transition from an essentially unidirectional flow through the depth of the mixed layer to a strong directional shear between approximately 200 and 300 meters ASL (extreme left in the referenced figure). The low-level counter-gradient flow indicated by this display is in agreement with the like phenomenon observed in the displays of PAM surface winds, Section 4.3.2, likely a result of the lateral shear arising from the surface roughness discontinuity between land and water.

5.2.2 VAD Derived Wind Profiles

Half-hourly plots of horizontal wind speed and direction were constructed from VAD derived data, presented as Figures 5.6 through 5.8. Data from the 5 kilometer analyses are depicted by the 5.6 series, with the 10 and 15 kilometer analyses corresponding to the 5.7 and 5.8 series, respectively. Each series will be examined independently, in order of increasing radius, with comparison discussion interspersed at appropriate points in the text.

The wind profiles from the 5 kilometer analyses, Figures 5.6a through 5.6g, yield little in terms of significant phenomena. Wind speeds showed only slight variation (not exceeding 1 meter per second) with height, except for the 1830 plot (Figure 5.6a) which increased by nearly 3 meters per second between 50 and 350 meters ASL. Directions were fairly consistent, typically showing an overall slight backing with increasing height. As the period progressed, wind speeds generally decreased and the direction profile, though retaining its backing characteristic, veered with time. These speed and direction

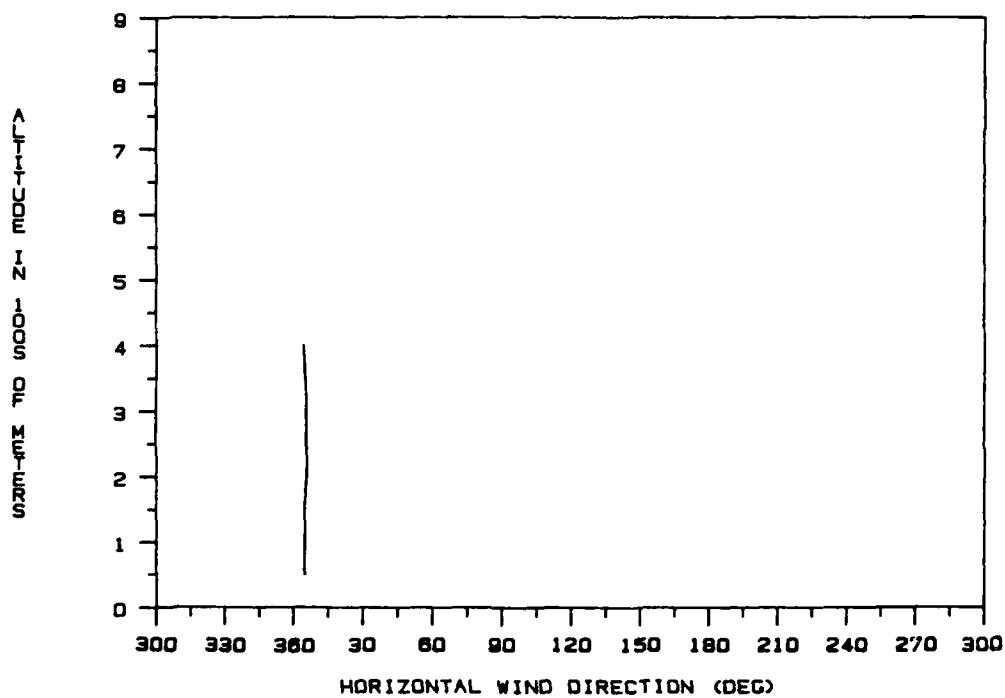
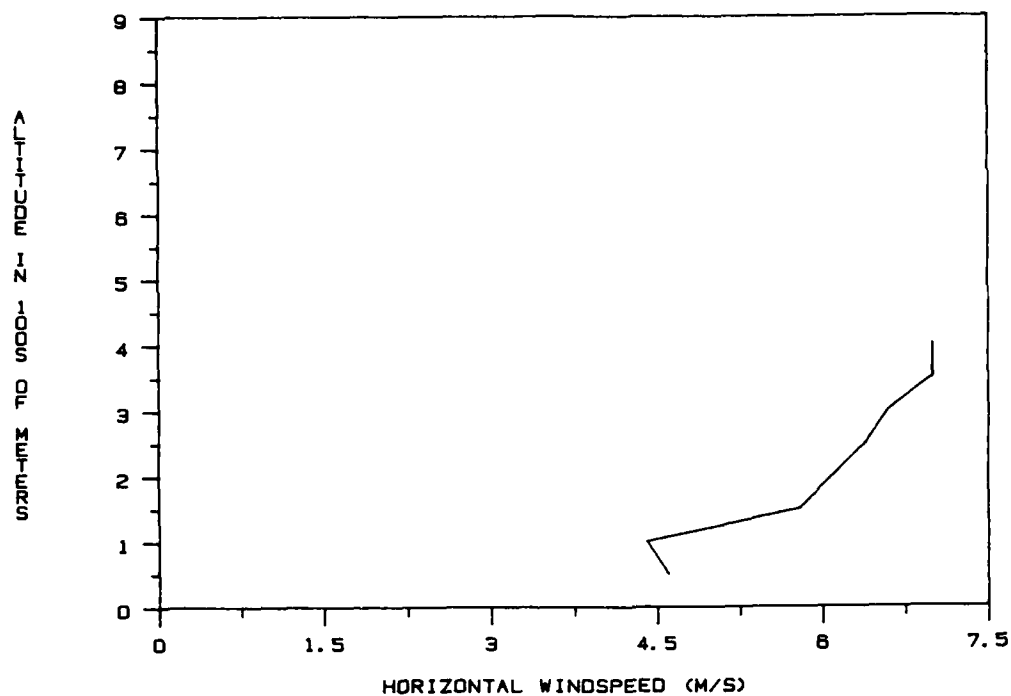


Figure 5.6a Plot of horizontal wind speed and direction versus altitude from the 5 kilometer radius VAD analysis taken by the CP-4 radar at 1831 GMT on 8 March 1986.

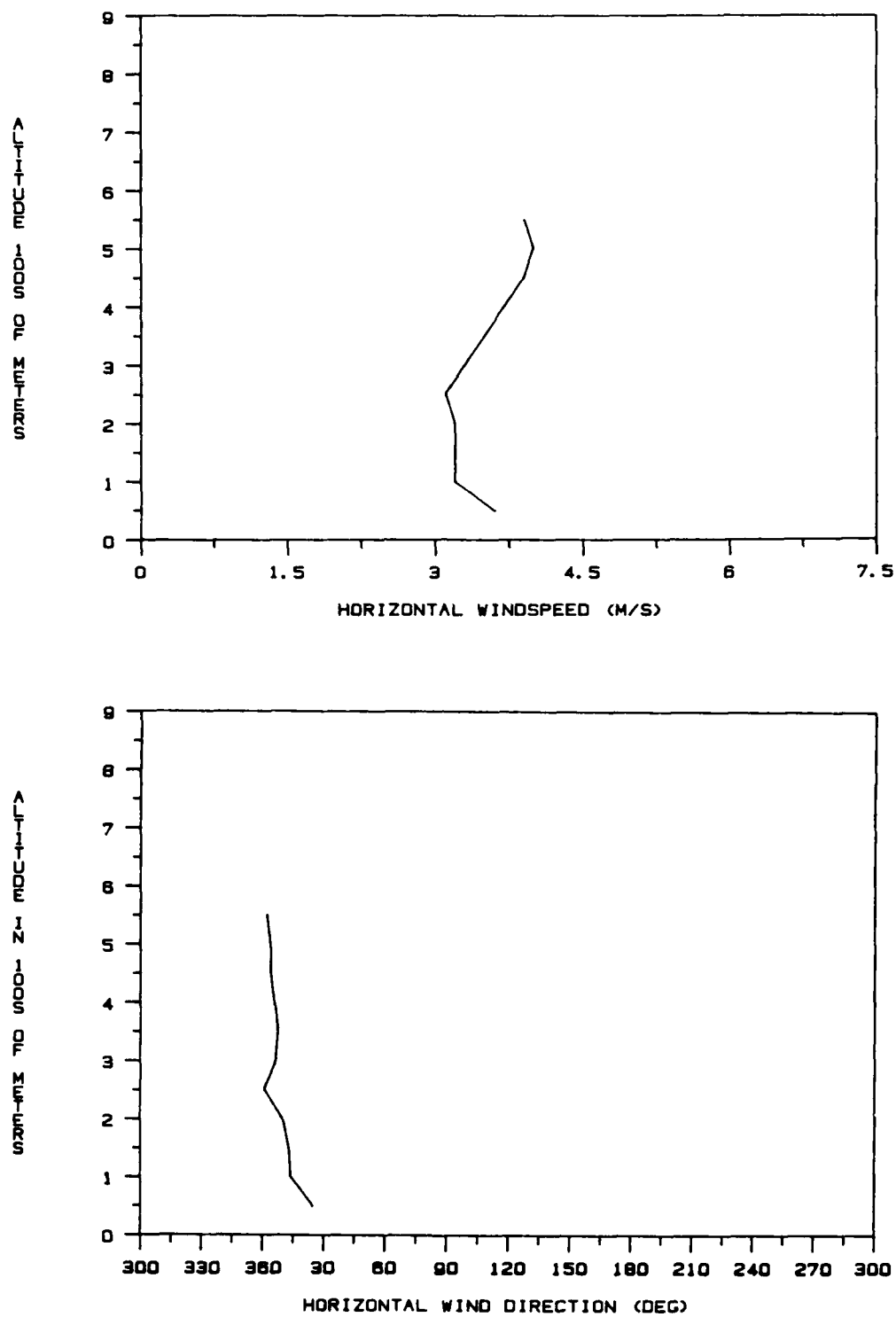


Figure 5.6b Plot of horizontal wind speed and direction versus altitude from the 5 kilometer radius VAD analysis taken by the CP-3 radar at 1934 GMT on 8 March 1986.

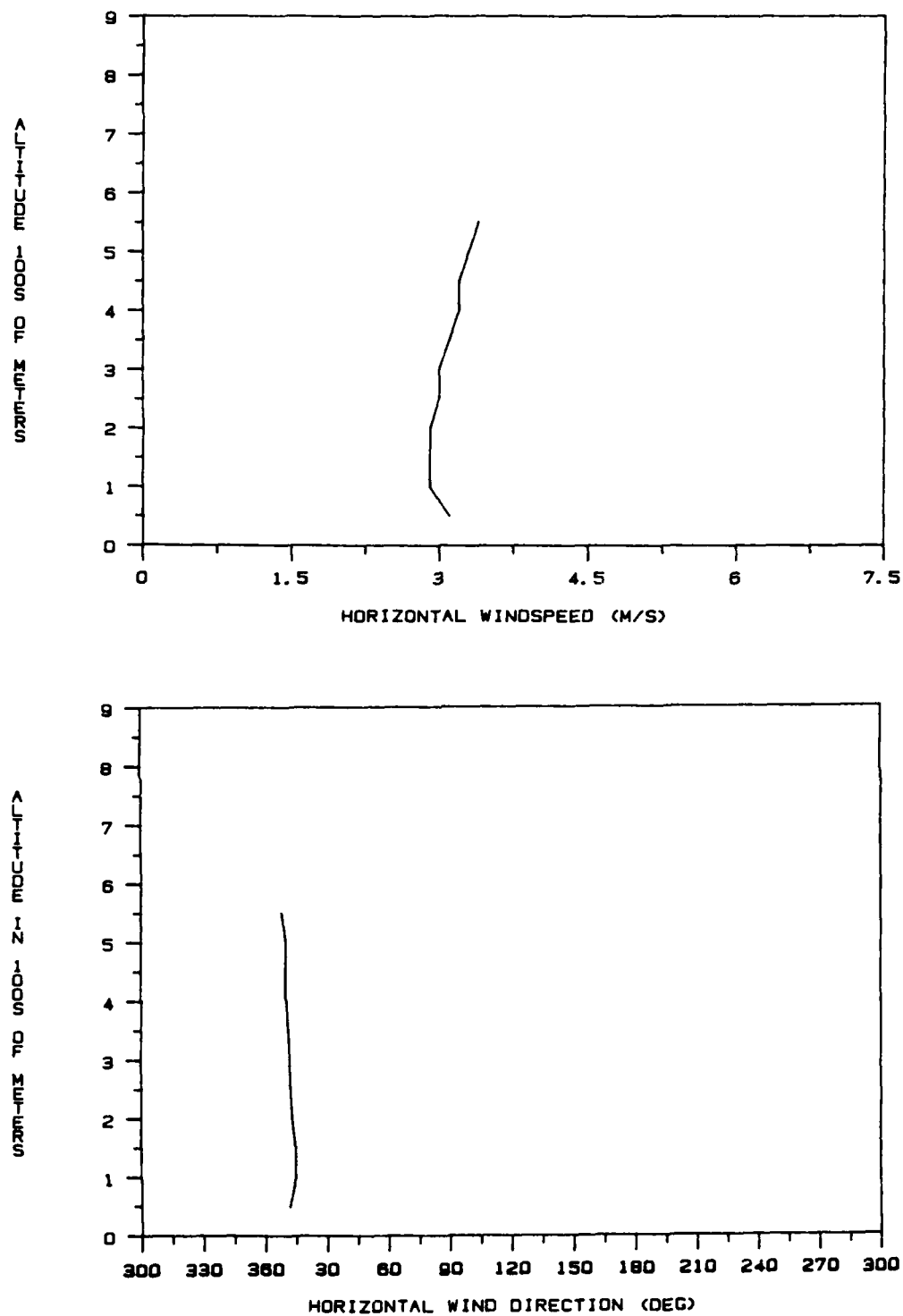


Figure 5.6c Plot of horizontal wind speed and direction versus altitude from the 5 kilometer radius VAD analysis taken by the CP-3 radar at 2003 GMT on 8 March 1986.

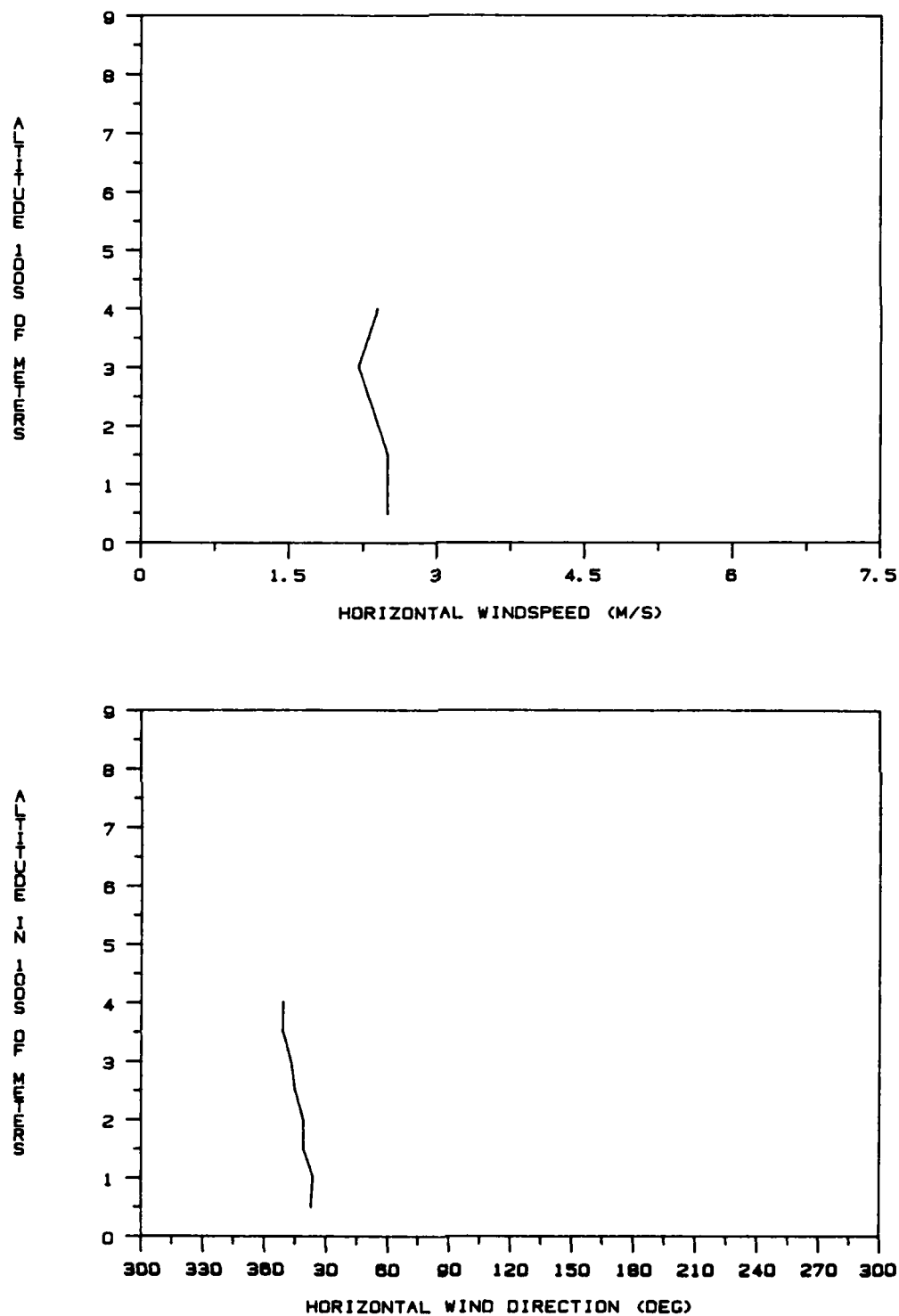


Figure 5.6d Plot of horizontal wind speed and direction versus altitude from the 5 kilometer radius VAD analysis taken by the CP-3 radar at 2034 GMT on 8 March 1986.

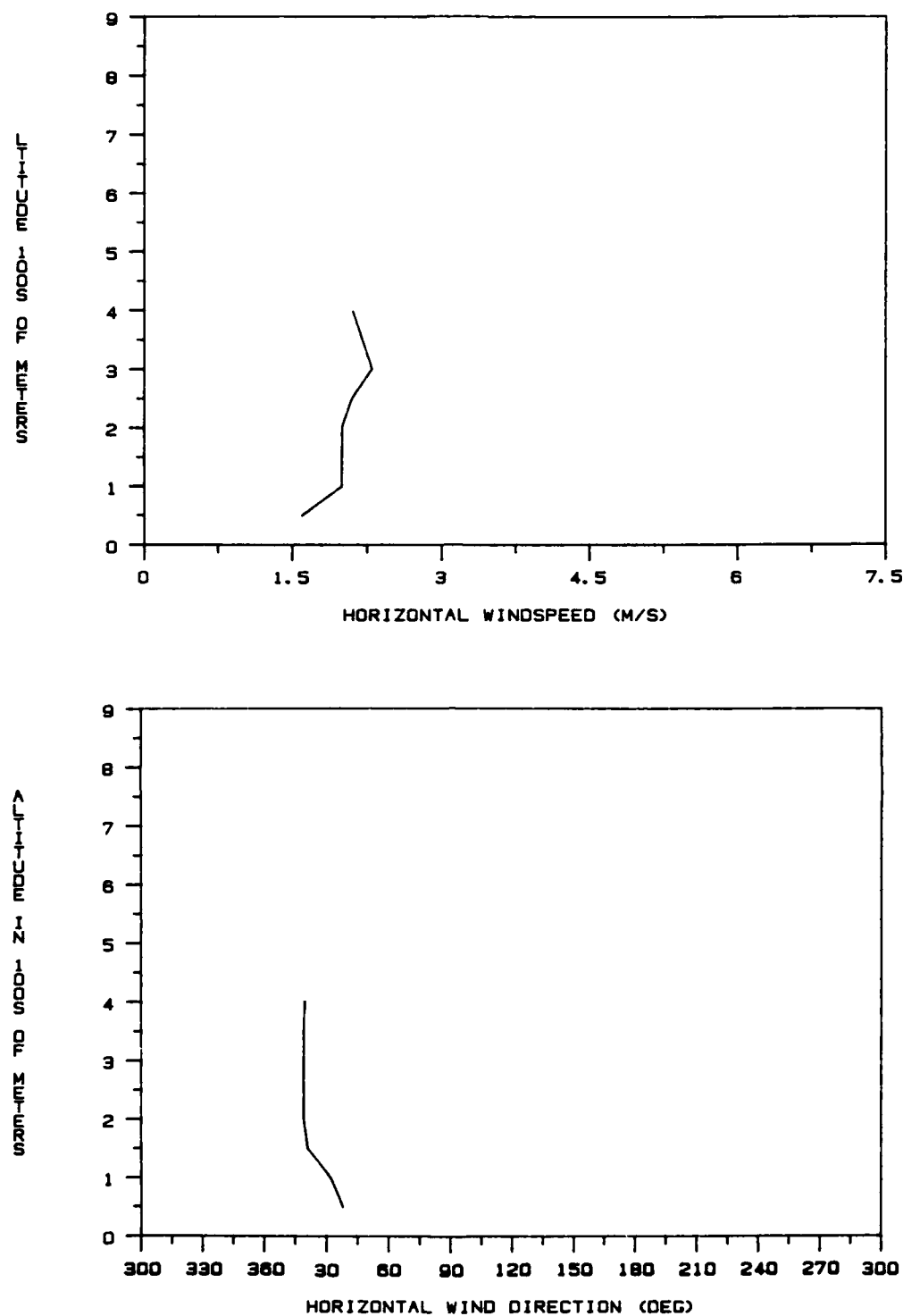


Figure 5.6e Plot of horizontal wind speed and direction versus altitude from the 5 kilometer radius VAD analysis taken by the CP-3 radar at 2103 GMT on 8 March 1986.

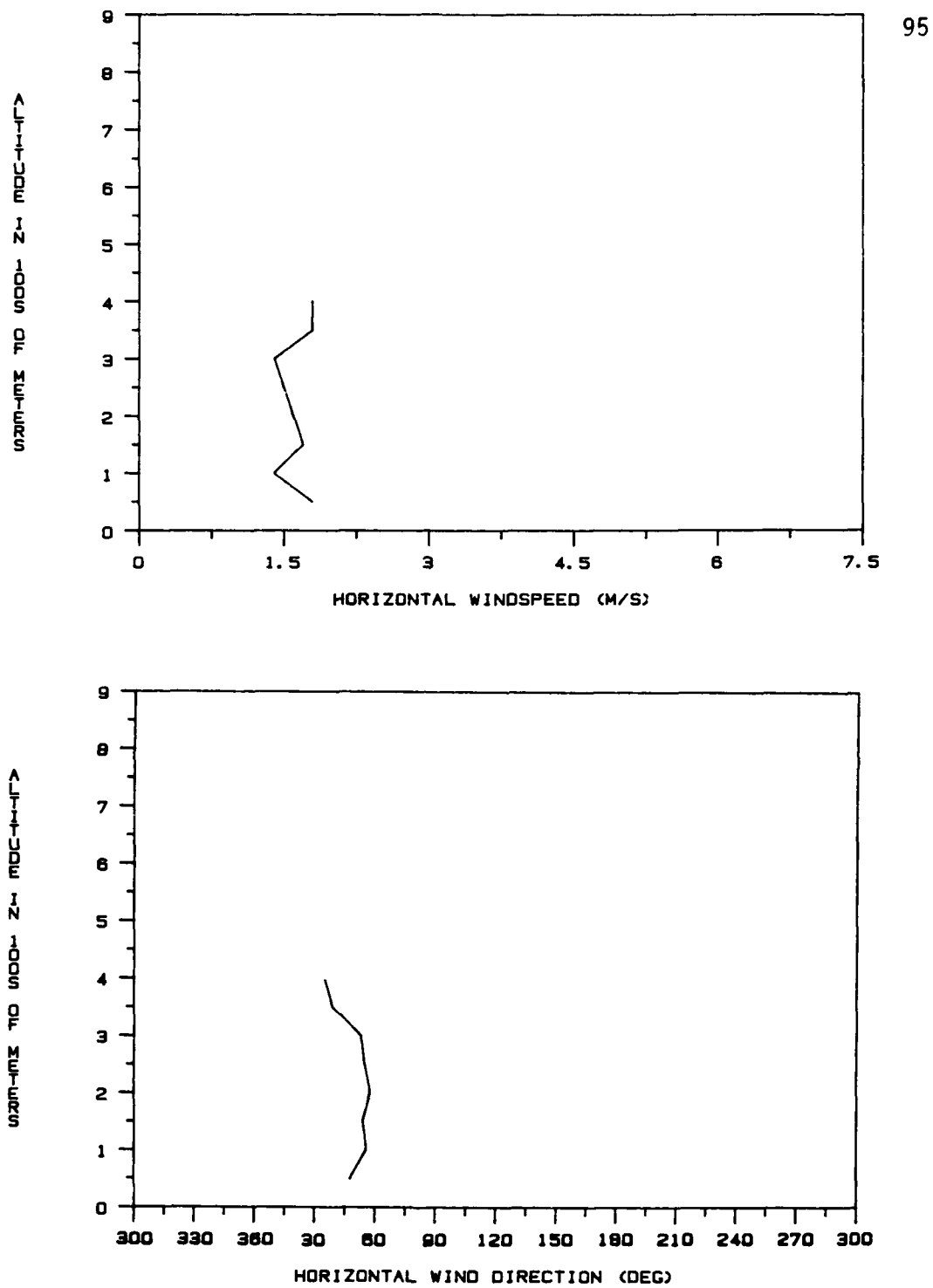


Figure 5.6f Plot of horizontal wind speed and direction versus altitude from the 5 kilometer radius VAD analysis taken by the CP-3 radar at 2131 GMT on 8 March 1986.

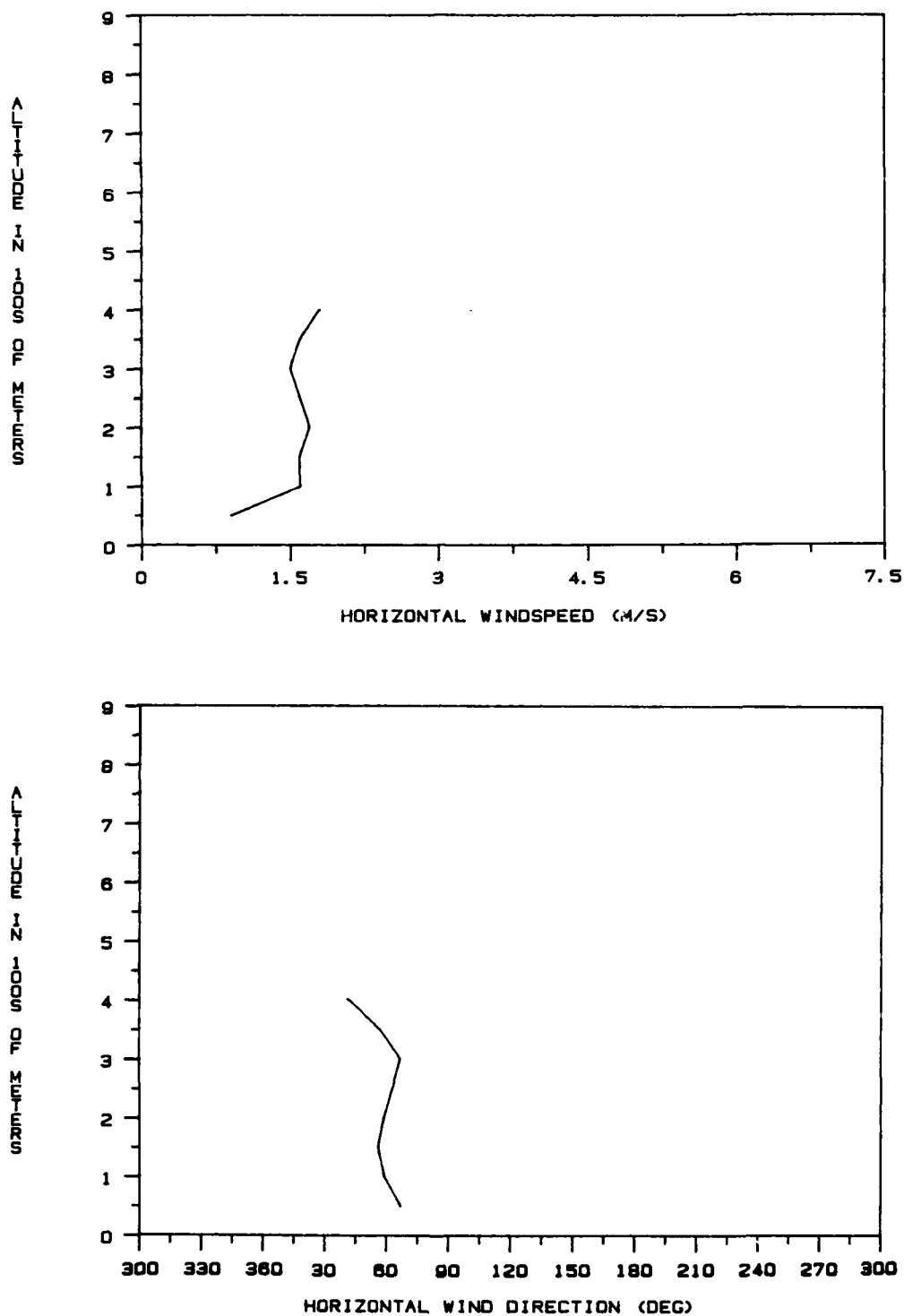


Figure 5.6g Plot of horizontal wind speed and direction versus altitude from the 5 kilometer radius VAD analysis taken by the CP-3 radar at 2201 GMT on 8 March 1986.

trends well coincide with the synoptic and meso- α scenario previously described.

Figures 5.7a through 5.7e are the wind profiles from the 10 kilometer VADs. These plots generally depict features and trends not unlike those described for the 5 kilometer series. Figure 5.7e, horizontal wind speed and direction profiles at 2200 GMT, is notably different than any discussed thus far. A 3 meter per second wind speed at 50 meters ASL increased to nearly 4.5 meters per second at 100 meters, followed by a decrease of over 3 meters per second in the next 50 meters of height. The speeds through the remainder of the column were on the order of 1 to 1.5 meters per second, except at 300 meters ASL where the wind speed was approximately 0.5 meters per second. This highly variable speed profile coincides well with the direction profile. The wind between 50 and 100 meters ASL was out of 190 degrees, substantially opposing the mean mixed layer flow. Between 100 and 200 meters ASL, the wind backed to 45 degrees, veered to 115 degrees at 300 meters, then resumed a northeasterly flow on upward through the remainder of the profile.

Recalling the strong vertical shear depicted by the 2103 GMT VSLICE, the profiles of Figure 5.7e illustrate the spatial extension of a low-level counter-gradient wind flow pattern. At least in the proximity of the radar network, the onshore component of flow was first evident at PAM station 46, 2030 GMT, followed by the VSLICE over Pamlico Sound at 2103 GMT, and these 10 kilometer VAD derived wind profiles at 2201 GMT. These combined results show the existence of such a wind field anomaly.

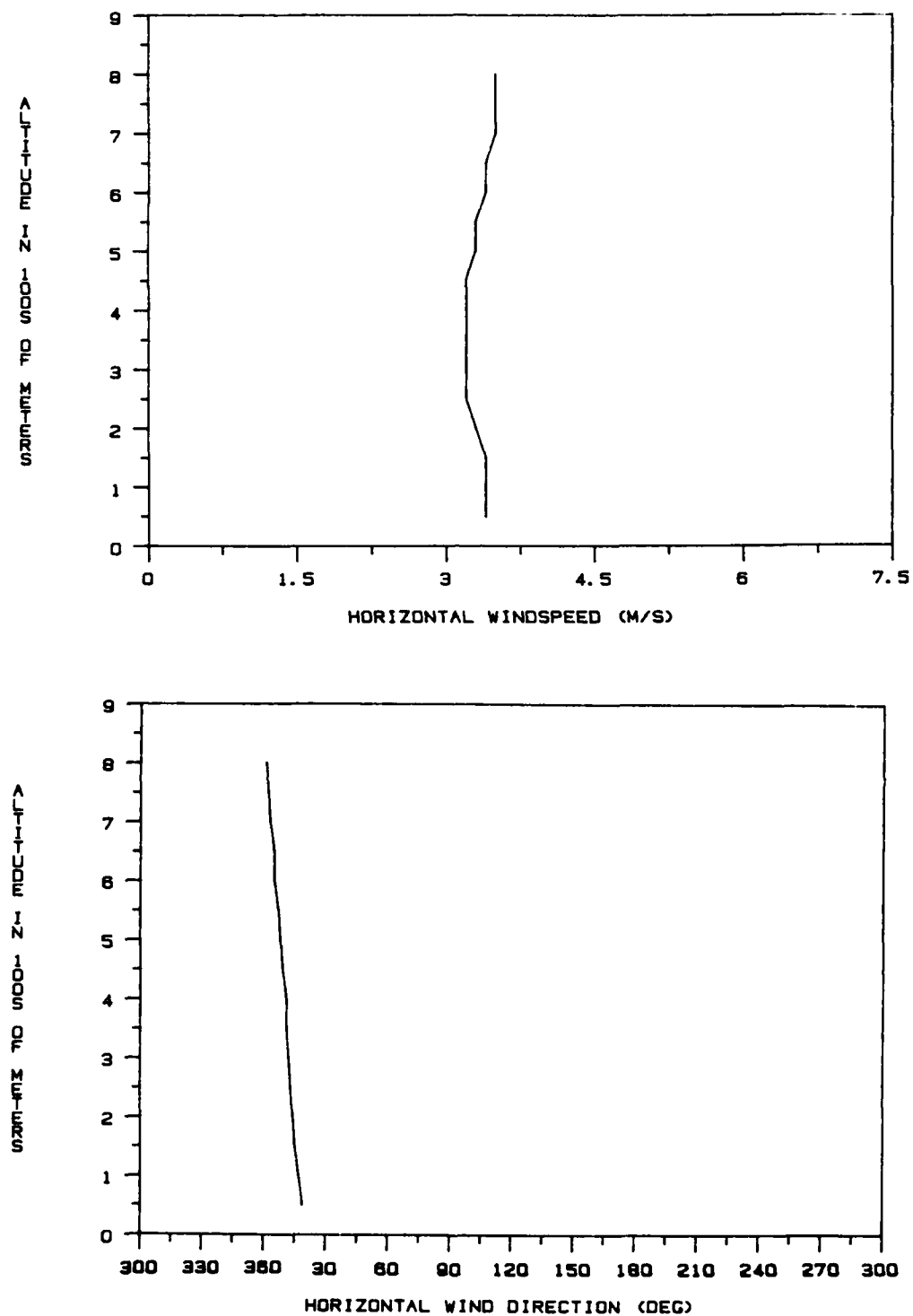


Figure 5.7a Plot of horizontal wind speed and direction versus altitude from the 10 kilometer radius VAD analysis taken by the CP-3 radar at 2003 GMT on 8 March 1986.

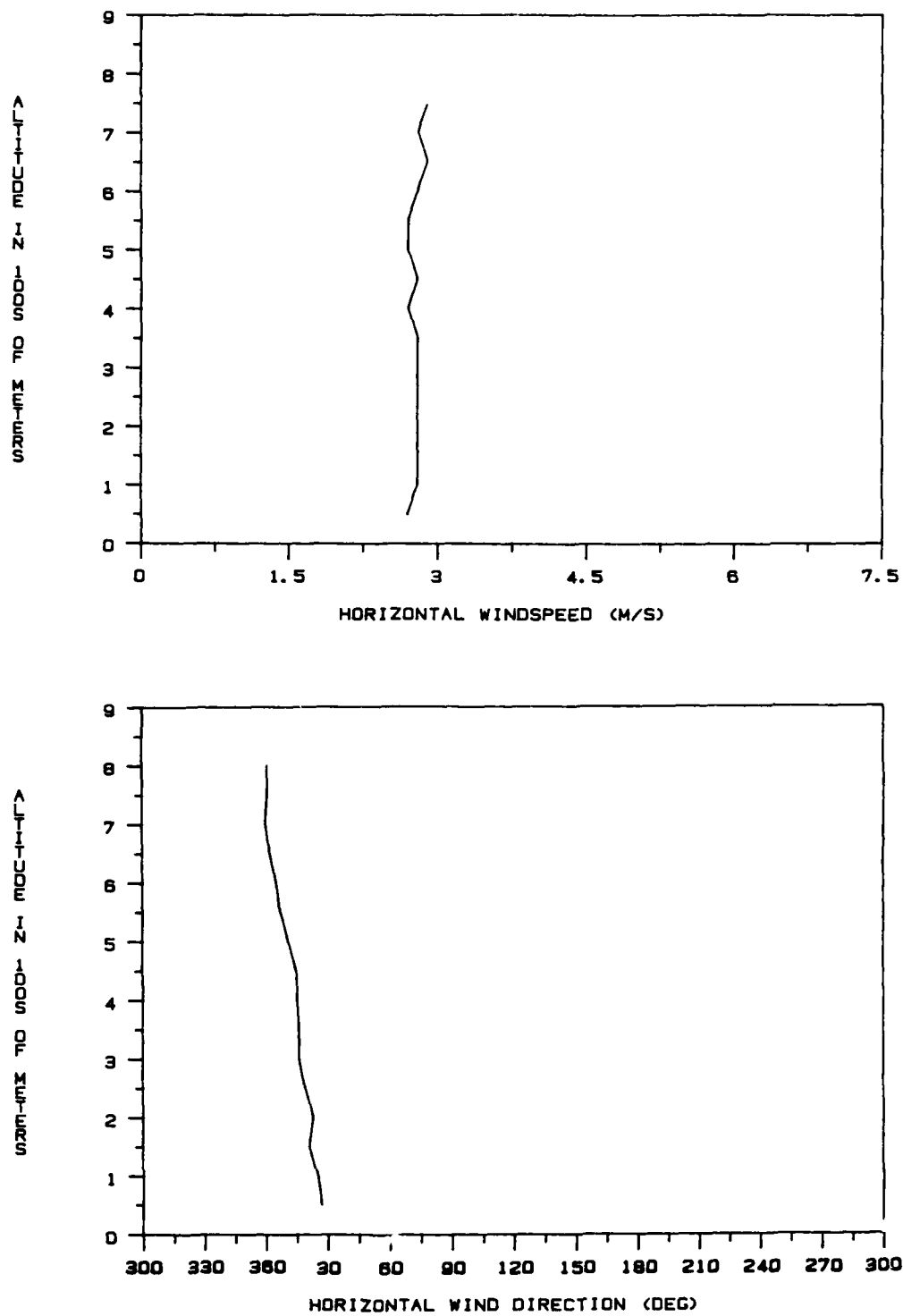


Figure 5.7b Plot of horizontal wind speed and direction versus altitude from the 10 kilometer radius VAD analysis taken by the CP-3 radar at 2034 GMT on 8 March 1986.

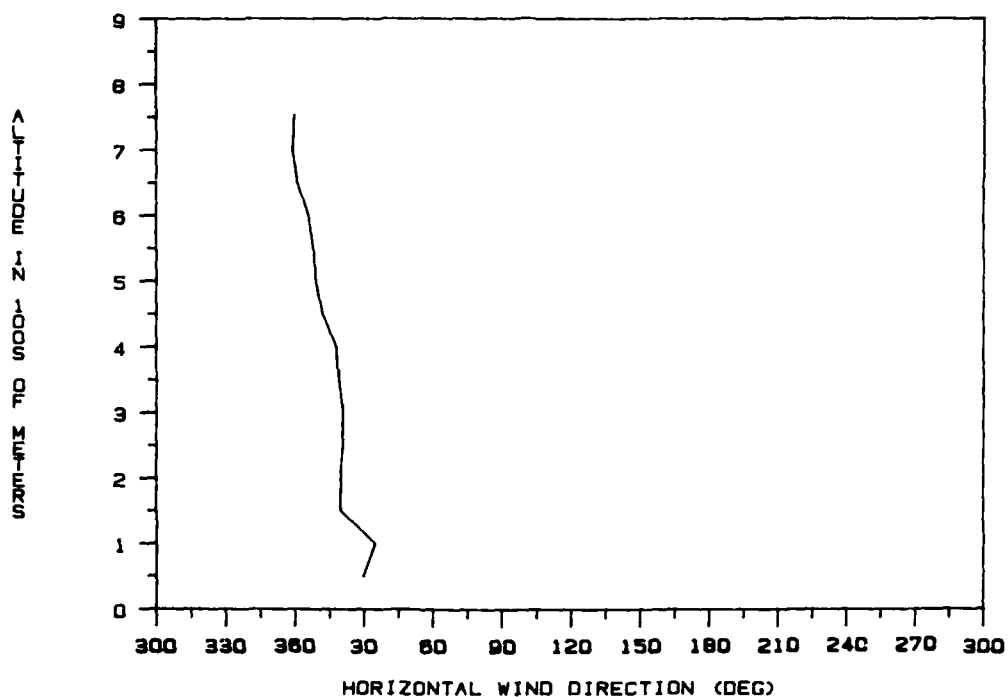
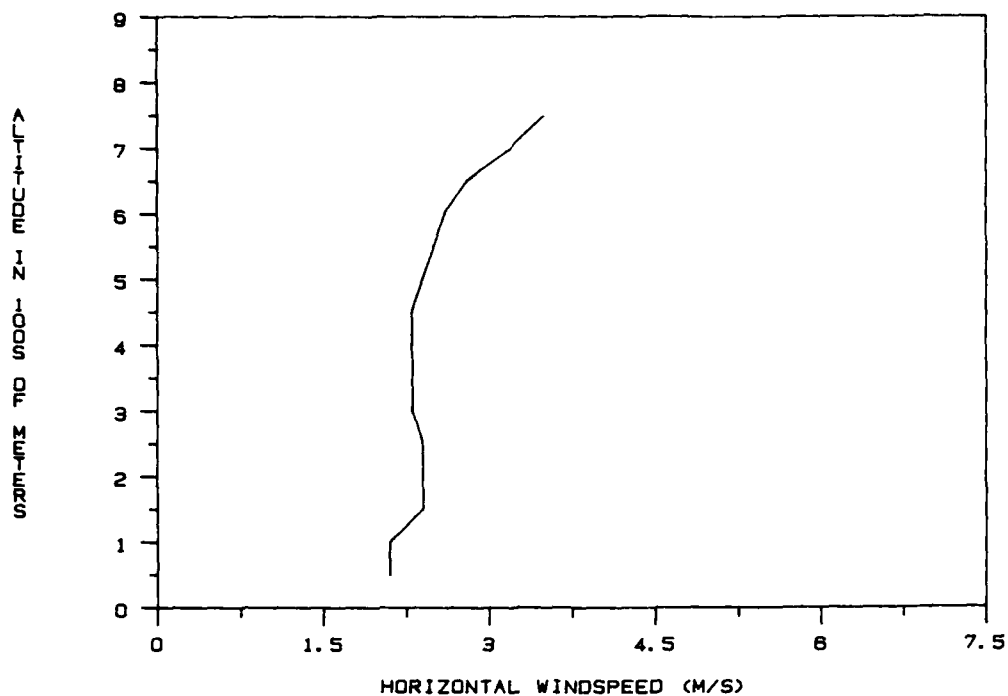


Figure 5.7c Plot of horizontal wind speed and direction versus altitude from the 10 kilometer radius VAD analysis taken by the CP-3 radar at 2103 GMT on 8 March 1986.

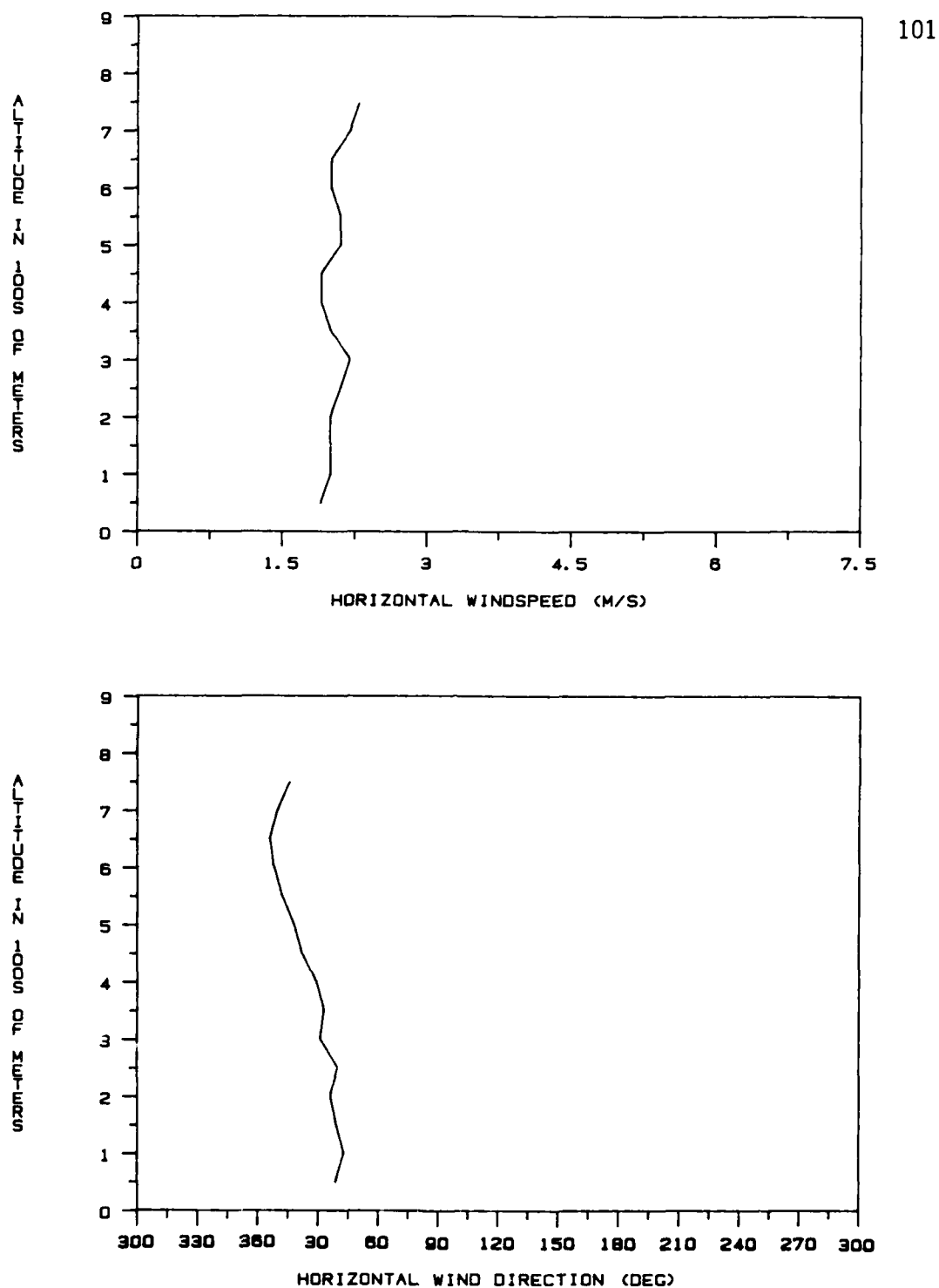


Figure 5.7d Plot of horizontal wind speed and direction versus altitude from the 10 kilometer radius VAD analysis taken by the CP-3 radar at 2131 GMT on 8 March 1986.

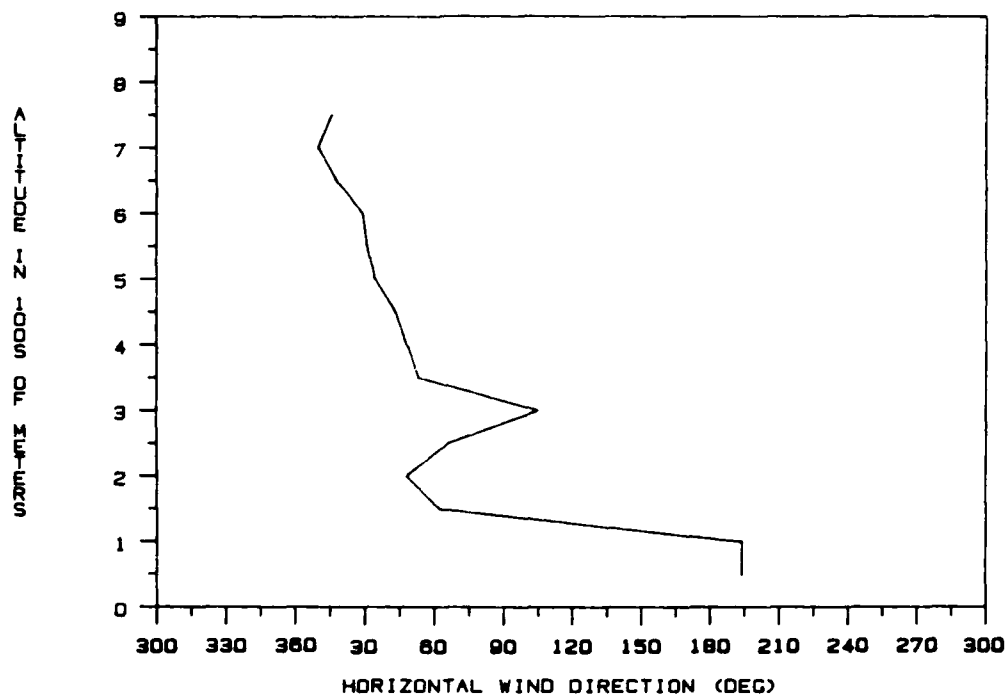
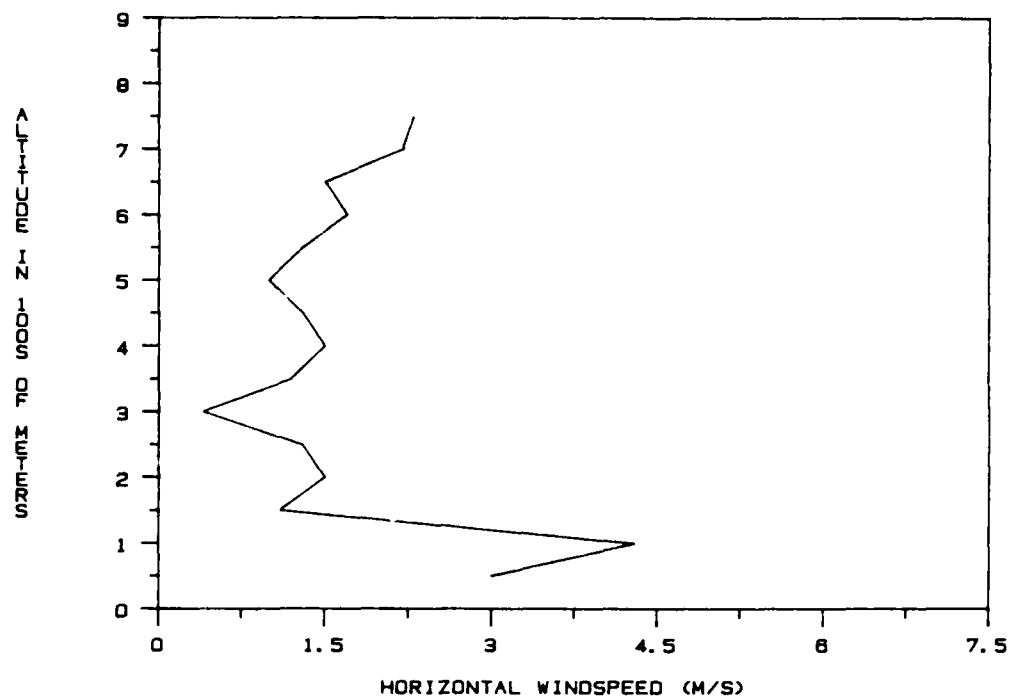
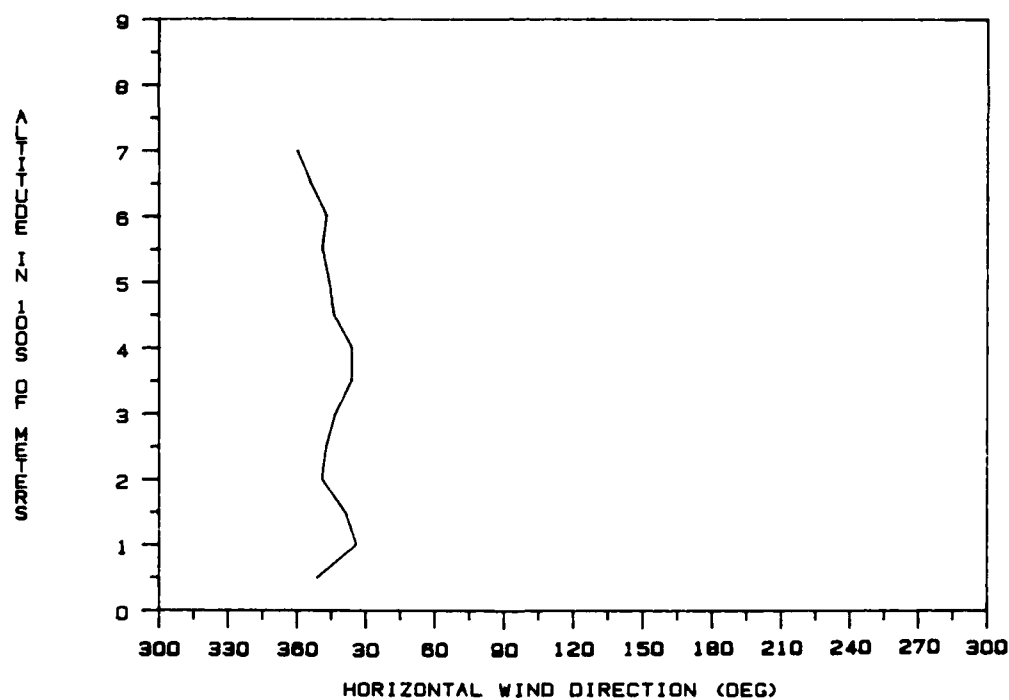
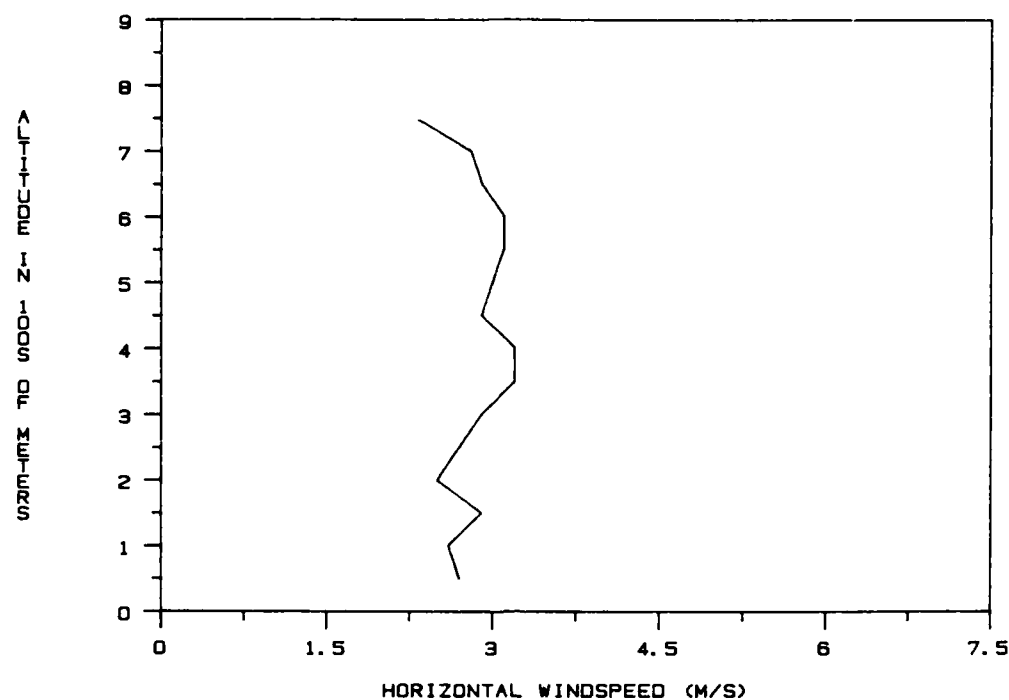
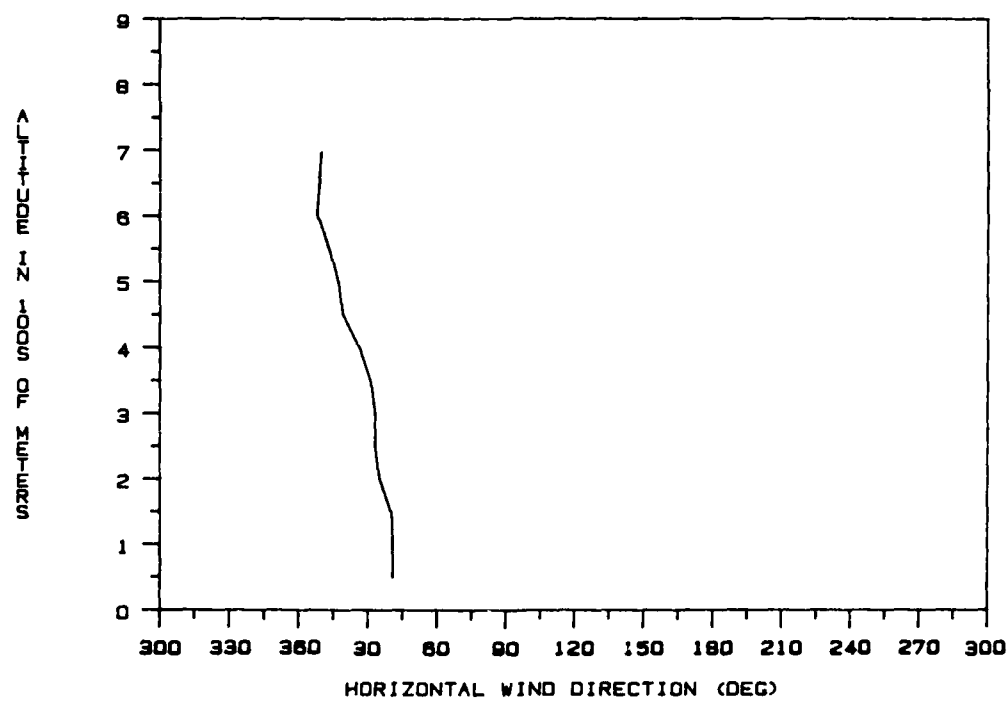
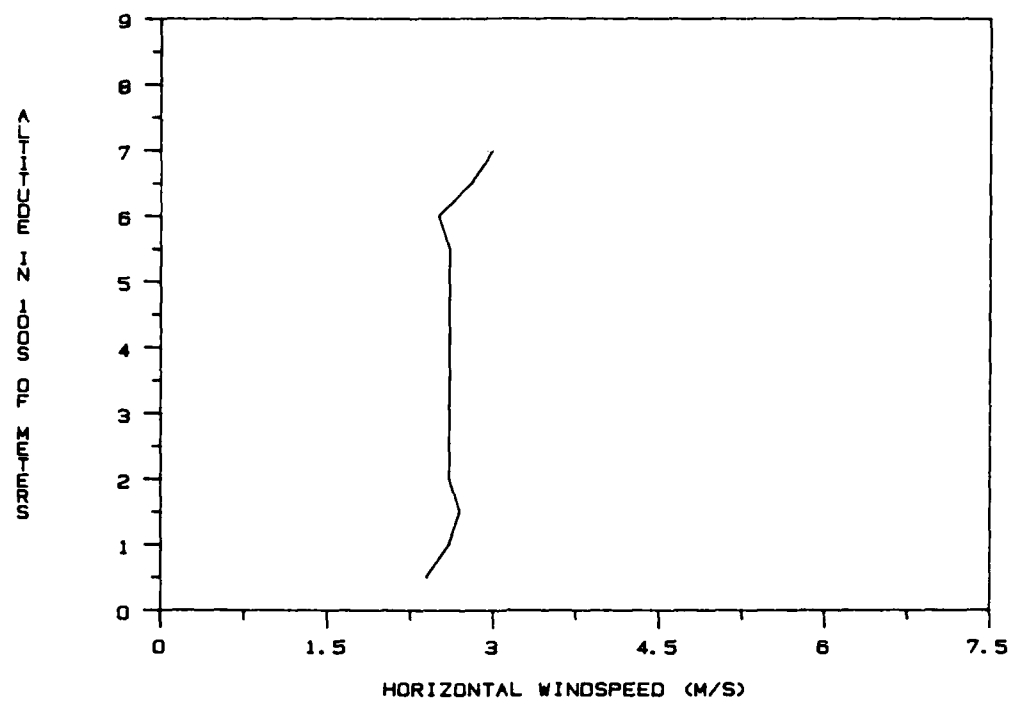


Figure 5.7e Plot of horizontal wind speed and direction versus altitude from the 10 kilometer radius VAD analysis taken by the CP-3 radar at 2201 GMT on 8 March 1986.

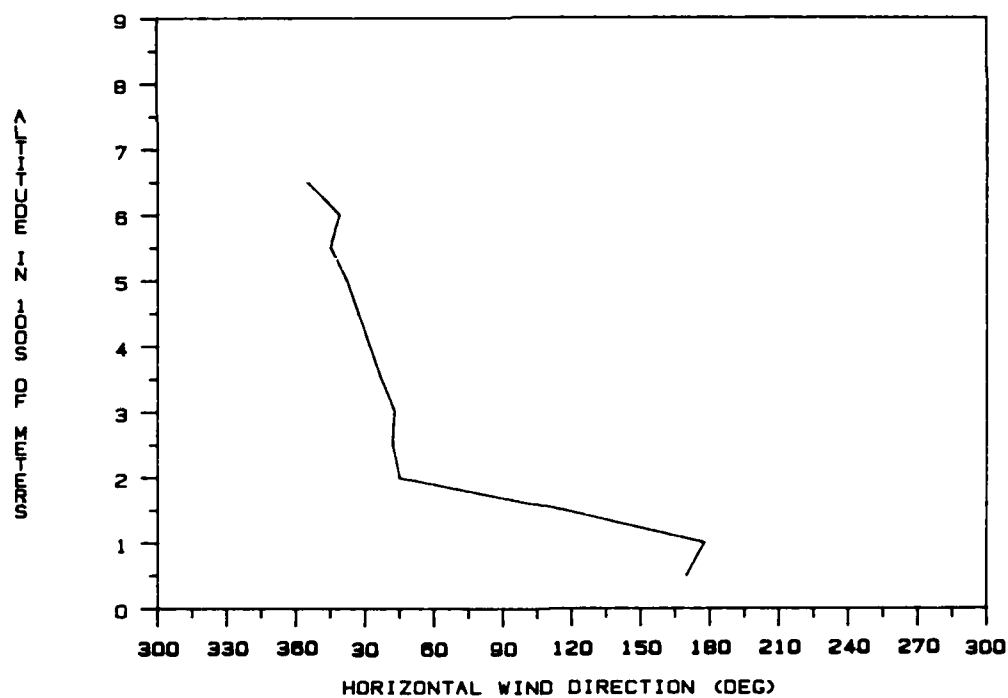
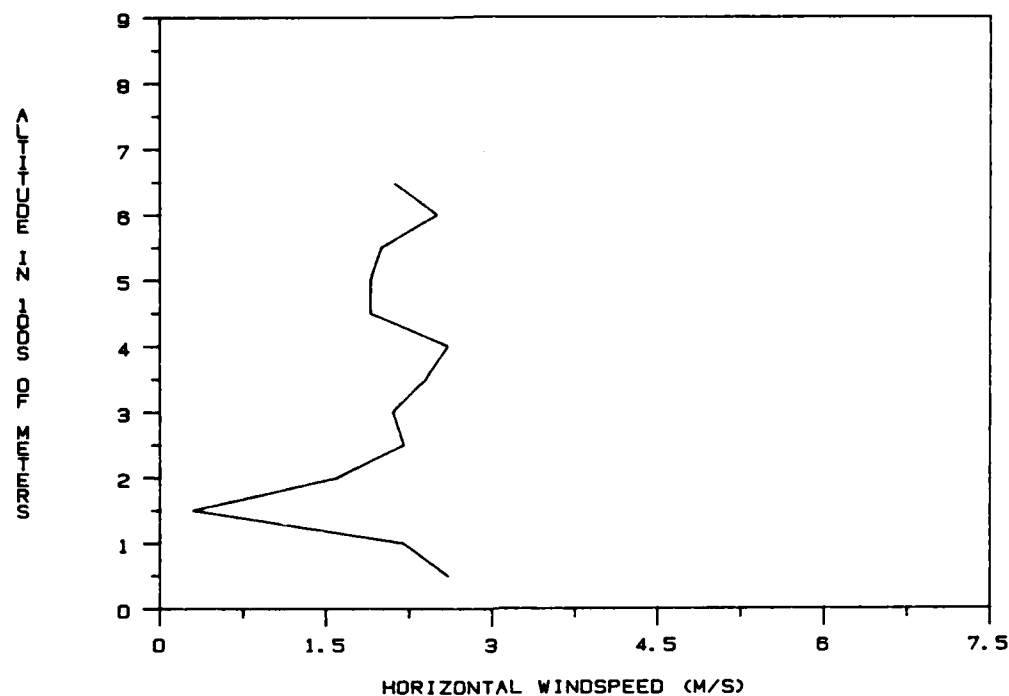
Figures 5.8a through 5.8c are the wind profiles from the 15 kilometer VAD analyses. As with the previous set of profiles, the same general trends and characteristics hold true. Noteworthy are the profiles of Figure 5.8c which depict the same low-level counter-gradient flow and strong vertical shear as that shown by Figure 5.7e. The wind speeds in the lowest hundred meters had values of between 2.5 and 3 meters per second with directions of 165 and 180 degrees at 50 and 100 meters ASL, respectively. The wind speed then dropped to nearly zero at 150 meters ASL and recovered, with slight variability, to about 2 meters per second at 200 meters ASL and above. Likewise, the wind direction backed to about 40 degrees at 200 meters ASL, followed by weak, but consistent, backing with increasing height. Again, the low-level shear depicted by this figure coincides spatially and temporally with the counter-gradient wind field anomaly, and resultant intense vertical shear, described in the preceding paragraph.



5.8a Plot of horizontal wind speed and direction versus altitude from the 15 kilometer radius VAD analysis taken by the CP-3 radar at 2034 GMT on 8 March 1986.



5.8b Plot of horizontal wind speed and direction versus altitude from the 15 kilometer radius VAD analysis taken by the CP-3 radar at 2103 GMT on 8 March 1986.



5.8c Plot of horizontal wind speed and direction versus altitude from the 15 kilometer radius VAD analysis taken by the CP-3 radar at 2131 GMT on 8 March 1986.

6. CONCLUSIONS

The single Doppler analysis technique, Velocity Azimuth Display (VAD), was successfully applied to selected radar data, acquired on 8 March 1988 along the Outer Banks of North Carolina, to attain mean value estimates of the horizontal wind, vertical velocity, horizontal divergence and deformation, at various altitudes in the mixed layer, averaged over 5, 10, and 15 kilometer analysis radii.

The calculated values for a single kinematic property, of fixed analysis radius, were plotted with respect to time and height ASL. The trend of increasing stability, as observed in the lapse rates calculated from Cape Hatteras rawinsonde data, was clearly depicted in the time-height plots. However, the vertical velocity and horizontal divergence plots deviated significantly from the smooth, consistent transition which might be expected, given the calculated lapse rates. The abrupt temporal change from strong low-level convergence and upward vertical motion, associated with the instability characteristic of the early part of the study period, to divergence and subsidence, then briefly back to its former state before final transition to fully stable conditions (as supported by the calculated lapse rates), was probably the result of meso- γ effects. Specifically, the distribution about the analysis area of migratory vertical cellular structures was the likely cause of the perturbation.

The VSLICE and wind plots well depicted the presence of a counter-gradient flow in the lowest 200 to 300 meters ASL. When combined with PAM-derived wind analyses, evidence of a nearshore meso- β

horizontal circulation pattern, with scale lengths on the order of tens of kilometers, was observed. The precise cause of this phenomenon is not clear, but certainly the weakening of the horizontal pressure gradient with time allowed for its development.

The time-series of PPI displays provide considerable insight into the meso- β wind field in the vicinity of the Outer Banks. Two significant revelations were readily evident. The differential advection of chaff, arising from differences in upwind surface roughness, indicated a definite oceanward increase in mixed layer windspeed. Also notable was the pronounced elongation of the chaff field in both the shoreward and oceanward directions. The anticyclonic shear arising from the underlying surface roughness discontinuity was undoubtedly of prime importance in generating the divergence responsible for the shoreward elongation of the chaff area. The oceanward divergence arose from the differential heating of air passing over the strong SST discontinuity between the coastal shelfwaters and the substantially warmer waters beyond the Mid-shelf Front and the nearby Gulf Stream.

The results obtained by this research certainly illustrate the utility of a single Doppler radar to collect data which provides considerable insight into boundary layer kinematics. The analysis of this particular dataset was a fine opportunity to study the MABL during rapidly changing and highly variable stability and turbulence conditions. Furthermore, the results surely give credence to the existence of meso- β scale anomalies in the "transitioning" coastal MABL which warrant further study.

7. LIST OF REFERENCES

- Atlas, D., B. Walter, S. H. Chou and P. J. Sheu, 1986: The Structure of the Unstable Marine Boundary Layer Viewed by Lidar and Aircraft Observations. Journal of the Atmospheric Sciences, 43, no. 13, 1301-1318.
- Atkinson, B. W., 1981: Meso-scale Atmospheric Circulations. Academic Press, 495 pp.
- Battan, L. J. 1981: Radar Observation of the Atmosphere. The University of Chicago Press, 324 pp.
- Battan, L. J. and J. B. Theiss, 1971: Wind Gradients and Variance of Doppler Spectra. Science Report No. 26, Institute of Atmospheric Physics, University of Arizona, Tucson, 12 pp.
- Bosart, L. F., 1981: The Presidents' Day Snowstorm of 18-19 February 1979: A Subsynoptic-Scale Event. Monthly Weather Review, 109, 1542-1566.
- Browning, K. A. and R. Wexler, 1968: The Determination of Kinematic Properties of a Wind Field Using Doppler Radar. Journal of Applied Meteorology, 7, 105-113.
- Caughy, S. J. and S. G. Palmer, 1979: Some of the Aspects of Turbulence Structure through the Depth of the Convective Boundary Layer. Quarterly Journal of the Royal Meteorological Society, 105, 811-827.
- Corbett, J., 1987: personal communication. NCAR FOF, Boulder, Colorado.
- Dennenberg, J. M., 1971: The Estimation of Spectral Moments. Technical Report No. 23, Laboratory for Atmospheric Probing, University of Chicago and Illinois Institute of Technology.
- Dirks, R. A., Kuettner, J. P., and J. A. Moore, 1988: Genesis of Atlantic Lows Experiment (GALE): An Overview. Bulletin of the American Meteorological Society, 69, no. 2, 148-160.
- Donaldson, R. J., G. M. Armstrong, K. J. Banis and R. M. Dyer, 1972: Measurement of Wind Gradients in Convective Storms by Doppler Radar. Proceedings from the 15th Radar Meteorology Conference, American Meteorological Society, 153-156.
- Doviak, R. J. and C. T. Jobson, 1979: Dual Doppler Radar Observations of Clear Air Wind Perturbations in the Planetary Boundary Layer. Journal of Geophysical Research, 84, no. C2, 697-702.

LIST OF REFERENCES (continued)

- Doviak, R. J., P. S. Ray, R. G. Strauch and L. J. Miller, 1976: Error Estimation in Wind Fields Derived from Dual Doppler Radar Measurement. Journal of Applied Meteorology, 15, no. 8, 868-878.
- Doviak, R. J. and D. S. Zrnic, 1984: Doppler Radar and Weather Observations. Academic Press, 458 pp.
- Elliot, W. P., 1958: The Growth of the Atmospheric Internal Boundary Layer. Transactions, American Geophysical Union, 39, no. 6, 1048-1054.
- Frisch, S., R. B. Chadwick, W. R. Moninger and J. M. Young, 1976: Observations of Boundary-Layer Convection Cells Measured by Dual-Doppler Radar and Echosonde, and by Microbarograph Array. Boundary Layer Meteorology, 10, 55-68.
- Gal-Chen, T., 1982: Error Analysis in Fixed and Moving Frame of Reference. Journal of the Atmospheric Sciences, 39, 2280-2300.
- Herzogh, P. H., 1986: personal communication. NCAR FOF, Boulder, Colorado.
- Herzogh, P. H., 1986: NCAR CP-3 and CP-4 Radar Data Quality in GALE: Impacts on Analysis. Technical note from the National Center for Atmospheric Research, Field Observation Facility, October 24, 1986, Boulder, Colorado, 6 pp.
- Herzogh, P. H., 1987: personal communication. NCAR FOF, Boulder, Colorado.
- Kelly, R. D., 1981: Single Doppler Radar Evidence of Horizontal Roll Convection in a Lake-Effect Snowstorm. Proceedings from the 20th Radar Meteorology Conference, American Meteorological Society, 533-535.
- Kropfli, R. A., 1983: A Review of Microwave Radar Observations in the Dry Convective Planetary Boundary Layer. Boundary-Layer Meteorology, 26, 51-67.
- Kropfli, R. A. and J. M. Wilczak, 1986: Characteristics of Terrain-Forced Eddies in the Marine Planetary Boundary Layer, From Doppler Radar Observations and a Mesoscale Numerical Model. Proceedings from the 23rd Radar Meteorology Conference, American Meteorological Society, JP186-JP189.
- LeMone, M. A., 1973: The Structure and Dynamics of Horizontal Roll Vortices in the Planetary Boundary Layer. Journal of the Atmospheric Sciences, 30, 1077-1091.

LIST OF REFERENCES (continued)

- LeMone, M. A., 1980: The Marine Boundary Layer. Workshop on the Planetary Boundary Layer, American Meteorological Society, 182-226.
- Lhermitte, R. M., 1970: Dual-Doppler Radar Observation of Convective Storm Circulation. Proceedings from the 14th Radar Meteorology Conference, American Meteorological Society, 139-144.
- Lilly, D. K., 1983: Doppler Radar as a Primary Observing Tool for the PBL. A paper presented at the AMS Specialty Conference on Air Quality Modeling of the Non-Homogeneous, Nonstationary Urban Boundary Layer, October 31-November 4, 1983, Baltimore, Maryland, 11 pp.
- Marshall, R. E., 1987: personal communication. North Carolina State University, Department of Electrical Engineering, Raleigh, North Carolina.
- Miller, L. J. and R. G. Strauch, 1974: A Dual-Doppler Radar Method for the Determination of Wind Velocities within Precipitating Weather Systems. Remote Sensing of the Environment, 3, 219-235.
- Moninger, W. R. and R. A. Kropfli, 1982: Radar Observations of a Plume From an Elevated Continuous Point Source. Journal of the Atmospheric Sciences, 21, 1685-1697.
- O'Bannon, T., 1978: A Study of Dual-Doppler Synthesized Clear Air Wind Fields. Proceedings from the 18th Radar Meteorology Conference, American Meteorological Society, 65-69.
- Rabin, R. and D. Zrnic, 1980: Subsynoptic-Scale Vertical Wind Revealed by Dual Doppler-Radar and VAD Analysis. Journal of the Atmospheric Sciences, 37, 644-654.
- Raman, S., and A. J. Riordan, 1988: The Genesis of Atlantic Lows Experiment: The Marine-Boundary-Layer Subprogram of GALE. Bulletin of the American Meteorological Society, 69, no. 2, 161-172.
- Readings, C. J., E. Golton and K. A. Browning, 1973: Fine-Scale Structure and Mixing within an Inversion. Boundary Layer Meteorology, 4, 275-287.
- Sampson, R. J., 1978: Surface II Graphics System [Revision One]. Kansas Geological Survey, Lawrence, Kansas, 240 pp.
- Raman, S., A. J. Riordan, T. Holt, M. Stunder and J. Hinman, 1986: Observations of the Marine Boundary Layer Thermal Structure Over the Gulf Stream During a Cold Air Outbreak. Journal of Climate and Applied Meteorology, 25, no. 1, 14-21.

LIST OF REFERENCES (continued)

- Stage, S. A., 1983: Boundary Layer Evolution in the Region Between Shore and Cloud Edge during Cold-Air Outbreaks. Journal of the Atmospheric Sciences, 40, 1453-1471.
- Stanley, W. D., G. R. Dougherty and R. Dougherty, 1984: Digital Signal Processing. Reston Publishing Co., 2nd edition, 514 pp.
- United States Department of Commerce, 1986: Daily Weather Maps, Weekly Series March 3-9, 1986.
- Waldteufel, P. and H. Corbin, 1979: On the Analysis of Single Doppler Radar Data. Journal of Applied Meteorology, 18, 532-542.
- Wilson, D. A., 1970: Doppler Radar Studies of Boundary Layer Wind Profiles and Turbulence in Snow Conditions. Proceedings from the 14th Radar Meteorology Conference, American Meteorological Society, 191-196.
- Yanagisawa, Z. and M. Ishihara, 1983: Doppler Radar Observation of Sea Breeze Fronts. Proceedings from the 21st Radar Meteorology Conference, American Meteorological Society, 668-669.